Energie & Umwelt
Energy & Environment

Gas-to-Particle Partitioning

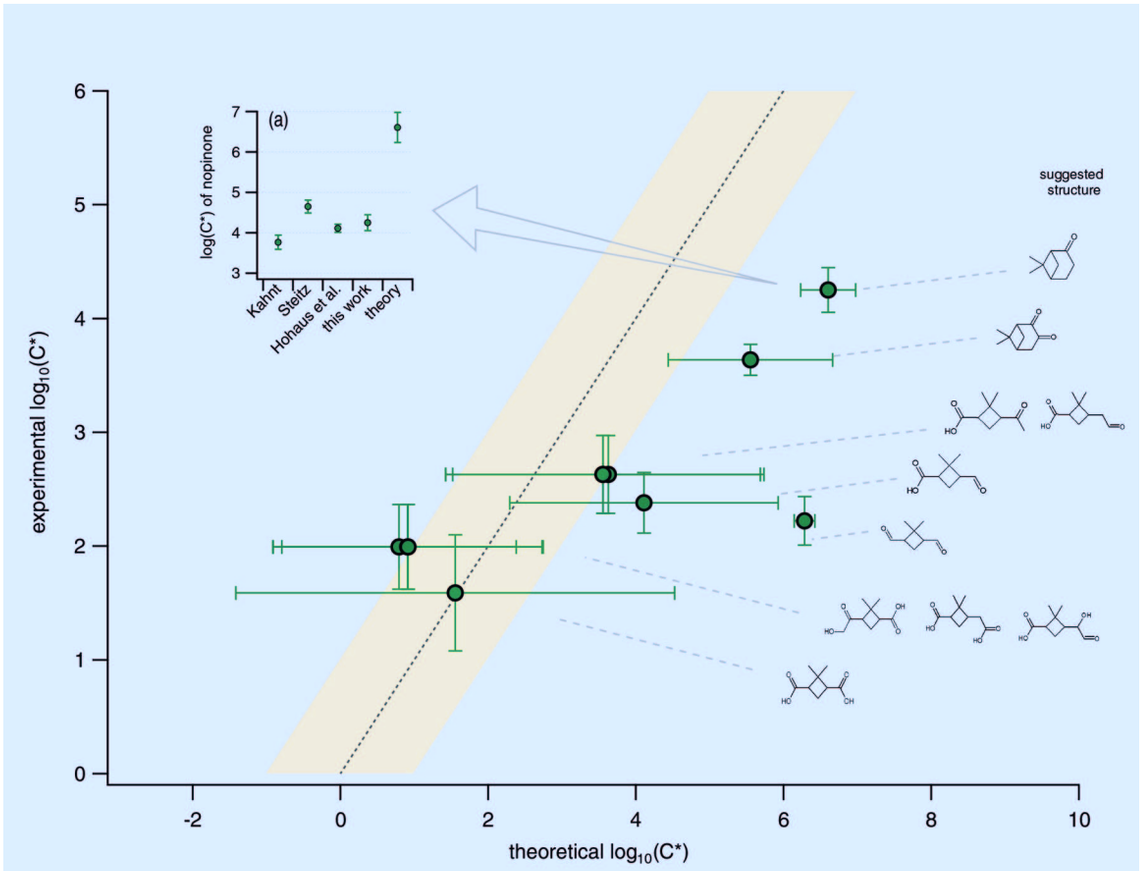

417

Georgios Gkatzelis

Gas-to-Particle Partitioning of Major Oxidation Products from Monoterpenes and Real Plant Emissions

Georgios Gkatzelis

Energie & Umwelt / Energy & Environment
Band / Volume 417
ISBN 978-3-95806-314-3

Energie & Umwelt / Energy & Environment
Band / Volume 417
ISBN 978-3-95806-314-3

Mitglied der Helmholtz-Gemeinschaft

JÜLICH Forschungszentrum

JÜLICH Forschungszentrum

Mitglied der Helmholtz-Gemeinschaft

JÜLICH Forschungszentrum

Schriften des Forschungszentrums Jülich
Reihe Energie & Umwelt / Energy & Environment Band / Volume 417

Forschungszentrum Jülich GmbH
Institut für Energie- und Klimaforschung
Troposphäre (IEK-8)

Gas-to-Particle Partitioning of Major Oxidation Products from Monoterpenes and Real Plant Emissions

Georgios Gkatzelis

Schriften des Forschungszentrums Jülich
Reihe Energie & Umwelt / Energy & Environment Band / Volume 417

ISSN 1866-1793 ISBN 978-3-95806-314-3

Bibliografische Information der Deutschen Nationalbibliothek.
Die Deutsche Nationalbibliothek verzeichnet diese Publikation in der Deutschen Nationalbibliografie; detaillierte Bibliografische Daten sind im Internet über http://dnb.d-nb.de abrufbar.

Herausgeber und Vertrieb:	Forschungszentrum Jülich GmbH Zentralbibliothek, Verlag 52425 Jülich Tel.: +49 2461 61-5368 Fax: +49 2461 61-6103 zb-publikation@fz-juelich.de www.fz-juelich.de/zb
Umschlaggestaltung:	Grafische Medien, Forschungszentrum Jülich GmbH
Druck:	Grafische Medien, Forschungszentrum Jülich GmbH
Copyright:	Forschungszentrum Jülich 2018

Schriften des Forschungszentrums Jülich
Reihe Energie & Umwelt / Energy & Environment, Band / Volume 417

D 38 (Diss., Köln, Univ., 2017)

ISSN 1866-1793
ISBN 978-3-95806-314-3

Vollständig frei verfügbar über das Publikationsportal des Forschungszentrums Jülich (JuSER) unter www.fz-juelich.de/zb/openaccess.

I would like to dedicate this thesis to my family, Eirini and in memory of Maria

Acknowledgements

This work would not have been possible without the supervision and guidance of Prof. Astrid Kiendler-Scharr and the everyday feedback, advice, and support from Dr.Thorsten Hohaus and Dr. Ralf Tillmann. The scientific outcome of this work is a result of their patience and endless support, motivating me to learn not only through my achievements but more importantly through my mistakes without ever discouraging me. Furthermore, I am really thankful for the numerous opportunities (conferences, campaigns, workshops) given to me throughout these three years. All the above has helped me build-up a more confident scientific character and I will always be very grateful for that.

The findings of this study are a result of a fruitful collaboration of the Institute of Energy and Climate Research in Jülich together with the University of Innsbruck, Austria and the Institute of Marine and Atmospheric research in Utrecht. Experiments conducted in the SAPHIR chamber were designed by Dr. Ralf Tillmann, Prof. Rupert Holzinger, Prof. Armin Wisthaler and Prof. Astrid Kiendler-Scharr. Dr.Thorsten Hohaus and Dr. Ralf Tillmann operated the chambers. Dr. Philipp Eichler and Dr. Markus Müller, Dr. Kang-Ming Xu and Prof. Rupert Holzinger, Dr. Robert Wegener and Dr. Martin Kaminski, Sebastian Schmitt, and Zhujun Yu operated and analyzed the data for the CHARON, TD, GC-MS, AMS and PTRMS respectively. Dr. Markus Müller designed and carried out the laboratory characterization experiments to further support the findings of this campaign. Dr. Patrick Schlag supported this work with software development and literature review. All these efforts were essential for the outcome of this work and are greatly valued.

I would like to especially thank Lüdke Wolfgang for our successful collaboration on the re-development of all electronic parts of the ACM. Furthermore, support provided by Dominik Raak and Kamil Kubik from the electronic workshop and Egmen Ayhan from the mechanical workshop were very much appreciated. LabVIEW software support from Mathias Bachner and further software support from Helga London and Michael Decker made the automation and data analysis of ACM possible.

Finally, I would like to thank all my colleagues for the very fruitful discussions, especially Dr. Patrick Schlag, Sebastian Schmitt, Dr. Zhao Defeng, Scarlet Stadtler, David Reimer, Avtandil Turdziladze and Sungah Kang. Support during the last three years from my family, friends and my girlfriend Eirini have been essential for carrying out this project.

Zusammenfassung

Sekundäre Organische Aerosole (SOA), welche durch die Oxidation von flüchtigen organischen Verbindungen (VOCs) in der Atmosphäre gebildet werden, spielen eine Schlüsselrolle bezüglich des Klimawandels und der Luftqualität. Tausende organische Substanzen sind an der Bildung von SOA beteiligt, weshalb die chemische Charakterisierung von organischen Aerosolen (OA) weiterhin eine große Herausforderung an die Analytik darstellt. Die Definition der Parameter, die bestimmen wie sich organische Moleküle zwischen der Gasphase und der Partikelphase verteilen, ist essentiell, da ihre atmosphärischen Lebenszeiten und damit ihr Einfluss stark davon abhängen in welcher Phase sie vorliegen. In dieser Arbeit wurde das sogenannte Aerosol Collection Module (ACM) verbessert, automatisiert und eingesetzt, um eine bessere Charakterisierung von SOA, welches aus Oxidationsprodukten von biogenen Vorläufersubstanzen gebildete wurde, zu erreichen. Eine Vergleichsstudie des ACM mit anderen Techniken zur chemischen Charakterisierung von SOA wurde durchgeführt, bei der der Fokus auf der Bestimmung der Partitionierung biogenen Oxidationsprodukten zwischen der Gasphase und Partikelphase lag. Die eingesetzten Instrumente waren der ACM, die „collection thermal desorption unit“ (TD) und der „chemical analysis of aerosol on-line“ (CHARON), welches verschiedene Aerosolsammler sind, die ein gekoppeltes Proton-Transfer-Reaktion Massenflugzeitspektrometer (PTR-ToF-MS) zur Detektion verwenden. Diese Instrumente wurden an der Atmosphärensimulationskammer SAPHIR eingesetzt, um die Bildung und die Alterung von SOA aus verschiedenen Monoterpenen (β-Pinen, Limonen) und realen Pflanzenemissionen (*Pinus sylvestris L.*) zu untersuchen. Die Charakteristiken der PTR-basierten Instrumente wurden untereinander und mit den Ergebnissen eines Aersolmassenspektrometers und eines SMPS-Spektrometers verglichen. Die Werte der Partitionierung von einzelnen Ionen zwischen der Gas- und Partikelphase, ausgedrückt durch die Massensättigungskonzentration (C*), wurde über die gleichzeitige Messung der Ionen in der Gas- und Partikelphase bestimmt.

Trotz der deutlichen Unterschiede der PTR-basierten Instrumente in den Methoden wie Aerosole gesammelt und desorbiert werden, war die Bestimmung der chemischen Zusammensetzung, d.h. die Ionen die den Hauptanteil zum Signal beigetragen haben, für die verschiedenen System vergleichbar. Diese Ionen konnten als Hauptoxidationsprodukten von den untersuchten Monoterpenen identifiziert werden. Gemittelt über alle Experimente war die Wiederfindungsrate der Aerosolmasse verglichen mit dem SMPS-Spektrometer 80 ± 10% für CHARON, 51 ± 5% für den ACM und 27 ± 3% für den TD. Der Vergleich des Sauerstoff zu Kohlenstoff Verhältnisses (O:C) vom AMS zu den PTR-basierten Instrument zeigte, dass all PTR-basierten Instrument ein niedrigeres Verhältnis gemessen haben. Das deutet auf einen Verlust von molekularem Sauerstoff hin, der entweder während der Sammlung oder der Desorption verloren geht. Die Unterschiede der Wiederfindungsrate der Aerosolmasse und des O:C Verhältnisses zwischen den drei PTR-basierten Instrumente konnte hauptsächlich

auf Unterschiede in dem Verhältnis von der elektischen Feldstärke (V cm^{-1}) zu der Dichte des Puffergases (Moleküle cm^{-3}) (E/N) in der Laufzeitionisationsröhre des PTR-MS und den Unterschieden in der Sammlung und Desorption der Aerosole zurückgeführt werden.

Eine Methode zur Identifizierung von Ionen, die von thermischer Dissoziation während der Desorbtion und der ionischen Dissoziation während der Ionisierung im PTR-MS betroffen waren, wurde entwickelt und getestet. Die Ionen, die nach Anwendung dieser Methode als nicht betroffen identifiziert wurden, wurden auf das zweidimensionale Volatilitätssystem (2D-VBS) abgebildet. Die Ergebnisse zeigen eine Abnahme von C* mit zunehmendem Oxidationsgrad. Für Substanzen die mit den PTR-basierten Instrumenten gemessen und in früheren Studien schon identifiziert wurden, wurden weitere Vergleiche mit theoretischen Berechnungen durchgeführt. Die theoretischen Berechnungen von C* basieren auf der Molekülstruktur der identifizierten Substanzen und zeigen eine gute Übereinstimmung mit den experimentell gemessen C* im Bereich von 10^{0} to $10^{2.5}$. Im Gegensatz dazu liegen im Bereich von $C^* > 10^{2.5}$ die theoretischen Berechnung von C* bis zu einem Faktor von 300 über den gemessen Werten. Diese Unterschiede im Bereich von $C^* > 10^{2.5}$ deuten auf (i) mögliche Interferenzen durch thermische und ionische Fragmentierung von Molekülen mit hohen Molekulargewichten hin, welche durch Oligomerization und Akkretion gebildet werden und dann durch Fragmentierung im messbaren m/z-Bereich des PTR-MS gemessen werden sowie (ii) kinetische bedingte Verschiebungen in der Verteilung zwischen Gas- und Partikelphase mit dem Schwerpunkt auf der Kondensation und der irreversiblen Aufnahme von Substanzen in die Partikelphase.

Abstract

Secondary organic aerosol (SOA), formed through the oxidation of volatile organic compounds (VOCs) in the atmosphere, play a key role in climate change and air quality. Due to thousands of individual compounds involved in SOA formation, the chemical characterization of organic aerosols (OA) remains a huge analytical challenge. Defining the fundamental parameters that distribute these organic molecules between the gas and particle phases is essential, as atmospheric lifetime and their impacts change drastically depending on their phase state. In this work, an instrument called aerosol collection module (ACM) was re-developed and automated to allow a better characterization of SOA originating from the oxidation of biogenic precursors. An inter-comparison of the ACM to different aerosol chemical characterization techniques was performed with a focus on the partitioning of major biogenic oxidation products between the gas- and particle-phase. In particular, the ACM, the collection thermal desorption unit (TD) and the chemical analysis of aerosol on-line (CHARON) are different aerosol sampling inlets utilizing a Proton-Transfer-Reaction Time-of-Flight Mass Spectrometer (PTR-ToF-MS). These techniques were deployed at the atmosphere simulation chamber SAPHIR to study SOA formation and aging from different monoterpenes (β-pinene, limonene) and real plant emissions (*Pinus sylvestris L.*). The capabilities of the PTR-based techniques were compared among each other and to results from an Aerodyne Aerosol Mass Spectrometer (AMS) and a Scanning Mobility Particle Sizer (SMPS). Gas-to-particle partitioning values were determined based on the saturation mass concentration (C*) of individual ions by performing simultaneous measurement of their signal in the gas- and particle-phase.

Despite significant differences in the aerosol collection and desorption methods of the PTR based techniques, the determined chemical composition was comparable, i.e. the same major contributing ions were found by all instruments for the different chemical systems studied. These ions could be attributed to known products expected from the oxidation of the examined monoterpenes. Averaged over all experiments, the total aerosol mass recovery compared to an SMPS was 80 ± 10%, 51 ± 5% and 27 ± 3% for CHARON, ACM and TD, respectively. Comparison to the oxygen to carbon ratios (O:C) obtained by AMS showed that all PTR based techniques observed lower O:C ratios indicating a loss of molecular oxygen either during aerosol sampling or detection. Differences in total mass recovery and O:C between the three instruments was found to result predominately from differences in the electric field strength (V cm^{-1}) to buffer gas density (molecules cm^{-3}) (E/N) ratio in the drift-tube reaction ionization chambers of the PTR-ToF-MS instruments and from dissimilarities in the collection/desorption of aerosols.

A method to identify and exclude ions affected by thermal dissociation during desorption and ionic dissociation in the ionization chamber of the PTRMS was developed and tested. Determined species were mapped onto the two dimensional volatility basis set (2D-VBS) and results showed a decrease of the C* with increasing oxidation state. For compounds measured

from the PTR techniques that were also found in previous publications further comparison was performed. Theoretical calculations based on the molecular structure of the compounds showed relatively good agreement, within the uncertainties of the calculations, with the experimental C* ranging from 10^0 to $10^{2.5}$, while for C* > $10^{2.5}$ theory showed higher C* up to a factor of 300. These major differences point towards (i) possible interferences by thermal and ionic fragmentation of higher molecular weight compounds, produced by accretion and oligomerization reactions that show up at *m/z*'s detected by the instruments, as well as (ii) kinetic influences in the distribution between gas- and particle-phase with condensation to the particle-phase and irreversible uptake.

Contents

Chapter 1 Introduction

In this chapter the importance of atmospheric aerosol (section 1.1) with a focus on organic aerosol and their formation, volatility and equilibrium thermodynamics (section 1.2) is performed. An overview of the instrumentation developed to measure the chemical composition of organic aerosol is presented (section 1.3). Methods to determine the saturation mass concentration from experimental approaches (section 1.4.1) to empirical and explicit methods are discussed (section 1.4.2). Finally, the objective of this work is summarized (section 1.5).

1.1 Atmospheric aerosols

Atmospheric aerosols are defined as a suspension of fine solid or liquid particles suspended in a gaseous medium. These particles range in size from 100 µm down to a few nanometers. Aerosols consist of organic compounds, inorganic ions, oxides of most metals, elemental carbon and water. Depending on their number, size and chemical composition, atmospheric aerosols have varying effects. Fine particles are air pollutants with a diameter of 2.5 micrometers or less defined as PM 2.5 (Particulate Matter, 2.5 micrometers or less).. PM 2.5 can affect human health by penetrating into the respiratory tract and reaching deep into the lungs e.g. (Lelieveld et al., 2015, Pöschl and Shiraiwa, 2015, Künzli et al., 2004). Furthermore, atmospheric aerosols can affect the Earth's radiative budget and global climate either directly, by scattering and absorption of solar radiation or indirectly, by their potential to act as cloud condensation nuclei, influencing cloud formation and properties (Seinfeld and Pandis, 2006). Overall, aerosols are estimated to have a cooling effect on climate (Intergovernmental Panel on Climate Change, IPCC 2013) as shown in Figure 1. Important to note is that the highest uncertainties on the radiative estimates is introduced due to the uncertain impacts of aerosols and their precursors on the climate. These uncertainties are to a large extent responsible for the uncertainties observed in global climate modelling (Kiehl, 2007) and further promote research in understanding aerosol formation and aging.

1.2 Atmospheric organic aerosols: formation, volatility and equilibrium thermodynamics

Atmospheric organic aerosols (OA) represent a major contribution to the submicrometer particulate matter (PM_1) thus playing a key role in climate change and air quality (Kanakidou et al., 2005). OA are either directly emitted through e.g. combustion processes (primary OA,

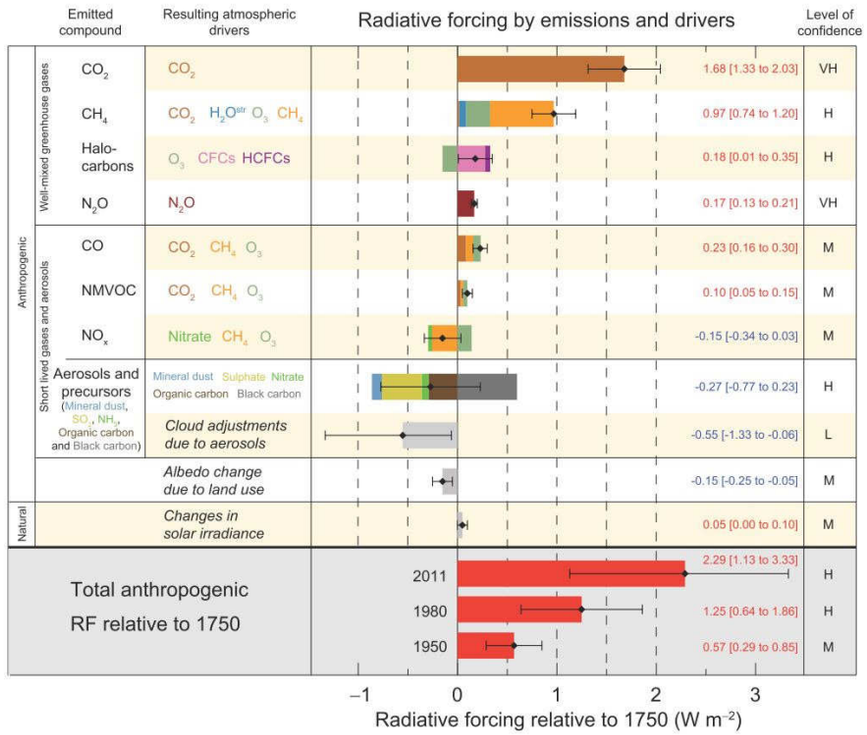

Figure 1: The IPCC report of 2013 (Stocker et al., 2013) that shows the radiative forcing estimates in 2011 relative to 1750and aggregated uncertainties for the main drivers of climate change. Values correspond to the average radiative forcing portioned according to the processes that result in a combination of drivers or the emitted compounds. The best estimates of the net radiative forcing are shown as black diamonds with corresponding uncertainty intervals; the numerical values are provided on the right of the figure, together with the confidence level in the net forcing (VH – very high, H – high, M – medium, L – low, VL – very low).

POA) or formed through the oxidation of volatile organic compounds (VOCs), called secondary OA (SOA) (Seinfeld and Pandis, 2006). SOA constitute a major fraction of OA (Jimenez et al., 2009) with biogenic VOC oxidation products affecting their global contribution (Guenther et al., 2012). Due to thousands of individual compounds involved in SOA, the chemical characterization of OA still presents a huge analytical challenge (Goldstein and Galbally, 2007). Theoretical model approaches that treat organic aerosol tend to underestimate their abundance by a factor of 10 to 100 in the free troposphere (Heald and Spracklen, 2015). These large deviations suggest higher SOA yields than expected from theoretical calculations. In order to better define these discrepancies further investigation of the chemical processes, formation pathways and the equilibrium thermodynamics of these complex systems is required.

SOA is formed through the oxidation of anthropogenic and biogenic VOCs by ozone, hydroxyl-radicals or nitrate radicals. The oxidation products formed have a lower volatility than the precursor compound due to the addition of an oxygen and/or a nitrogen atom to the organic molecules (Odum et al., 1996). Condensation will occur when the vapor pressure of a compound in the gas-phase exceeds its saturation vapor pressure. In complex mixtures and by assuming thermodynamic partitioning equilibrium and neglecting curvature effects, the transition from the gas- to the particle-phase, is expressed by the modified Raoult's law as:

$$p_i^{eq} = \zeta_{x,i}\, x_i\, p_i^o \quad (1)$$

where p_i^{eq} is the equilibrium vapor pressure, $\zeta_{x,i}$ is the mole-fraction-based activity coefficient, x_i is the mole fraction of i in the mixture and p_i^o is the pure component saturation vapor pressure. The molecular interactions of i in the condensed phase determine the saturation vapor pressure that is a strong function of temperature and the enthalpies of vaporization and sublimation based on the Clausius-Clapeyron equation:

$$\frac{dp_i^o}{dT} = \frac{\Delta H_{trs,i}}{T\,\Delta v_{m,i}} \quad (2)$$

where T is the temperature and $\Delta H_{trs,i}$ and $\Delta v_{m,i}$ are the changes of molar enthalpy and molar volume upon the phase transition (vaporization or sublimation), respectively.

OA are expected to show volatilities in the range from intermediate volatility OA (10^{-4} atm) to extremely low volatility OA (10^{-12} atm) (Donahue et al., 2013) thus spanning a wide range of saturation vapor pressures. The determination of the saturation vapor pressure thus plays a central role in better understanding their distribution between the gas and particle phases. As atmospheric lifetime and impacts change drastically between phases, understanding how these molecules distribute between the gas- and particle-phase is essential. Attempts to

experimentally and theoretically determine the saturation vapor pressure of simple and complex systems have been performed in the last decade (discussed in detail in section 1.4). In the following sections a summary of the state-of-the-art instrumentation to better understand both the chemical composition and volatility of OA is provided.

1.3 Instrumentation to measure the chemical composition of organic aerosol

Various techniques have been established in order to better quantify and chemically characterize SOA (Hallquist et al., 2009). These techniques optimize and compromise for time, size or chemical resolution combined with the percentage of OA mass they can detect. Off-line techniques, based on filter measurement, provide detailed information on functional groups or individual chemical species while having low time resolution (hours to days) and limited size information. These techniques can be prone to risks of gas-phase interferences since filters also absorb gas-phase compounds. Furthermore, loss processes from the re-evaporation of particles back to the gas-phase due to long collection times, temperature changes during collection or losses during filter transfer and storage could lower the OA mass recovered. On-line techniques, like e.g. the Aerodyne aerosol mass spectrometer (AMS) (Canagaratna et al., 2007), provide high time resolution and size resolved data while less specific chemical composition information or molecular identification of the OA compounds is acquired.

In recent years attempts to develop new techniques that combine both chemical identification but also improved time resolution have been established (Lopez-Hilfiker et al., 2014, Williams et al., 2006, Hohaus et al., 2010, Holzinger et al., 2010b, Eichler et al., 2015). These techniques use different pre-concentration methods in order to detect the particulate-phase compounds. Filter based techniques like the Filter Inlet for Gases and AEROsols (FIGAERO) (Lopez-Hilfiker et al., 2014) provide highly effective collection of particles on filters, under high flow rates (30 standard Liters per minute, sLpm), thus low collection times. Thermal desorption of the sampled particles on the filter is performed. Contrary to conventional filter techniques, FIGAERO is not influenced by storage and handling losses comparable to the off-line filter measurements. Still this technique has the disadvantage of sampling artefacts from gas-phase compounds that may condense on the large surface area of the filter and contribute to the overall signal.

Techniques that efficiently remove the gas-phase signal during collection of the particle-phase have been further developed. The thermal desorption aerosol gas chromatograph (TAG) (Kreisberg et al., 2009, Williams et al., 2006) or the collection thermal desorption unit (TD) (Holzinger et al., 2010b), utilize the concept of particle collection on an impaction surface by means of humidification and inertial impaction, followed by desorption. TAG and TD provide hourly time resolution measurements, and when combined with a gas-phase denuder reduce sampling of additional gas-phase constituents on their collection thermal desorption (CTD) cell. Due to the particle humidification step these techniques may bias collection efficiency towards water soluble compounds. The aerosol collection module (ACM) (Hohaus et al., 2010) collects aerosols by passing them through an aerodynamic lens for particle collimation (Liu et al., 1995a, Liu et al., 1995b), further through a vacuum system (comparable in design to the AMS), and finally impacting the particle phase on a cooled sampling surface (more details provided in Chapter 2). The aerodynamic lenses and vacuum system of the ACM allow complete removal of gas-phase organic compounds thus making its design applicable for the investigation of compound specific thermodynamic properties e.g. partitioning coefficient and volatility (Hohaus et al., 2015) with the disadvantage of a relatively low time resolution (3-4 h) compared to the previous mentioned techniques. The chemical analysis of aerosol online (CHARON) (Eichler et al., 2015) is a technique that provides on-line real time measurements by passing the particles through a denuder to strip off the gas-phase. Particles are sampled through an aerodynamic lens combined with an inertial sampler for the particle-enriched flow, and a thermodesorption unit for particle volatilization prior to chemical analysis. The enrichment factor of this system is known by performing calibrations, thus reducing the quantification uncertainty. All the above pre-concentration systems detect the compounds originating from the particulate-phase that underwent evaporation to the gas-phase by desorption, thus introducing possible thermal break down of analytes during desorption.

A variety of detection instruments have been coupled to these inlet techniques, providing different functionality and chemical composition information. The proton-transfer-reaction time-of-flight mass spectrometer (PTR-ToF-MS) (Jordan et al., 2009) is a soft ionization technique with low detection limits and high time resolution (ms), that can cover a wide volatility range, from VOCs to low-volatility organic compounds (LVOCs), depending on the inlet used (Eichler et al., 2017). Techniques utilizing a PTR-ToF-MS (details in section 3.3) are capable of measuring a large fraction of the OA mass, ranging from 20 to 100% (Mensah et al., 2012, Eichler et al., 2015), and provide additional information on the elemental

composition of the organic compounds; however, the compound's molecular identity attribution is challenging. On the contrary, gas chromatography mass spectrometry is considered ideal for detailed compound specific structural analysis. Techniques like the TAG have been applied utilizing a gas chromatograph, to provide non-polar and low-polarity tracers identification while the modified semi-volatile TAG (SV-TAG) has broadened this range to highly polar oxygenates, mostly seen in the atmosphere, by using online derivatization (Zhao et al., 2013b, Isaacman et al., 2014). The volatility and polarity separator (VAPS) is a similar technique that provides volatility- and polarity-resolved OA information by using a modified 2-dimensional gas chromatography (2D-GC) approach combined with high resolution time -of -flight mass spectrometry (Martinez et al., 2016). Although these techniques provide chemical speciation and lower time resolution, they can only do so for a small fraction of the OA mass (10 - 40%).

1.4 Methods to determine the saturation mass concentration C*

Experimental and theoretical attempts to measure the saturation vapor pressure of OA compounds have been further established. Recent studies use the saturation mass concentration C* in units of μg m^{-3} (Donahue et al., 2012, Donahue et al., 2011) to express the saturation vapor pressure and thus the volatility of different species. This term is also used throughout this work. Considering equilibrium absorptive partitioning the (sub-cooled liquid) saturation vapor pressure ($p_{i,L}$) of a species is related to its C* based on Cappa and Jimenez (2010) as following:

$$C_i^*(\mathrm{T}) = \frac{\mathrm{MW_{OA}} \times 10^6 \times \mathrm{p_{i,L}} \times \zeta_\mathrm{i}}{\mathrm{R} \times \mathrm{T}} \qquad (3)$$

where MW_{OA} is the mean molecular weight of the condensed organic phase (180 g mol^{-1}) (Prisle et al., 2010), $p_{i,L}$ is the sub-cooled liquid saturation vapor pressure of species i, ζ_i is the activity coefficient of species i in the OA phase, T is the chamber temperature (K) and R is the ideal gas constant (8.314 J mol^{-1} K^{-1}).

There are three major ways to determine experimentally the saturation mass concentration of individual compounds. A commonly used method is by performing calibrations of the instrument with standards of known saturation vapor pressure (Lopez-Hilfiker et al., 2015, Lopez-Hilfiker et al., 2014). The limitations and challenges of this approach lie on the narrow volatility range that can be covered from a limited number of commercially available compounds. Another approach is by developing theoretical thermodynamic models to define the experimental setup and derive the C* based on the model calculations (Pankow and

Asher, 2008, Riipinen et al., 2010), thus increasing the uncertainty of these estimations. Finally, when applicable, C* can be derived by simultaneous measurement of the gas- (G_i) and particle-phase concentration (P_i) of a compound in µg m^{-3}, combined with the overall organic mass concentration (OA) in µg m^{-3} (Hohaus et al., 2015, Stark et al., 2017, Isaacman-VanWertz et al., 2016). The equation used to derive C* is by applying the partitioning theory (Pankow, 1994) based on Donahue et al. (2006) as

$$C^* = OA \times \frac{G_i}{P_i}, \quad (4)$$

Since SOA consist predominantly of oxidized multifunctional compounds (McFiggans et al., 2010) organic compounds are expected to show low saturation vapor pressures thus increasing the detection challenges due to the low gas-phase concentrations that need to be probed (Bilde et al., 2015).

Different instrumentation has been developed using one or more of the above mentioned methods to derive the saturation mass concentration. An overview of these techniques is provided in the following.

1.4.1 Experimental approaches

Instrument development to determine the saturation vapor pressure and thus the saturation mass concentration (C*) and volatility of single components and complex organic aerosol systems has been advanced in the past decades both for laboratory and field studies. Dicarboxylic acids represent a class of low-volatility compounds commonly found in atmospheric aerosol that are commercially available. These molecules have been extensively studied by various techniques (Bilde et al., 2015). Namely, the Knudsen effusion mass spectrometry (KEMS) (Booth et al., 2009) is a method were macroscopic crystalline samples effuse in a Knudsen cell and the change of the concentration in the gas phase is measured using a mass spectrometer and translated to saturation vapor pressure values based on calibrated standards. Single particle methods using optical tweezers (Mitchem and Reid, 2008) and the electrodynamic balance (EDB) (Pope et al., 2010) infer saturation vapor pressure values from the evaporation or condensational growth of a single particle at a controlled environment. Thermal desorption mass spectrometry (TDMS) has extended the studies from laboratory to ambient complex poly-disperse systems. Thermodenuders (TDs) have been extensively used to quantify the volatility of the bulk OA (Faulhaber et al., 2009, Huffman et al., 2008, An et al., 2007, Louvaris et al., 2017, Gkatzelis et al., 2016, Isaacman-VanWertz et al., 2017) by measuring the OA mass fraction remaining after passing the OA

through the heated TD. By combining this information with the support of mass transfer models, the kinetic and thermodynamic effects and thus the saturation mass concentration can be derived (Riipinen et al., 2010, Karnezi et al., 2014). However, the detector used in most of these studies is an AMS (Canagaratna et al., 2007) that operates at high vaporizer temperatures (600 °C) and ionizes the analytes by electron impact (70 eV) thus introducing excessive thermal and ionic decomposition.

As discussed in the previous section different methods have been recently developed that compromise between molecular level information for a small fraction of the OA mass (Williams et al., 2014, Zhang et al., 2014, Kreisberg et al., 2009, Williams et al., 2006, Hohaus et al., 2010) or chemical formula identification using soft ionization MS to achieve a more comprehensive OA characterization (Gkatzelis et al., 2017, Stark et al., 2017, Lopez-Hilfiker et al., 2014, Isaacman-VanWertz et al., 2017). Volatility measurements are performed either by calibrating with standards of known saturation vapor pressure (Lopez-Hilfiker et al., 2015, Lopez-Hilfiker et al., 2014) or by simultaneous measurement of the gas- and particle-phase mass concentration of the molecule when applicable (Hohaus et al., 2015, Stark et al., 2017, Isaacman-VanWertz et al., 2016).

In order to identify the C* of OA on a molecular level, thermal desorption techniques have been coupled to Gas-Chromatography (GC) methods. The 2D-TAG (Isaacman et al., 2011) and the VAPS (Martinez et al., 2016) provide volatility- resolved OA based on the two-dimensional chromatographic retention times relative to those of known standards, thus establishing a retention time correlation (RTC) to the vapor pressure. Simultaneous measurements of the gas- and particle-phase mass of organic molecules has also been recently developed using the SV-TAG that utilizes two CTD cells in parallel (Isaacman-VanWertz et al., 2016). As previously discussed, although the above GC methods provide chemical speciation and gas-to-particle partitioning in a molecular level, they can only do so for a small fraction of the OA mass (10 - 40%).

The newly developed thermal desorption inlets have allowed near-simultaneous chemical characterization of gas- and particle-phase ambient compounds (Eichler et al., 2015, Holzinger et al., 2010b, Stark et al., 2017, Lopez-Hilfiker et al., 2014, Yatavelli et al., 2014, Gkatzelis et al., 2017). When coupled to chemical ionization high resolution, time-of-flight mass spectrometers (ToF-CIMS) these inlets can provide information on a very broad volatility range (Eichler et al., 2017). By simultaneous measurement of the gas- and particle-phase mass concentration when applicable, direct volatility calculations of individual species can be performed. Indirect ways of estimating the vapor pressure for this type of systems

have been also established based on the desorption temperature of calibrated known species or mixtures (Stark et al., 2017, Lopez-Hilfiker et al., 2016).

1.4.2 Empirical and explicit methods to calculate C*: Trying to bridge the gap between theory and experiments

There are two major ways to treat partitioning for practical applications to atmospheric aerosol that have been established in the last years. One is through a thermodynamic model containing an ensemble of specific molecules (Aumont et al., 2005) while the other is based on empirical calculations (Donahue et al., 2014). When using explicit methods, model systems are treated as fully as possible thus individual vapor pressures and activity coefficients are calculated based on several thermodynamic schemes (Zuend et al., 2011, Clegg et al., 2001, Fredenslund et al., 1975). These calculations are strongly affected by the wide range of vapor pressure estimates from the different theoretical approaches (Donahue et al., 2014, Camredon et al., 2010). The required thermodynamic properties, such as the boiling temperature or the enthalpy of vaporization are predicted from the molecular structure of the investigated compounds (Joback and Reid, 1987, Mackay et al., 1982, Stein and Brown, 1994). Their explicit calculation using functional group contribution methods are very laborious not only because of the high number of components, but also because of the wide range of multifunctional organic compounds in the aerosol mixtures. On the contrary, empirical methods tend to simulate gas-to-particle partitioning based on fits of partitioning data derived from experimental observations. Frameworks like the 2-Dimensional Volatility Basis Set (2D-VBS) classify OA in terms of their bulk chemical characteristics based on the oxidation state (OS), the oxygen to carbon ratio (O:C) and volatility (Donahue et al., 2013, Donahue et al., 2012). Volatility is expressed based on the C* and used for separating the OA to volatile OA (VOC) ($6.5 < \log_{10}(C^*) < 9.5$), intermediate volatility OA (IVOC) ($2.5 < \log_{10}(C^*) < 6.5$), semi-volatile OA (SVOC) ($-0.5 < \log_{10}(C^*) < 2.5$), low volatility OA (LVOC) ($-3.5 < \log_{10}(C^*) < -0.5$) and extremely low volatility OA (ELVOC) ($-5.5 < \log_{10}(C^*) < -3.5$). A variety of the above newly developed techniques can be mapped onto the 2D-VBS and thus provide important experimental input to further develop and test both the empirical methods and the newly developed instrumentation.

Deviations between theoretical and experimental vapor pressure estimates are systematically observed. A characteristic example is the comparison of the experimental vapor pressures for straight-chain dicarboxylic acids compared to a variety of estimation methods as seen in

Figure 2 (Bilde et al., 2015) where results show orders of magnitude differences between the different model approaches. Furthermore, recent measurements show stronger enrichment of semi-volatile organic compounds in the particle- relative to the gas-phase than calculations based on equilibrium vapor pressure would suggest (Zhao et al., 2013a, Hohaus et al., 2015, Isaacman-VanWertz et al., 2016). It is currently unclear whether this is due to (i) uncertainties in the theoretical estimates of vapor pressures, (ii) thermal decomposition pathways affecting the experimental partitioning determination or (iii) the existence of uptake pathways to particles other than absorption e.g. adsorption or reactive uptake. The wide range of theoretical vapor pressure estimates combined with the large gas-to-particle partitioning discrepancies of the above techniques (Thompson et al., 2017) promote further studies in order to bridge the gap between theory and experiments.

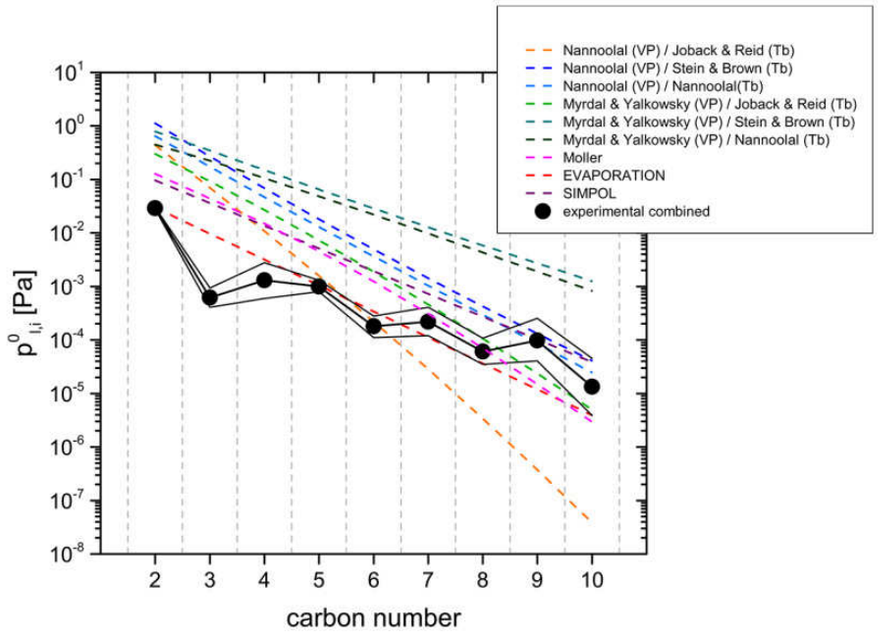

Figure 2: Comparison of experimental subcooled liquid saturation vapor pressures with the subcooled saturation vapor pressures obtained from a series of estimation methods for straight-chain dicarboxylic acids (Bilde et al., 2015).

1.5 Objective of this work

Owing to the current lack of understanding of partitioning of individual organic compounds in complex organic aerosol, this thesis is focused at the improvement and application of a measurement technique for direct determination of C* in SOA. To this end the ACM was automated (see Chapter 2) and deployed at the atmosphere simulation chamber SAPHIR (Rohrer et al., 2005) to investigate biogenic SOA (BSOA) formation and aging. Three different inlet techniques that utilize soft-ionization mass spectrometry, the Aerosol Collection Module (ACM) (Hohaus et al., 2010), the Chemical Analysis of Aerosol Online (CHARON) (Eichler et al., 2015) and the Collection Thermal Desorption Cell (TD) (Holzinger et al., 2010b) were used to compare the overall mass fraction these techniques were able to detect (section 4.1) combined with the comprehensive chemical characterization (section 4.2) and volatility trends (section 4.3). The gas-to-particle partitioning of major biogenic SOA oxidation products was investigated. The saturation mass concentration C* and thus the volatility measurements were calculated based on the mass concentration of individual species in the gas- and particle-phase (section 4.6). Results were implemented in the 2D-VBS (section 4.7) and compared to various explicit methods (section 4.8).

Chapter 2 Aerosol Collection Module development and optimization

In this chapter a description of the principle of operation and the operating conditions of the Aerosol Collection Module is provided (section 2.1). Details on the re-development, optimization and automation of the instrument via LabVIEW are presented in detail (section 2.2).

2.1 Instrument description

The Aerosol Collection Module (ACM) is an aerosol collection inlet with subsequent sample evaporation coupled to a gas-phase detector (Hohaus et al., 2015, Hohaus et al., 2010). It is designed for in situ, compound specific chemical analysis of the aerosol particulate-phase. A schematic of the ACM setup is provided in Figure 3. In brief, ambient air is sampled through an aerodynamic lens (Liu et al., 1995a, Liu et al., 1995b) with a flow rate of 80 ml min^{-1}. Within the aerodynamic lens the gas and particle phase of an aerosol are separated and the particles are collimated into a narrow beam. The particle beam is directed through a high

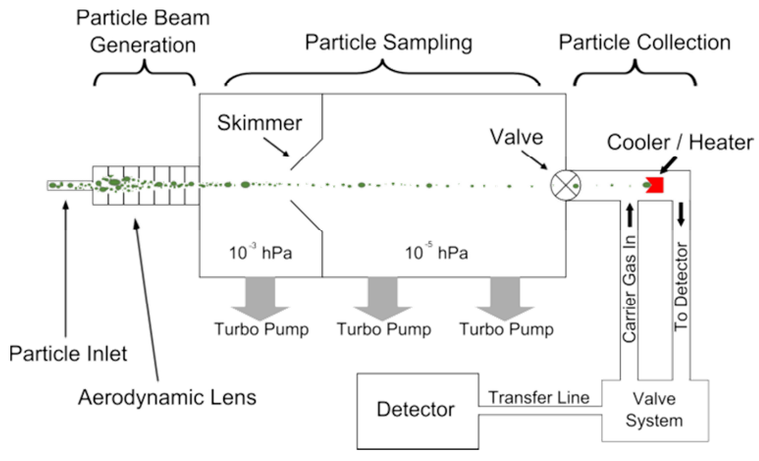

Figure 3: Schematic of the ACM instrument in collection mode (Hohaus et al., 2010).

vacuum environment (< 10^{-5} torr) to a cooled (~ -5 °C) sampling surface made of Siltek treated stainless steel. After collection is completed the particles are thermally desorbed by heating up the collector. The evaporated compounds are transferred to a gas phase detector through a coated stainless steel line of 0.8 mm inner diameter and 30 cm length, constantly kept at 280 °C. The design of the ACM allows for simultaneous measurement of the gas- and particle-phase organic species. During collection of the particle-phase on the collector, a bypass line is used for direct measurements of gas-phase organic compounds. In this work, the ACM was coupled to a PTR-ToF-MS (model PTR-TOF 8000; Ionicon Analytik GmbH, Innsbruck, Austria). Details on the operating principle of PTR-ToF-MS are provided in section 3.3.1.

The ACM is circulated through three different modes of operation, the standby, the collection and the desorption mode as seen in Figure 4. In the standby mode the collector surface is

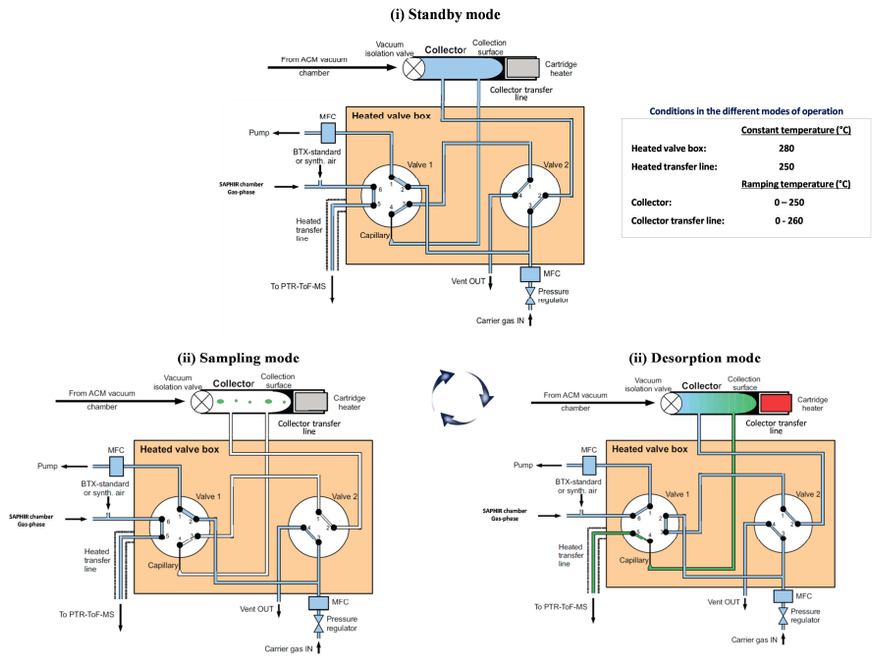

Figure 4: Schematic of the transfer valve system showing the connection scheme in (i) standby mode, (ii) sampling mode and (iii) desorption mode. The active gas flow is shown in blue and green. Green line shows the carrier gas with the desorbed particulate-phase.

cooled down to sub-zero temperatures. When this mode is initiated the collector is at the highest temperature, after desorption is finalized, thus cooling is required to reinitiate collection. To achieve the cooling of the collector a combination of a fan and a peltier element are used. The fan is operated to cool down the collector to 50 °C. After this temperature is achieved the peltier element is attached to the collector by using a lifter. This attachment assures the cooling of the collector down to sub-zero temperatures. Nitrogen is flashed through the collector and vented. The 6-port valve is switched to the PTRMS bypass line to perform gas-phase measurements. Depending on the ambient conditions, the standby mode requires around 15 to 20 minutes. When the system reaches low temperatures (~ 0 °C) collection mode is initiated. The vacuum isolation valve is opened and the collection cell is connected to the chamber and exposed to vacuum conditions achieved by the ACM turbo pump system. The surface of the collector is kept under cool conditions throughout the collection period to assure reduced evaporation of particulate-phase organic compounds from the collector to the gas-phase. Parallel to collection the PTRMS measures the mixing ratio of organic compounds in the gas-phase. Collection periods depend on the aerosol mass concentration in the sample. In this study a collection time of 4 h was used. After collection, the vacuum isolation valve is closed and the 4-port and 6-port valves are switched, connecting the PTRMS to the collector. The temperature of the collector is ramped up by 100 °C min^{-1} to a maximum of 250 °C stopping at different temperatures for 3 min. After the final temperature of 250 °C is reached, desorption time is extended for additional 7 minutes to ensure complete evaporation of the sample. The evaporated particle-phase compounds are transferred to the PTRMS using nitrogen as a carrier gas. More details on the operating conditions of the ACM for this study are provided in section 3.3.2.

2.2 Automation and performance optimization

Within this work, mechanical and electronic parts of the instrument were re-developed and optimized in order to reduce the losses of the evaporated aerosol on cool surfaces and automate the ACM, respectively. The automation was achieved via LabVIEW introducing a user friendly interface to monitor the performance of the instrument. In this section a detailed enumeration of these changes is provided.

During desorption particles evaporate to the gas-phase and are transferred from the collector to the valve box of the ACM and then to the detector. To avoid possible cold spots in the transfer lines from the collector to the valve box (Collector transfer line of Figure 4) special

copper plates were designed using the software INVENTOR (Figure B 1). Their design assured maximum cartridge heater to copper surface contact with fast response times since copper is a highly conductive material. A thermocouple was positioned to the minimum distance from the transfer line to provide reliable temperature feedback. Gas-phase compounds passed from the transfer line to the ACM valve box that was constantly heated at 280 °C. An additional line connecting the ACM valve box to the PTRMS (Heated transfer line of Figure 4) was optimized to the minimum possible length (15 cm). The temperature of the collector, the transfer copper plates, the valve box and the ACM-PTRMS line were temperature controlled via 5 PID controllers. Furthermore an instrument case was built to make the ACM portable with adjustable height depending on the size of the detector.

An electronic box was manufactured to power and control the individual devices. A LabVIEW NI X Series Multifunction Data Acquisition device (NI USB 6356) was connected to the electronic box and the ACM computer in order to achieve communication and control of all devices. In total 18 devices were automated using LabVIEW as seen in Figure 5. Software tools were generated to control 5 OMEGA PID controllers model CN7533, an OMEGA PID controller model CNi-3254-C24, a VICI E 90 4-

port valve, a VICI E 60-CE 6-port valve, a vacuum isolation valve, a Graupner rotor valve (DES 707 BBMG, No 7945), 3 Mass Flow Controllers (MFCs, Bronkhorst EL flow bus interface) and a fan. Furthermore, feedback communication was achieved for 3 turbo pumps (Agilent Technologies) and a pressure sensor (MKS, Baratron Pressure reader: 3XX04).

A graphical user interface (GUI) was built including 3 tabs: the “Settings”, the “ACM time-independent devices” and the “ACM time-dependent devices”. In the “Settings” the user can define the pathways where the data files will be stored and the timing and temperature steps of the PID controller heating the collector. All data are saved in TXT and CSV format in a similar structure to the one provided in Figure 5. For the valves, lifter, and fan, instead of storing the individual instrument status information concerning their position, the ACM mode of operation is recorded while their status is only constantly updated in the GUI.

In the “ACM time-independent devices” the user can set the values of the MFCs controlling the flow of nitrogen in the valve-box as well as the PID controllers heating the valve-box and the ACM-PTRMS heated transfer line (see Figure 4). Feedback and storage of the flows and temperatures is provided via an on-line graph interface with a time resolution defined by the user (“Saving time step” tab lower right side). Furthermore, the conditions of the turbo pumps

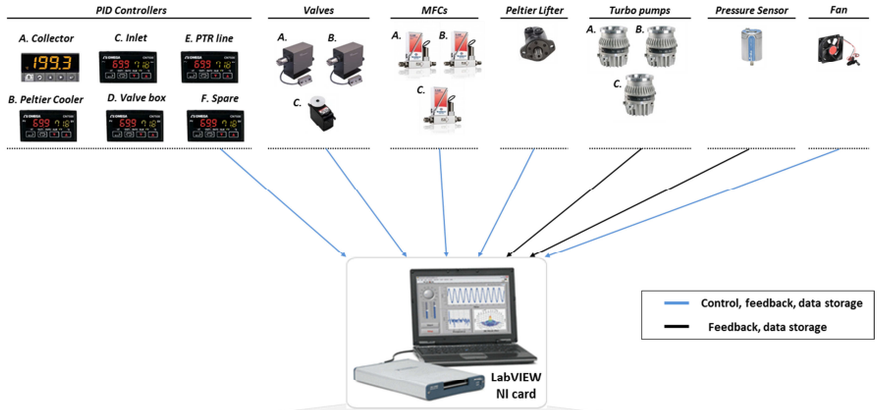

Date and time	Temperature (°C) A.	B.	C.	D.	E.	Valves (ON-OFF) A.	B.	C.	MFCs (cc)			Lifter (Up-Down)	Turbos (mAmps)			Pressure sensor (cc)	Fan (ON-OFF)
17.03.2017 12:00:00	100	-5	110	280	150	OFF	ON	OFF	300	200	800	DOWN	1347	1251	1280	80	OFF
17.03.2017 12:00:05	110	-5	120	280	150	OFF	ON	OFF	300	200	800	DOWN	1346	1250	1281	80	OFF
17.03.2017 12:00:10	120	-5	130	280	150	OFF	ON	OFF	300	200	800	DOWN	1348	1251	1279	80	OFF
. . .	.	.	.	.	.	.	.	.	.	.	.	.	.	.	.	.	.

Figure 5: Overview of the devices controlled via LabVIEW and the data output stored in txt format.

(operating rotational speed (Hz) and current (mA)) of the ACM together with the aerosol flow reaching the collector are recorded and updated in the interface with the same time resolution. The aerosol flow is calibrated based on the pressure drop occurring in the aerodynamic lens recorded by the pressure sensor. During operation, aerosol is introduced to the ACM vacuum with a flow of 80 ml min^{-1}. Flow drops would imply a clocked inlet. With the GUI the user can now get direct feedback on this flow rate in order to troubleshoot. All controlled devices included in this tab do not change set values during the changing modes of operation of the ACM.

Devices that require changes of their set point values when changing modes of operation are included in the final “ACM time-dependent devices” tab. Here the user can define the saving time step for data-storage, the time of particle collection on the collector and the collector temperature that the collector should reach in the standby mode before initiating the collection.

After all parameters are set, the user can press the “START ACM MODE CYCLES” button and the cycling of the ACM through the different modes of operation is initiated. Direct

feedback on the mode in which the ACM is operated, the position of the different valves, the operating conditions of the fan, the position of the peltier element lifter and the current and set point temperature values of the PIDs heating or cooling the collector and the PID heating the inlet line from the collector to the valve-box are provided and updated every second. This gives the user the ability to not only know the operating conditions of the ACM on-line but also check the history of the PID controllers operation from the constantly updated graphs.

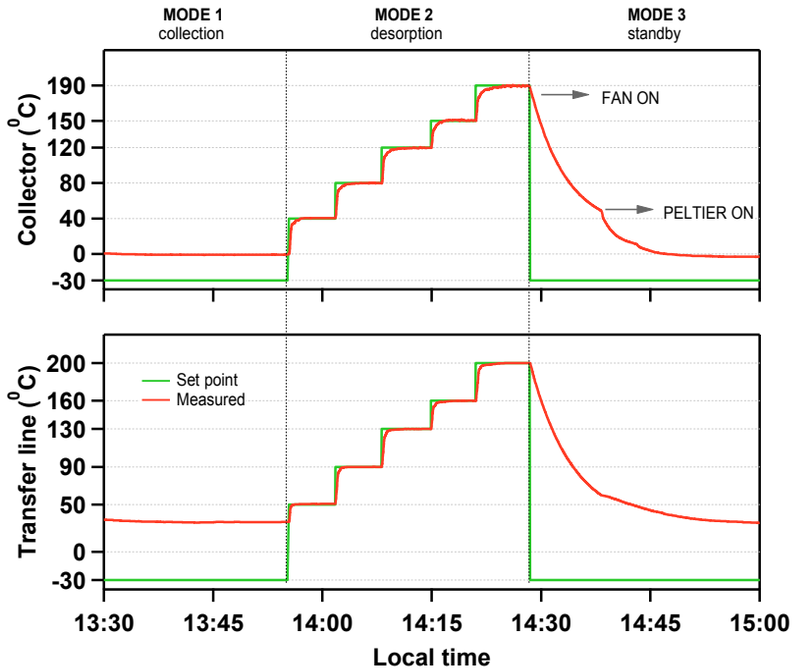

Figure 6: Temperature profile of the collector and transfer line during the different modes of operation of ACM.

A characteristic example to present the flexibility and fast response achieved via the ACM automation is given in Figure 6. After the collection time is finalized the ACM switches to the desorption mode where the collector is heated up using different temperature steps. In parallel to the heating of the collector the inlet line follows but with temperature steps 10 °C higher in order to avoid any cool spots in the transfer line. These 10 °C temperature difference can be controlled and changed by manually applying changes in the LabVIEW software. The heating of both the collector and the transfer line is achieved

fast (150 °C min^{-1}) due to the re-design of the copper plates. After desorption is completed the collector needs to cool down in order to initiate the next collection. To minimize the standby mode time a fan was installed blowing ambient air on the collector. The use of the fan successfully minimized the cooling time by a factor of 2. When using the ACM in environments of high humidity, during collection and while the collector is cooled down water can condense on the outer surface of the sub-cooled collector and generate a frost on the collector as seen in Figure B 2. In order to avoid possible damage of the lifter when changing from collection to desorption the automation was changed in the following; first the valves were switched when changing to desorption in order to connect the collector to the PTRMS. Then the collector was heated up to 20 °C to melt the frost and then the lifter was pushed down via the controlled rotor to disconnect the peltier element from the collector. This way it was ensured that the lifter was not harmed when forced to disconnect the peltier element from a frosted surface.

Chapter 3 Methods and Instrumentation

In the following details on the facilities (section 3.1), experimental conditions (section 3.2) and instrumentation (section 3.3) used during a campaign conducted in 2015 in the Institute of Energy and Climate Research, IEK-8: Troposphere in Forschungszentrum Jülich GmbH in Germany is provided. This campaign was performed in collaboration with partners from the Institut für Ionenphysik und Angewandte Physik from the University of Innsbruck in Austria and the Institute for Marine and Atmospheric research Utrecht, in the Netherlands. Aim of the campaign was to investigate SOA composition and atmospheric oxidation processes of biogenic VOCs with a focus on the gas-to-particle partitioning of major biogenic oxidation products. State-of-the art instrumentation (section 3.3) from the different collaborating groups was deployed in a joined effort to achieve a detailed chemical characterization of biogenic SOA. Instrument maintenance and data analysis performed from the different groups and used throughout this work is identified and presented in the next sections.

3.1 Facilities

Experiments were conducted in the atmospheric simulation chamber SAPHIR (Simulation of Atmospheric PHotochemistry In a large Reaction chamber) located in Jülich, Germany (Figure 7). The chamber consists of double-walled FEP Teflon foils with a volume of 270 m^3, resulting in a surface to volume ratio of approximately 1 m^{-1}. High purity nitrogen (99.9999% purity) is flushed at all times to the space between the foil and a pressure gradient (80 Pa overpressure) is maintained in order to prevent contamination from outside. Evaporation of high purity (> 99.9999%) liquid N_2 and O_2 is performed to prepare synthetic air. Exchange of air inside the chamber is done via controller systems. A high flow (max. 260 m^3 h^{-1}) is used to flush the chamber and reach clean starting conditions between each experiment while a small flow (max. of 15 m^3 h^{-1}) is used to replenish the chamber during experiments from losses due to leaks and the sampling of instruments. The chamber is equipped with a louvre system thus experiments can be performed under dark conditions focusing on O_3 and NO_3 oxidation (roof closed) or as photooxidation experiments utilizing sun light (roof open). Photolysis frequencies inside the chamber are ~ 80% of their outside values due to shadowing from the Teflon foil and structural elements holding the shutter system. High purity water (Milli-Q Gradient A10, Millipore Corp.) is heated to introduce humidity in the chamber by

mixing the water vapour to a large flow of synthetic air (260 m^3 h^{-1}). More details on SAPHIR can be found in Rohrer et al. (2005).

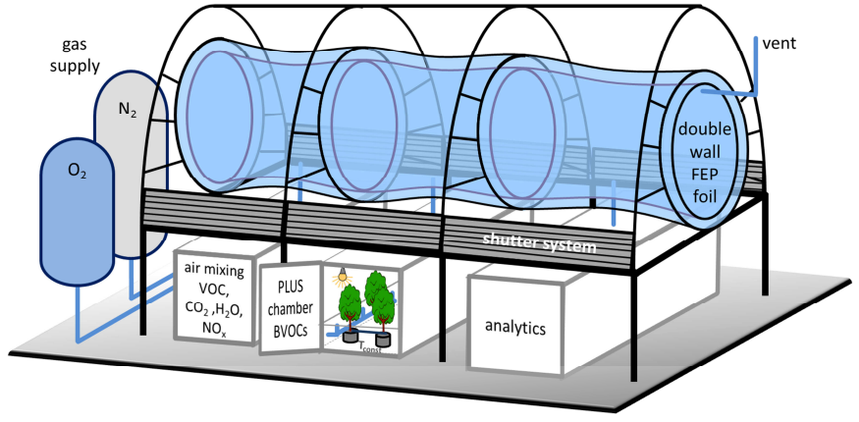

Figure 7: Schematic setup of the SAPHIR chamber (Copyright from Schmitt (2017)).

A PLant chamber Unit for Simulation (PLUS) has been recently coupled to SAPHIR to investigate the impact of real plant emissions on atmospheric chemistry (Hohaus et al., 2016). PLUS is an environmentally controlled, flow-through plant chamber where continuous measurements and adjustments of important experimental parameters (e.g., soil relative humidity, temperature, photosynthetical active radiation) are performed. To simulate solar radiation and control the tree emissions in PLUS, 15 light-emitting diode (LED) panels were used with an average photosynthetically active radiation value (PAR) of 750 mol m^{-2} s^{-1} and an average temperature of 25 °C. BVOC emissions were generated from 6 *Pinus sylvestris L.* (Scots pine) trees. Two air supply systems can be used for the gas supply of PLUS, a system utilizing cleaned and particle free outside air and the SAPHIR air supply. In this work, the SAPHIR air supply was used throughout all experiments.

A set of standard instrumentation was coupled to the simulation chamber SAPHIR. Air temperature was measured by an ultrasonic anemometer (Metek USA-1, accuracy 0.3 K) and humidity was determined with a frost point hygrometer (General Eastern model Hygro M4). NO and NO_2 measurements were performed with a chemiluminescence analyser (ECO

PHYSICS TR480) equipped with a photolytic converter (ECO PHYSICS PLC760). Ozone was measured by an UV absorption spectrometer (ANSYCO model O341M).

3.2 Experimental procedure

The simulation chamber SAPHIR was used for the formation of SOA from the ozonolysis of different monoterpenes. A high flow (150 to 200 $m^3 h^{-1}$) of air was introduced in order to clean the chamber and reach aerosol and trace gases concentrations below detection limits before each experiment was initiated. A low flow (8 $m^3 h^{-1}$) was used to replenish SAPHIR during experiments from losses due to leaks and sampling of the instruments. The chamber was initially humidified (55% RH, 295 – 310 K) and background measurements for all instruments were performed. CO_2 was added (20 ppm) and used as a dilution tracer. Experimental starting conditions varied from the injection of β-pinene and limonene, as single compounds or as a mixture, to the injection of real plant emissions from 6 Pinus sylvestris L. (Scots pine), provided from SAPHIR-PLUS (Section 3.1). For the tree emissions experiment the BVOCs consisted of 42% δ^3-carene, 38% α-pinene, 5% β-pinene, 4% myrcene, 3% terpinolene and 8% other monoterpenes, as determined by GC-MS measurements. Monoterpenes were injected either with a Hamilton syringe injection and subsequent evaporation into the replenishment flow of SAPHIR, or by SAPHIR-PLUS (real tree emissions). An overview of the experiments is given in Table 1 and presented in further detail in Figure 8. After background measurements were performed for all instruments,

Table 1: Experimental conditions for each experiment. For all experiments SOA formation is achieved from the ozonolysis of the precursors. The chamber temperature corresponds to the average temperature throughout each experiment indicating the ± 1σ of the average. For the tree emissions experiment there were two VOC injection periods.

Experiment	**Monoterpenes (ppbV)**	**Ozone (ppbV)**	**Duration (h)**	**Maximum SOA formed ($\mu g/m^3$)**	**Chamber temperature (°C)**	**SOA aging Conditions**
β-Pinene	120	700	34	130	20 ± 4	Photochemical oxidation for 10 h
Limonene	25	150	17	50	17 ± 4	Continuous NO_3 oxidation for 8 h
β-Pinene/Limonene mixture	60/12	300	26	60	19 ± 5	Photochemical oxidation for 4 h
Tree emissions 1^{st} inj. / 2^{nd} inj.	65/10	300	30	80	30 ± 5	Photochemical oxidation for 6 h

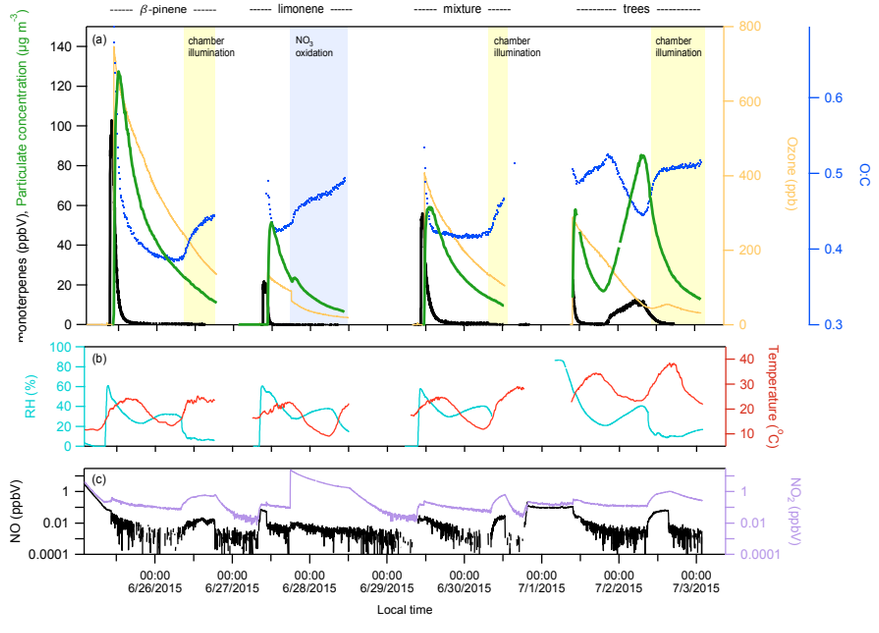

Figure 8: An overview of all experiments during the campaign with (a) corresponding to the mixing ratios of the injected monoterpenes (black line) and ozone (orange line) as well as the SOA mass produced (green line) and its O:C ratio (measured from the AMS) as an indicator of the oxidation of the SOA. Background colours correspond to the opening of the roof (yellow) or the NO_3 oxidation initiation (blue colour). Measurement of the RH (ciel), temperature (red), NO (black) and NO_2 (purple) are also provided.

lasting for one hour, ozone was introduced in the system to initiate chemistry. The ozonolysis of monoterpenes and the tree emissions were performed under low NO_x conditions (10 – 100 pptV) and in the absence of an OH scavenger. For the limonene experiment, 8 hours after the ozone injection, an addition of 30 ppbV of NO_2 was introduced into the dark chamber. The reaction of NO_2 with remaining ozone in the chamber resulted in the generation of NO_3, thus initiating the NO_3 oxidation chemistry. In all other experiments the chamber was illuminated ~20 hours after the ozone injection, exposing the SOA to real sunlight, thus initiating photo-oxidation by OH radicals. Further oxidation of the SOA was reflected by the increase of the oxygen to carbon ratio, measured from the AMS (details in section 3.3.5). Finally, for the real tree emissions, after 11 hours of ozone exposure, additional BVOCs were introduced into the SAPHIR chamber to generate fresh SOA which was subsequently aged by photooxidation for

additional 6 hours. The duration of the experiments varied from 17 to 36 hours, providing ample time to experimentally investigate the aging of the biogenic SOA.

3.3 Instrumentation

Three independent aerosol chemical characterization techniques utilizing a PTR-ToF-MS were used to measure SOA composition, the aerosol collection module (ACM – PTR-ToF-MS, referred to as "ACM" hereafter), the chemical analysis of aerosol online (CHARON – PTR-ToF-MS, referred to as "CHARON" hereafter) and the collection thermal desorption unit (TD – PTR-ToF-MS, referred to as "TD" hereafter). Their characteristics and differences

Table 2: Instruments operating conditions (Gkatzelis et al., 2017).

INSTRUMENT CHARACTERISTICS	**ACM (in situ)**	**CHARON (online)**	**TD (in situ)**
Time resolution (min)	240	1	120
Gas/particle separation	High vacuum	Denuder	Denuder and/or blank correction (filtered air)
Pre-concentration factor	3	44	10000[a]
LOD[b] (ng/m^3)	250[c]	1.4[d]	0.001[a]
Desorption temperature(°C)	25 – 250	140	25 – 350
Heating rate (°C / min)	100	0	15
Temperature steps (°C)	100, 150, 250 (3 min)	none	None
Desorption pressure (atm)	1	< 1	1
Particle size (nm)	70 – 1000	70 – 1000	70 - 2000
PTR-ToF-MS E/N (Td)	120	65 / 100	160
PTR-ToF-MS mass resolution (m/Δm)	2500	4500-5000	4000

[a] based on 30 min sampling at 9 L/min and 3 min desorption at 9 mL/min (Holzinger et al., 2010a)

[b] Limit of detection

[c] For signal on *m/z* 139 and 10 sec integration time

[d] For signals around *m/z* 200 and 1 min integration time

are provided in Table 2 and discussed in detail in this section. The time resolution of the techniques varied from CHARON providing online measurements to the TD and ACM deployed with collection times of 120 and 240 min, respectively. CHARON was operated at a constant desorption temperature and lower pressure (< 1 atm) while ACM and TD, operated at 1 atm, introduced temperature ramps during desorption thus providing more detailed volatility information. The limit of detection (LOD), dependent on the different pre-concentration factors for each technique, resulted in TD having the lowest LOD of 0.001 ng m^{-3}, followed by the CHARON with 1.4 ng m^{-3}, while ACM showed the highest values with 250 ng m^{-3}. More details on the operating conditions of the different instrumentation is provided in detail in the following.

3.3.1 Proton Transfer Reaction-Time of Flight-Mass Spectrometer

The Proton Transfer Reaction-Time of Flight-Mass Spectrometer (PTR-ToF-MS) is a high resolution mass spectrometer that has been previously extensively described (Graus et al., 2010, Jordan et al., 2009, de Gouw and Warneke, 2007) and only the major working principle will be discussed here. In brief, the instrument allows simultaneous real-time monitoring of volatile organic compounds (VOCs) by using a soft ionization technique. It is divided in three major parts as seen in Figure 9: an ion source, a drift tube and the time-of-flight section prior to detection. Protonated water H_3O^+ is used as a primary ion, generated in the ion source from distilled water vapor through an electrical discharge. In the drift tube VOCs coming from the

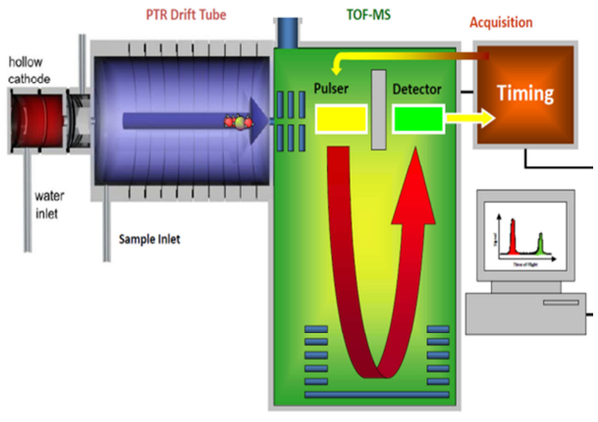

Figure 9: PTR-ToF-MS set-up developed by IONICON Analytik (Jordan et al., 2009).

sample inlet and H_3O^+ interact resulting in a proton transfer from the hydronium to the trace gas molecule. The protonated and therefore ionized molecule is directed through the ToF section and detected by the mass spectrometer. Only compounds with a proton affinity larger than the proton affinity of water can be ionized using this technique and thus be detected.

PTR-ToF-MS is considered a soft chemical ionization technique that preserves in many cases the chemical structure of the VOC during ionization. For a non-dissociative proton transfer, the detected VOC-H^+ directly reflects the atomic composition of the respective VOC. A characteristic example of the separation capabilities and chemical formula attribution of the PTR-ToF-MS is provided in Figure 10 (taken by Graus et al. (2010)). In the lower unit mass a clear separation of protonated acetone to protonated glyoxal is achieved while for the example of the higher unit mass of 143, multiple peaks are identified. A separation by 0.036, which corresponds to the mass difference of CH_4 (16.0308 u) and O (15.9944 u) is observed for neighboring peaks. This mass difference indicates that the unknown compounds at nominal mass 143 can be assigned to different isobaric oxygenated hydrocarbons containing different oxygen atom number.

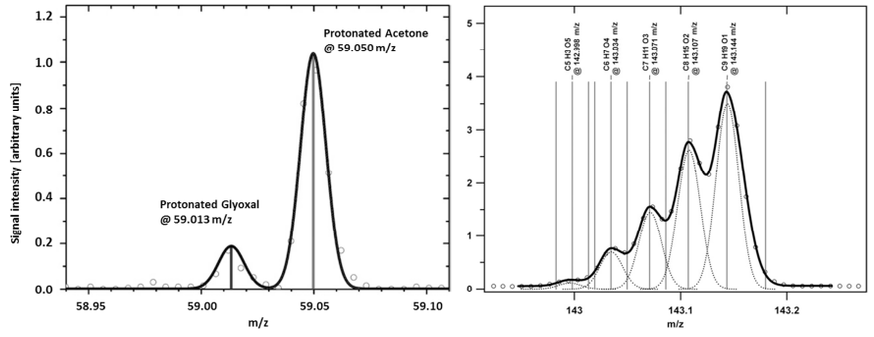

Figure 10: Characteristic example of measured ion signal (open circles) of PTR-TOF with a multi-peak fit (black line) and contributing peaks (dotted lines) along with matching candidates for $C_xH_yO_z$ assignment (vertical lines) from (Graus et al., 2010) for the 59 and 143 unit mass.

Concentrations of the individual identified species can be derived from the respective peak area under the fitted curve thus providing time series of the counts per second (cps) per ion identified. All integrated signals are then normalized to the H_3O^+ signal to derive the normalized cps (ncps). In order to determine the mixing ratio in parts per billion by volume

(ppbV) the sensitivity of the PTRMS to the detected ions is required. This is performed by calibrating the instrument with compounds of known concentration in the gas-phase. The expression to derive from ncps the ppbV is thus given as

$$\mathrm{ppbV}_i = \frac{\mathrm{cps}_i}{\mathrm{H_3O^+}} \times \frac{1}{S_i} \quad (5)$$

where S_i is the sensitivity of a calibrated compound i. Since hundreds of ions are detected with a PTR-ToF-MS calibration for each compound is not possible. For uncalibrated compounds different approaches have been used in order to derive their sensitivities. These approaches and their uncertainties are discussed in detail in the next sections.

Although when compared e.g. to electron impact ionization techniques, PTR-ToF-MS is considered a soft ionization instrument, compounds can still undergo fragmentation. Depending on the molecular structure of the compound, preferential split-up of certain molecular bonding can occur, thus making certain fragmentation pathways more probable than others. Furthermore, conditions in the drift tube chamber that define the probability for an ion to release its excess free energy through collision with other molecules play a key role to the extent of fragmentation in this type of systems. These drift tube chamber conditions are determined by the E/N ratio accounting for the electric field strength (V cm^{-1}) to buffer gas density (molecules cm^{-3}) in units of Townsden (Td = 10^{-17} V cm^2). Lower E/N set values result in longer ion residence times in the drift tube of the PTR-ToF-MS thus higher sensitivity due to enhanced proton transfer reaction times (de Gouw and Warneke, 2007). Ions are introduced to a lower kinetic energy system, thus resulting in reduced fragmentation during ionization while the cluster ion distribution is changed when lowering the E/N, supporting more $H_3O^+(H_2O)_n$ (n=1,2,3..) cluster ion generation. Since the proton affinity of $H_3O^+(H_2O)_n$ is higher than that of H_3O^+, a certain range of organic compounds cannot be ionized in such operating conditions. In particular, most oxygenated VOCs would still react efficiently with both H_3O^+ and $H_3O^+(H_2O)_n$ ions but for aromatic compounds reactions with $H_3O^+(H_2O)_n$ would be less efficient and the sensitivity for this compound class would decrease.

Four PTR-ToF-MS instruments (model PTR-TOF 8000; PTR-ToF-MS, Ionicon) were deployed in this campaign, one coupled to the ACM (section 3.3.2), one coupled to the CHARON (section 3.3.3), one coupled to the TD (section 3.3.4) and one dedicated to gas-phase measurements. ACM, CHARON and TD measured organic compounds in the particle-phase by evaporating the particles to the gas-phase and detecting them with a PTRMS. Different methods to derive the mass concentration of the evaporated to the gas-phase OA

were performed and discussed in detail in the next sections. By combining the chemical formula information and the mass concentration of all detected species, overall parameters for the bulk OA like the oxygen to carbon (O:C) ratio were determined based on the contribution of each species and their individual O:C. Operating conditions of each PTR-ToF-MS together with the principle of operation of the different aerosol inlets together with AMS and SMPS are provided in the following sections.

Operation and calibration of the PTR-ToF-MS dedicated to the measurement of VOCs and their gas-phase oxidation products was performed by Zhujun Yu. This instrument was operated at E/N = 120 Td. Calibrations were performed with the exact same approach as for the ACM-PTR-ToF-MS described in detail in section 3.3.2. Data analysis was performed using the software PTR-TOF Data Analyzer (version 4.40) (Müller et al., 2013).

3.3.2 ACM-PTR-ToF-MS

Details on the operating conditions of the ACM-PTR-ToF-MS are provided in this section. The principle of operation of both ACM and PTR-ToF-MS were introduced previously (section 2.1 and 3.3.1, respectively). The collection time of aerosol on the ACM collector was chosen to be 4 h in this study. The particles were thermally desorbed by heating up the collector. The evaporated compounds were transferred to the PTR-ToF-MS through a coated stainless steel line of 0.8 mm inner diameter and 30 cm length constantly kept at 300 °C. Nitrogen was used as carrier gas with a flow of 300 ml min^{-1}, resulting in a residence time in the ACM of 60 ms. The collector temperature was ramped by 100 °C min^{-1} to a maximum of 250 °C, with 3-minute isothermal sections at 100 °C, 150 °C and 250 °C, respectively. During the final temperature step of 250 °C, desorption time was extended for additional 7 minutes to ensure complete evaporation of the sample. These temperature steps provided enough time for compounds to undergo evaporation. The signal dropped close to zero before each temperature step was completed (example case in Figure 11), making the ACM-PTR-ToF-MS ideal for compound specific volatility trend analysis. Parallel to the ACM particulate-phase collection, a bypass line was used, coupled to the same PTR-ToF-MS, measuring the gas-phase during particle phase sampling time. An example of the gas- and particulate-phase measurements is given in Figure 11. During the campaign, the aerosol-phase sampling line was a stainless steel line (total length: 4 m, OD: 1/4') with a flow of 0.7 L min^{-1} resulting in a residence time of approximately 3 seconds.

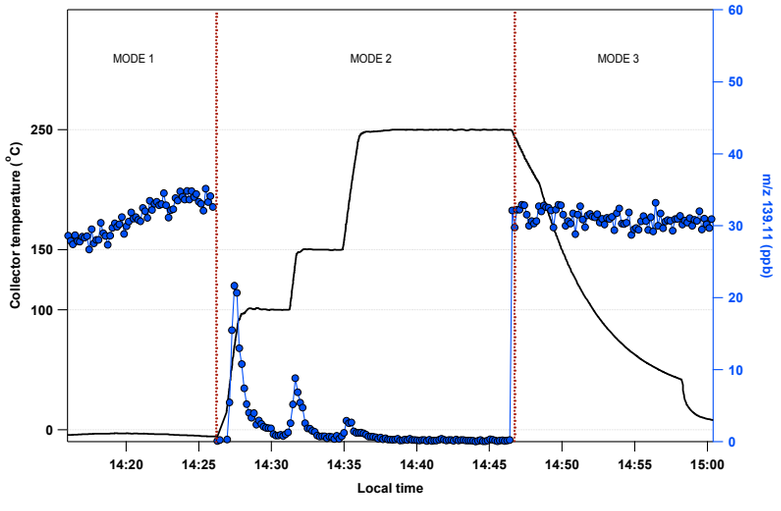

Figure 11: Different modes of operation of the ACM-PTR-ToF-MS during the β-pinene ozonolysis experiment. Left axis correspond to the temperature of the collector and right axis to the ppb's measured for *m/z* 139.11 (corresponding to nopinone) with time. MODE 1 indicates the particulate phase collection on the cooled ACM collector and the parallel gas phase measurements of the PTR-ToF-MS. MODE 2 is the desorption of particulate phase compounds from the collector at the different temperature steps and MODE 3 corresponds to gas phase measurements and the intermediate step of cooling down the collector in order to initiate the next collection.

Assuming a collection efficiency of 100% (Hohaus et al., 2010) for all particles in the aerosol sample, measured PTR-ToF-MS signals could be converted to particulate mass concentrations by applying PTR calibrations as described in the following. Normalization of the PTR-ToF-MS cps was performed based on the H_3O^+ signal, as previously discussed (section 3.3.1). The ACM was corrected for mass discrimination accounting for transmission efficiency corrections for the PTRMS. The mass discrimination function was determined based on the ratio of the measured over the theoretical sensitivity of acetaldehyde, acetone, butanone, benzene, toluene, xylene and mesitelyne. The instrument was calibrated for a total of 15 compounds including aromatics (benzene, toluene, xylene, chlorobenzene), oxygenates (acetaldehyde, acetone, 2-butanone, 3-pentanone, MVK, nopinone, methanol, 1-butanol), pure hydrocarbons (isoprene, α-pinene) and acetonitrile as seen in Table A 1. Calibration was performed by coupling the PTR-ToF-MS to a calibration unit (LCU, Ionicon Analytik GmbH, Innsbruck, Austria) and measuring known concentration of the compounds in the gas-phase. For signals observed at uncalibrated masses the average sensitivity of acetaldehyde,

acetone, MVK, Butanon, pentanone and nopinone was applied resulting in 15 ncps/ppb and an uncertainty of ± 50% (± 1σ). The mass concentration of an aerosol compound i in the air sample was calculated based on the mixing ratios the PTR-MS measures:

$$C_{aer,i} = \frac{n_{mean,i} \times MW_i \times P}{T \times R} \times \frac{F_{N_2} \times t_{meas}}{F_{col} \times t_{col}}, \quad (6)$$

where $C_{aer,i}$ is the aerosol concentration of compound i in µg m^{-3}, $n_{mean,i}$ is the arithmetic mean of the mixing ratio during the aerosol analysis in the nitrogen flow in ppbV when accounting for the signal above the instrument noise (> 2σ), MW_i is the molecular weight of compound i in g mol^{-1}, P is the ambient pressure in atm, R is the universal gas law constant, T the ambient temperature of the SAPHIR chamber in Kelvin, F_{N_2} the flow of the carrier gas of 300 mL min^{-1}, t_{meas} the aerosol desorption duration of 20 min (when all signal is > 2σ), F_{col} the collection flow rate of the aerosol to the ACM of 80 mL min^{-1} and t_{col} the aerosol collection duration of 240 min. The volume ratio correction $\left(\frac{F_{N_2} \times t_{meas}}{F_{col} \times t_{col}}\right)$ was applied in order to account for the ACM collection preconcentration step. The mass concentration was calculated by taking into account only the signal above the instrument noise (> 2σ) for each compound at each desorption.

Background measurements were performed before and after every experiment (~ 2 times per day) by heating up the collector, without depositing particles on the surface beforehand. The signal derived from the background measurements at each temperature step was then interpolated and subtracted from all desorptions for all compounds. Two major factors could affect the background signal, gas-phase interference and aerosol residual remaining at the collector after each desorption cycle. Due to the aerodynamic lens set-up the ACM design prevents gas-phase contamination (removal > 99.9999%). Background measurements throughout this study show no residual compounds on the collector in the temperature range studied.

PTR-ToF-MS operation conditions were kept constant throughout the campaign. It was operated at E/N = 120 Td. The drift tube was kept at a temperature of 100 °C and a pressure of 2.30 mbar. The mass resolving power of this PTR-ToF-MS was m/Δm ~ 2500 (Δm is full width at half maximum). Mass spectra were collected up to *m/z* 400 at 10 s signal integration time. Analysis of the raw data was performed using the PTR-TOF Data Analyzer (version 4.40) software (Müller et al., 2013). In brief, an integration time of 90 s was chosen for the software and *m/z* calibration peaks were assigned based on the peaks of 21.02, 59.05 and 180.94 accounting for $H_3[18O]^+$, protonated acetone and trichlorobenzene respectively.

Trichlorobenzene was used as an internal standard throughout the campaign. The chemical composition assignment was derived from the measured exact mass assuming a molecular formula of $C_xH_yO_zN_a$ and attributing the isotopic pattern when possible.

3.3.3 CHARON-PTR-ToF-MS

The analyzer deployed by the University of Innsbruck consisted of a Chemical Analysis of Aerosol Online (CHARON) inlet interfaced to a PTR-ToF-MS.

A schematic of the CHARON inlet is provided in Figure 12. The CHARON inlet (Eichler et al., 2015) consists of a gas-phase denuder for stripping off gas-phase analytes, an aerodynamic lens for particle collimation combined with an inertial sampler for the particle-enriched flow, and a thermodesorption unit for particle volatilization prior to chemical analysis. The monolithic charcoal denuder (Mast Carbon International Ltd., Guilford, UK) used in this study was 25 cm long, had an outer diameter of 3 cm and a channel density of 585 channels per inch (cpi). The denuder was tested to efficiently remove all gas-phase compounds with an efficiency > 99.999% and to transmit particles in the range from 100 to 750 nm with a 75-90% efficiency. The thermodesorption unit consisted of a heated Siltek®/Sulfinert®-treated stainless steel tube kept at a temperature of 140 °C and a pressure on the order of a few mbar. A HEPA filter (ETA filter model HC01-5N-B, Aerocolloid LLC, Minneapolis, MN, USA) was periodically placed upstream of the gas-phase denuder for determining the instrumental background. More details on the performance of the CHARON inlet are given in Eichler et al. (2015).

The CHARON inlet was interfaced to a commercial PTR-ToF-MS instrument (model PTR-TOF 8000; Ionicon Analytik GmbH, Innsbruck, Austria). PTR-ToF-MS mass spectra were collected up to *m/z* 500 at 10 s signal integration time. The PTR-TOF Data Analyzer (version 4.40) software was used for data analysis (Müller et al., 2013). During the tree emissions experiment the electric field applied to the drift tube was periodically switched in 300 s intervals, i.e. measurements were performed at alternating E/N-values of 65 Td (referred to as "$CHARON_{65}$" hereafter) and 100 Td (referred to as "$CHARON_{100}$" hereafter), respectively (1 Td = 10^{-17} V cm^{-2} $molecule^{-1}$). For all other experiments the E/N-value analysed was at 100 Td. The drift tube was kept at a temperature of 120 °C and a pressure of 2.40 mbar. Continuous permeation of 1,2-diiodobenzene was performed into the drift tube for generating mass axis calibration signals at *m/z* 203.943 and *m/z* 330.847. The PTR-ToF-MS was calibrated using the same 16-compound gas mixture as the ACM (Table A 1) that included

aromatics (benzene, toluene, o-xylene, mesitylene, chlorobenzene), oxygenate compounds (acetaldehyde, acetone, 2-butanone, 3-pentanone, MVK, nopinone, methanol, 1-butanol), pure hydrocarbons (isoprene, α-pinene) and acetonitrile. The mass resolving power of this PTR-ToF-MS was m/Δm 4500-5000.

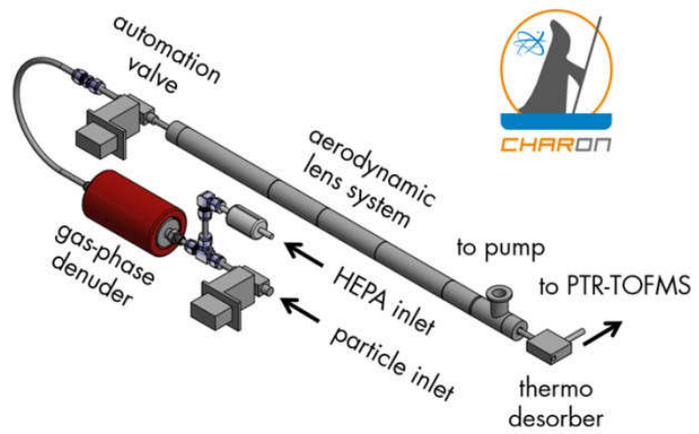

Figure 12: Schematic of the CHARON instrument (Eichler et al., 2015).

A sensitivity model based on Su and Chesnavich's parameterized reaction rate theory (Bosque and Sales, 2002, Su and Chesnavich, 1982) and a chemical composition based parameterization of polarizabilities at a constant dipole moment of μ_D = 2.75 D (between 1 – 4.5 D for most oxygenated organic compounds) (Cappellin et al., 2012) was applied to calculate sensitivities of unknown compounds. This resulted in an *m/z* independent sensitivity accuracy of about ± 25%. For compounds without assigned elemental composition the polarizability of acetone was applied with an accuracy of ± 40%. The entire CHARON setup was calibrated for particle-phase transmission and pre-concentration estimation using size-selected ammonium nitrate particles as described in Eichler et al. (2015). Derived volume mixing ratios were transformed to mass concentrations using the molecular *m/z* information at Normal Temperature and Pressure (NTP) conditions (293.15 K, 101.325 kPa). Quantification was hampered by two events (power failure, partial obstruction of the aerodynamic lens) which resulted in a higher than usual variability of the particle enrichment

in the aerodynamic lens. Results from two experiments (limonene ozonolysis/NO_3 oxidation and limonene/β-pinene mixture ozonolysis) were particularly affected as will be shown and discussed in section 4.1.

The CHARON-PTR-ToF-MS setup was interfaced to the SAPHIR chamber using Siltek®/Sulfinert®-treated stainless steel tubing (total length: 600 cm, 50 cm extending into the chamber, ID: 5.33 mm). During the β-pinene ozonolysis and limonene ozonolysis/NO_3 oxidation experiments, the inlet flow was kept at 0.6 l min^{-1} resulting in a sample residence time of 13.4 s. During the β-pinene/limonene mixture ozonolysis and the real tree emissions ozonolysis experiments, the inlet flow was increased to 1.6 l min^{-1} resulting in a sample residence time of 5.0 s.

Operation of the CHARON was performed by Dr. Phillip Eichler. Dr. Markus Müller provided the analyzed data in µg m^{-3} and performed additional laboratory characterization experiments using the CHARON, to further support the results of this work.

3.3.4 TD-PTR-ToF-MS

The Thermal-Desorption unit was coupled to a commercial PTR-TOF8000 instrument (Ionicon Analytik GmbH, Austria). The TD is a dual aerosol inlet system consisting of impact collection thermal desorption cells as seen in Figure 13. The setup was already used in several campaigns as described by Holzinger et al. (2013), (2010a).

In short, the centrepiece of both aerosol inlets is a Collection Thermal Desorption cell (CTD, Aerosol Dynamics, Berkeley, CA, USA), on which humidified ambient particles in the size range of 70 nm to 2 µm at an air sample flow rate of ~ 6 L min^{-1} are collected by impaction onto a stainless steel collection surface using a sonic jet impactor. The humidification of the aerosol sample flow to approximately 70% is achieved by a Nafion based humidifier and reduces particle rebound. All tubing in contact with volatilized aerosol compounds (i.e. the CTD cell, and all transfer tubing and valves) is coated to increase the chemical inertness of the surface. The CTD cell coating is AMCX (AMCX, L.L.C., Lemont PA, USA); all other parts received the Siltek®/Sulfinert®- treatment. The transfer lines are operated at elevated temperatures of 200 ℃ to avoid re-condensation of desorbed aerosol compounds.

In this study, aerosols were sampled from the chamber through a ~5 m long copper line (ID=6.5 mm). The operation of the system was fully automated. One cycle was completed in 2.5 h and included the analysis of (i) the first aerosol inlet (namely inlet A), (ii) the second aerosol inlet (namely inlet B), (iii) inlet A and (iv) inlet B that sampled particle-filtered

chamber air, and (v) the analysis of gas-phase in conventional PTR-MS mode. The duration

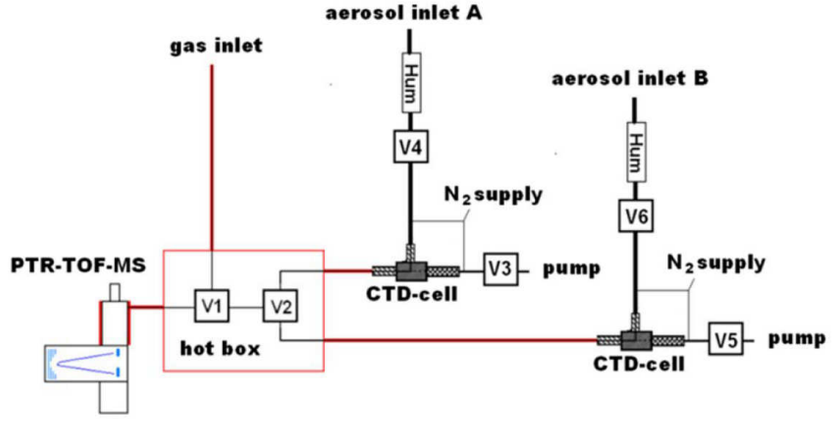

Figure 13: Schematic of the TD instrument from Utrecht University (Holzinger et al., 2013).

of each section was 30 min. Due to lab air contamination the conventional PTR-MS gas-phase measurements of the chamber air were not available from the TD-PTR. In addition, inlet A data quality was affected by a systematic change of the PTR-MS conditions (E/N fluctuation during background measurements caused by a malfunctioning valve). Consequently, inlet A data were excluded from this campaign and only data for aerosol composition derived from inlet B is used.

The aerosols were pre-concentrated onto the CTD cell for 30 min with a flow of 6 L min^{-1} before thermal desorption into the PTR-MS. After collection, a small flow of ~ 10 mL min^{-1} of nitrogen carrier gas transported all compounds desorbing from the CTD cell directly into the PTR-MS. Aerosol compounds were thermally released from the CTD-cell by ramping the temperature from room temperature (normally, 25 ℃) up to 350 ℃. Temperature ramped continuously at a rate of ~15 ℃ min^{-1} for ~21 minutes until 350 ℃ was reached followed by a dwell time of 3 minutes (at 350 ℃). After a cool down period of 6 min a new collection was initiated. For the last experiment (tree emissions), a denuder was installed on inlet B to constrain a possible artefact from gas-phase compounds adsorbing on the CTD cell.

The aerosol background was measured every other run by passing the airstream through a Teflon membrane filter (Zefluor 2.0 µm, Pall Corp.) that removed the particles from the air stream (sections: iii and iv mentioned above). The effective removal of particles was confirmed by test measurements with a condensation particle counter (TSI, WCPC

Model 3785). While particles are removed by the Teflon filter, gas-phase compounds should be less affected. Filter samples to determine the aerosol background have been taken in turns: in each cycle, inlet A and inlet B sampled successively for 30 min of each, then the samples collected through the two inlets were analysed successively as well.

The PTRMS measures mixing ratios of compounds desorbed from aerosols in a nitrogen carrier gas. The mass concentration of an aerosol compound in the air sample under ambient pressure (1 atm) is calculated according to

$$C_{aer,i} = n_{mean,i} \times MW_i \times \frac{F_{N_2} \times t_{meas}}{22.4 \times F_{col} \times t_{col}}, \quad (7)$$

where $C_{aer,i}$ is the aerosol concentration of compound i in µg m^{-3}, $n_{mean,i}$ its (arithmetic) mean mixing ratio during the aerosol analysis in the nitrogen carrier gas in nmol mol^{-1}, MW_i the molecular weight of compound i in g mol^{-1}, F_{N2} the flow of the carrier gas in standard liters per minute, t_{meas} the duration of the aerosol measurement in minutes, F_{col} the flow rate at which the aerosols are collected in standard liters per minute, t_{col} the duration of aerosol collection in minutes and 22.4 the volume which one mole of an ideal gas will occupy in liters. It should be noted that equation 7 assumes a temperature of 0 °C thus overestimating the aerosol mass concentration observed by approximately 5 to 10 % in this study. Mixing ratios of most compounds were calculated according to the method described in Holzinger et al. (2010b), which involves the use of default reaction rate constants (3×10^{-9} cm^3 s^{-1} $molecule^{-1}$).

Specific conditions of the PTR-ToF-MS during the campaign were as follows: E/N = 1.6×10^{-19} V m^2 $molec^{-1}$ (i.e. 160 Td) to ensure ionization only by H_3O^+, temperature of the drift tube Td = 120 °C, and a mass resolution of $m/\Delta m \approx 4000$.

Mass spectra were obtained on a 5s time resolution. The data were processed using the PTRwid software (Holzinger, 2015). The software has several unique features including autonomous and accurate calibration of mass scale and the export of a uniform peak list which avoids the same ion being attributed to a slight different mass within the limits of precision. In total, 543 organic ions represented in the “unified mass list” have been obtained and used for all experiments in this campaign.

Operation of the TD was performed by Dr. Kang-Ming Xu and Prof. Rupert Holzinger. Data were analyzed in µg m^{-3} for each desorption cell at each temperature during desorption by Dr. Kang-Ming Xu. No additional background corrections were applied.

3.3.5 Aerosol Mass Spectrometer

A High-Resolution Time-of-Flight Aerosol Mass Spectrometer (HR-ToF-AMS, hereby called AMS) (Canagaratna et al., 2007, DeCarlo et al., 2006) was used to quantify and identify the chemical composition of the aerosol. Components measured from an AMS are the total organic mass and the major inorganic species ammonium, sulphate, nitrate, chloride and particulate water. The AMS schematic is provided in Figure 14 while the principle of operation has been described in detail by Canagaratna et al. (2007).

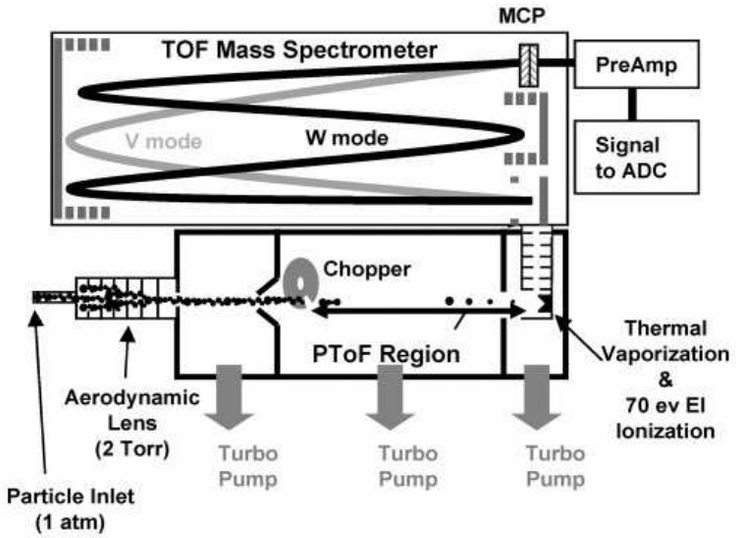

Figure 14: Schematic of the HR-ToF-AMS (Canagaratna et al., 2007).

In brief, aerosols are sampled through an aerodynamic lens (Liu et al., 1995a, Liu et al., 1995b), focused into a narrow beam, and transmitted through a vacuum chamber where they are flash-vaporized by impaction on a heated surface. Electron impact ionization (70 eV) of the evaporated species is performed with subsequent detection through the time of flight mass spectrometer. AMS follows a similar principle of operation as the ACM as they share a similar aerodynamic lens and vacuum chamber. AMS organic mass concentration for this study was provided with an accuracy of 31% (Aiken et al., 2008). High resolution mass spectra were analyzed using the software packages SQUIRREL (v1.57) and PIKA (v1.15Z).

Oxygen to carbon ratios were calculated based on the newly developed “Improved-Ambient” method by Canagaratna et al. (2015).

Operation and data analysis of the AMS was performed by Sebastian Schmitt who provided the organic time series in μg m^{-3} together with the O:C calculations.

3.3.6 Scanning Mobility Particle Sizer

Particle size distribution was measured using a Scanning Mobility Particle Analyser (SMPS TSI) which consists of an Electrostatic Classifier (TSI Classifier model 3080, TSI DMA 3081) and a Condensation Particle Counter (TSI Water CPC 3786). In the electrostatic classifier, particles pass through a neutralizer containing Kr-85 source where they are exposed to high concentration of bipolar ions. Through the interactions of aerosol and ions, the particles are ionized reaching Boltzmann equilibrium with a known size dependent number distribution. Particles are then directed to a Differential Mobility Analyzer (DMA) where the electrical field of the DMA together with the electrical mobility of the particles defines the particle size exiting the DMA. These monodisperse particles are then transferred to the CPC where their detection is achieved. By scanning through different DMA electrical fields to measure the total number concentration of monodisperse particles, a particle number distribution is obtained. For this study, an impactor installed in front of the SMPS provided measurements in the 40 to 600 nm range. The time resolution used in this work was 8.5 min. Calculation of the SMPS organic mass concentration was performed, assuming spherical particles with a density of 1.4 g cm^{-3} (Cross et al., 2007) with an estimated measurement accuracy of 12% (Wiedensohler et al., 2012).

Operation of the SMPS was performed by Stefanie Andres, Dr. Tillmann Ralf and Sebastian Schmitt and data analysis was performed by Dr. Tillmann Ralf providing total volume concentration of the particles as a function of time.

3.4 Estimation of volatility distribution

In this work the volatility of different species was quantified based on their saturation mass concentration (C*) in units of μg m^{-3}. Theoretical calculations of the saturation concentration were performed for known oxidation products of the investigated monoterpenes. The predicted values were compared to the observed ones (section 4.8). Considering equilibrium absorptive partitioning the (sub-cooled liquid) saturation vapor pressure ($p_{i,L}$) of a species was related to its C* based on equation 3. Here, the calculations were performed using a

mean molecular weight MW of 180 g mol^{-1} (Hohaus et al., 2015). In conformity with Donahue et al. (2014) the activity coefficients of all considered species partitioning into a mixed aerosol system containing similar compounds were assumed to be 1 throughout the study.

Recently, a new web-based facility, UManSysProp was developed, for automating predictions of i.a. pure component vapor pressures of organic molecules or activity coefficients for mixed liquid systems (http://umansysprop.seaes.manchester.ac.uk). Calculations are performed by uploading the molecular information in form of SMILES (Simplified Molecular Input Line Entry System) strings (Toppings et al., 2016). At a defined temperature, there are several options for vapor pressure predictive techniques, providing the possibility to combine two different empirical representations of the Clausius-Clapeyron equation (Myrdal and Yalkowsky, 1997, Nannoolal et al., 2008) with three different prediction methods for thermodynamic properties of the investigated compounds based on their molecular structure(Joback and Reid, 1987, Nannoolal et al., 2008, Stein and Brown, 1994). Additionally, the EVAPORATION method proposed by (Compernolle et al., 2010) is available for the web-based calculations. Here, we use the $p_{i,L}$ predicted online by UManSysProp facility, to examine all seven estimation methods (Figure A 11. 1). Only the results giving the lowest and highest vapor pressures (grey background color) are considered to be employed in the comparison study. Model calculations for this study have been performed by Dr. Iulia Gensch.

The required thermodynamic properties such as the boiling temperature (T_B) or the enthalpy of vaporization are predicted from the molecular structure of the investigated compounds e.g. (Joback and Reid, 1987, Mackay et al., 1982, Stein and Brown, 1994). Their explicit calculation using functional group contribution methods are very laborious not only because of the high number of components, but also because of the wide range of multifunctional organic compounds in the aerosol mixtures. Parameterizations are derived by comparing experimental boiling points for wide ranges of organics to the estimated values obtained by adding up the contributions multiplied by the number of selected functional groups in the given compounds. Linear regression analyses within the well-defined data base of organic compounds give T_B expressions depending on the molecule structure. The method proposed by Joback and Reid (1987) distinguishes itself by good results despite its simplicity. Even though only 41 molecular functional groups are employed, the method explicitly treats ring increments, which are relevant to monoterpene calculations and thus for this study. Stein and

Brown (1994) introduced more groups in the simulations, describing a total of 85. They introduced multiple subdivisions (e.g. differentiating among OH attached to primary/secondary/tertiary or aromatic C) and conversely, they merged functional groups to larger ones (e.g. amides) for a better fit. Consequently, they refined the T_B function by fitting a second degree polynomial to the extended experimental data for temperatures lower than 700 K. Yet, there should be no significant differences in the T_B calculated using these two methods for organic compounds with less than 10 C atoms (Cordes and Rarey, 2002). Nannoolal et al. (2004) extended further the investigated range of functional groups up to 133, simultaneously introducing information on a greater neighborhood of the central atom of the investigated functional group. In that way, they could simulate higher boiling points for higher branched compounds with a smaller molecular surface, associated with lower vapor pressure values.

The empirical relationships to estimate the vapor pressure are usually polynomial functions of temperature, obtained by integrating the Clausius–Clapeyron equation (equation 2). The coefficients of the various temperature functions are determined by regression analysis of vapor pressure as a function of temperature when making simplifying assumptions on the missing information. The method developed by Myrdal and Yalkowsky (1997) includes heat capacity changes (ΔC_p) for phase transitions into their empirical representation, yielding a lowering in the vapor pressure estimates, compared with the approaches used hitherto. The dependency of ΔC_p upon molecular flexibility, i.e. the number of torsional bonds (nonterminal sp^3 and sp^2, rings), makes this inclusion very interesting for monoterpene calculations. Nannoolal et al. (2008) accounted for the heat capacity changes upon vaporization, but they removed the mathematically more complicated Kirchhoff vapor pressure equation by an Antoine expression. The coefficients were derived from the correlation of vapor pressure data for several hundred components, being directly correlated with the strength of the intermolecular forces in the organic mixture via an 'educated guess' computing. The new feature here is that non-additive interaction contribution of multi-functional groups (e.g OH-ketone) are adopted, resulting in lower vapor pressure values compared with the previous methods. Higher electron delocalization induce stronger dispersive forces, thus decreasing the $p_{i,L}$. Furthermore, the EVAPORATION method proposed by Compernolle et al. (2010) proposed a very simple empirical formula to describe the temperature dependence of the vapor pressure, derived from the Antoine equation. To determine the coefficients, the contributions are additive or not, depending on the

intramolecular interaction between multi-functional groups. This approach doesn't require boiling points. The authors argue that reliable experimental T_B information is difficult to obtain for the targeted SOA compounds. Therefore this direct empirical procedure might strongly simplify the vapor pressure calculations.

Experimental determination of the saturation mass concentration of the individual compounds was derived by applying the partitioning theory (Pankow, 1994) based on Donahue et al. (2006) as in equation 4 where OA is the total organic mass (μg m^{-3}) determined from AMS and G_i and P_i are the gas- and particle-phase mass concentration (μg m^{-3}) of compound i, respectively, measured from the PTR based techniques. Assuming typical vaporization enthalpies presented by Epstein et al. (2010), the C* and therewith the partitioning between the gas- and particle-phase is strongly dependent on the temperature, with changes of ± 15 °C resulting in a change of 1 decade for the C*. Stark et al. (2017) used a reference temperature of 298 K when focusing on the average C* for the BEACHON and SOAS field campaigns with the assumption that deviations due to temperature changes (18 ± 7 °C and 25 ± 3 °C, respectively) were within the uncertainties of the measurements. During this campaign the average chamber temperatures and their standard deviations where 20 ± 4 °C, 17 ± 4 °C, 19 ± 5 °C and 30 ± 5 °C for the β-pinene, limonene, mixture and trees experiment, respectively. The small deviations (< 10 °C) of the average temperatures to the reference temperature of 298 K thus promoted the use of a reference temperature for this study.

Chapter 4 Results and Discussion

The capabilities of the three different PTR-based techniques to measure the overall organic mass concentration as well as the oxygen content of the SOA were compared among each other and to results from an Aerosol Mass Spectrometer (AMS) and a Scanning Mobility Particle Sizer (SMPS) (sections 4.1). Classification of the SOA based on their oxygen and carbon atom number together with their molecular weight was performed (section 4.2) to better understand the differences observed between the PTR-based techniques. The volatility of the bulk OA was further examined by comparing results from the ACM and the TD thermograms (section 4.3). Ions measured from all three techniques were identified and compared to previous publications (section 4.4). In order to identify ions affected by thermal and ionic dissociation a method was developed and tested (section 4.5). The gas-to-particle partitioning of the individual parent ions was determined based on the saturation mass concentration C*, by performing simultaneous measurement of their signal in the gas- and particle-phase (section 4.6). These ions were mapped on the 2D-VBS (section 4.7) and compared to explicit methods (section 4.8).

To achieve the above comparisons, a time synchronization of the three data sets of ACM, TD and CHARON was performed. All data presented in this work have been synchronized to the ACM time with a time resolution of 4 hours. The presented time is the center of the sampling interval for all experiments.

Sections 4.1 to 4.4 presented in the following chapter have been reported in Gkatzelis et al. (2017) and are discussed in more detail here while the figures and tables used from Gkatzelis et al. (2017) are identified throughout this work.

4.1 Determination of mass recovery and oxygen content of organic aerosol

Comparison of the overall mass concentration the different aerosol chemical characterization techniques measured, to the AMS and SMPS was performed (Figure 15). Linear regression was applied to fit the data for each instrument and experiment. Total mass concentration signal for the PTR-based techniques was derived by adding the signal of all individual contributing ions (more details in Chapter 3). Since no collection efficiency (CE) was applied

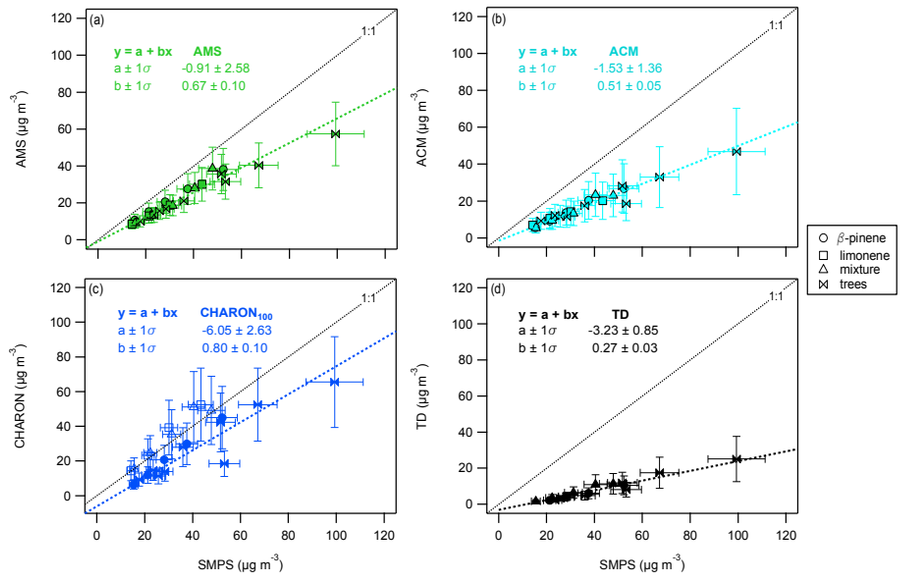

Figure 15: Comparison of the organic mass concentration of (a) AMS (green), (b) ACM (ciel), (c) $CHARON_{100}$ (blue) and (d) TD (black), to the SMPS (x-axis). Markers correspond to the different experiments with the mixture experiment accounting for the mixture of β-pinene and limonene. AMS data presented are not corrected for collection efficiency. $CHARON_{100}$ corresponds to data taken only at 100 Td E/N operating condition. Error bars provide the uncertainty of each instrument (details in Section 3.3). A least orthogonal distance regression linear fit is applied for every instrument, taking into account all campaign measurement points. Exception is the CHARON limonene and mixture data (open markers) that were excluded due to experimental flaws. Details of the coefficient values and their standard deviation (± 1σ) are given on the upper left of each graph. This graph is adopted from Gkatzelis et al. (2017).

to the PTR-based aerosol measurement techniques, AMS data were treated the same way throughout this work, thus no AMS CE was enforced. A least orthogonal distance regression linear fit function, included in the IGOR extension ODRPack95, was used for each instrument related to SMPS data. Results showed that the measured fraction compared to the SMPS mass was constant for each technique throughout the campaign. Due to malfunctions $CHARON_{100}$ introduced a higher than usual variability of the particle enrichment in the aerodynamic lens during two experiments, the β-pinene/limonene mixture ozonolysis and the limonene ozonolysis/NO_3 oxidation (Section 3.3.3). These experiments were excluded when applying the linear fit. $CHARON_{100}$ was able to measure 80% (1σ = ± 10%) of the SMPS mass. ACM and AMS measured 51% (± 5%) and 67% (± 10%) while TD measured 27% (±

3%) of the SMPS, respectively. TD and ACM showed the lowest slope uncertainties (≤ 5%), thus the highest stability in terms of recovery or overall detection efficiency. $CHARON_{100}$ and AMS followed with slope accuracy of ~ 10%, but at higher recovery rates. All instruments showed linear fit offset values close to zero when taking into account the error of the fit (± 3σ).

For the PTR based techniques and AMS an underestimation of the measured SOA mass concentration could be expected due to a variety of processes from (i) CE losses during particle collection, (ii) thermal dissociation during desorption, (iii) ionic dissociation in the ionization region, and (iv) the inability of the PTRMS to ionize the reactant/fragment. The extent to which these processes affect the different techniques was investigated in detail in this work (sections 4.1, 4.2, 4.5). An estimation of their individual importance is discussed. Since these processes occur in parallel, no quantitative results are presented for accessing CE, thermal dissociation, ionic fragmentation and ionization efficiency in this work.

It is well known that AMS derived mass concentrations have to be corrected for CE due to particle bounce signal loss on the vaporizer (Canagaratna et al., 2007). Fresh biogenic SOA though have a high CE (Kiendler-Scharr et al., 2009) and reduced bouncing effect, also observed from the relatively high AMS CE in this work (~ 0.7). ACM and TD utilize a collection surface as well and therefore introduce a CE uncertainty with the TD setup reducing the bouncing effects by humidifying the particles prior to collection. CHARON is an on-line technique avoiding loss processes associated with collection, thus increasing the ability of the instrument to measure the mass concentration of the compounds generated during these experiments.

During desorption, thermal dissociation of molecules could introduce two or more fragmentation products. Canagaratna et al. (2015) reported that in the AMS organics give rise to H_2O^+, CO^+ and CO_2^+ signal due to surface dissociation and thermal break down of organic molecules at vaporizer operating temperatures down to 200 °C (under vacuum conditions). Although neutral dissociation products like H_2O, CO and CO_2 could be ionized by the AMS, their proton affinities are lower than that of H_2O, thus PTR techniques cannot ionize and detect them. On the contrary, remaining smaller organic fragmentation products with proton affinities higher than H_2O would still be visible to the PTR-MS. A lack of detection of certain neutral fragments formed during thermal desorption could introduce an underestimation of the total mass, and the oxygen and carbon concentration for the PTR based techniques. It should be noted that decarboxylation and dehydration reactions are strongly dependent on the temperature, pressure and the heat exposure time of the molecules.

CHARON was operated at the lowest temperature of 140 °C, under a few mbars of pressure and with the lowest heat exposure time thus minimizing the latter reactions. On the contrary, ACM and TD were operated at 1 bar and up to 250 °C and 350 °C respectively with longer heat exposure times. To further assess whether thermal dissociation for ACM and TD had an additional effect on the measurements, the experimental findings from the case studies performed by Salvador et al. (2016) using the TD-PTR-ToF-MS were examined. Five authentic standard substances (phthalic acid, levoglucosan, arabitol, cis-pinonic and glutaric acid) were utilized to examine the response of the sampling device. If the compounds would only fragment in the PTR-ToF-MS due to ionic dissociation, then the detected fragments should have the same volatility trend as the parent compounds since both originate from the latter. During desorption of the collected samples, fragment ions were found to represent different volatility trends compared to their parent ions (Arabitol, cis-Pinonic Acid). These thermogram differences, originating from the same substance, promoted certain amount of neutral fragmentation/pyrolysis in the hot TD cell.

Ionic dissociation in the ionization region of the PTR-MS is strongly affected by the PTR operating conditions and in particular the E/N applied in the drift tube region (Section 3.3). The lower mass concentration detected by the TD unit compared to ACM and CHARON could be partly explained by the different E/N used, with TD operated at the highest E/N = 160 Td. This high potential of fragmentation losses during quantification would be given as:

$$(R^+)^* \rightarrow F^+ + N \quad (8)$$

where $(R^+)^*$ is the unstable protonated reactant, F^+ is the protonated fragment and N is the neutral product. By increasing the fragmentation potential the neutral products would increase, thus lowering the total mass concentration detected. This could also lead to an underestimation of the ACM mass concentration compared to $CHARON_{100}$ (ACM operated at 120 Td and $CHARON_{100}$ at 100 Td) and is discussed in detail in the next section. It should be noted that the mass underestimation of the ACM due to ionic and thermal dissociation could be higher than the mass difference between the ACM and AMS. This would imply that ACM CE was higher compared to the AMS CE during this campaign, a possible result due to the differences of vaporizer/collector geometry (Hohaus et al., 2010). ACM does not use flash vaporization but after collection the heating of the wide collector surface is initiated thus avoiding losses due to bouncing of the particles like AMS.

Additional comparison between the AMS and the PTR-ToF-MS based techniques was examined by determining the bulk oxygen to carbon ratio (O:C) for all instruments (

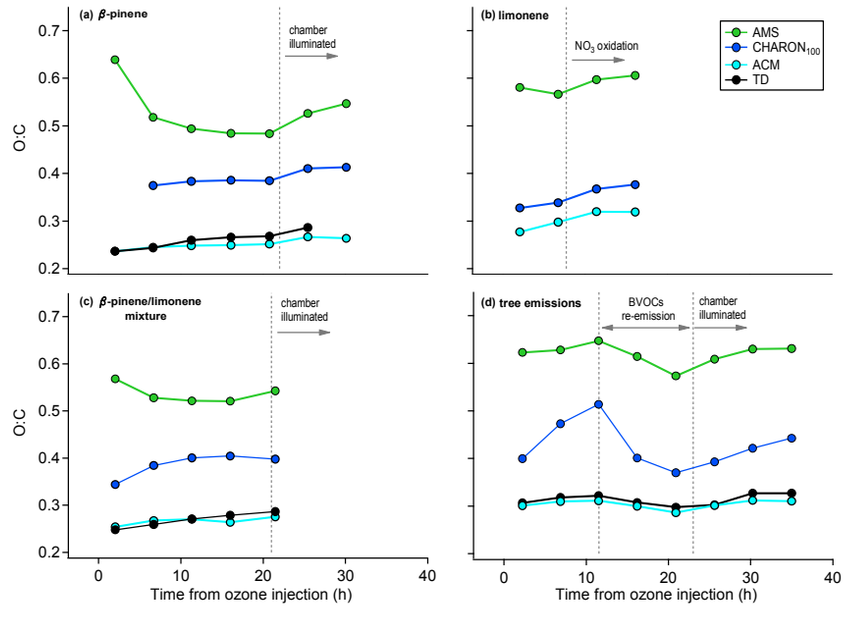

Figure 16: Bulk oxygen to carbon ratio comparison for the different instruments ($CHARON_{100}$: blue, AMS: green, ACM: ciel, TD: black) versus the time from ozone injection. Experimental description details are provided in Table 1. This graph is adopted from Gkatzelis et al. (2017).

Figure 16). AMS O:C values were calculated based on the method by Canagaratna et al. (2015). For the PTR-based techniques O:C calculation was performed based on the O:C ratio of the individual ions (based on their chemical formula) in combination with their contribution to the total OA mass (for details see section 3.3.1). All instruments followed similar trends. O:C ratios increased with photochemistry initiation (chamber illumination) or NO_3 oxidation (limonene experiment/NO injection). On the contrary, O:C values decreased when fresh BVOC was introduced into SAPHIR and additional SOA was formed during the tree BVOCs re-emission stage (11 – 22 h after ozone injection). ACM and TD O:C ratios ranged from 0.24 to 0.32, and CHARON from 0.32 to 0.50, while AMS ranged from 0.5 to 0.65. When compared to AMS, all PTR-ToF-MS based techniques showed lower O:C values. Good agreement was found between the ACM and TD O:C values (< 3% difference). $CHARON_{100}$ measured higher O:C compared to ACM and TD (ACM lower by ~ 20-35%), an indication that during this campaign $CHARON_{100}$ was capable of detecting more oxygenated compounds. When comparing the β-pinene and limonene experiments,

$CHARON_{100}$ had increased O:C values for experiments that incorporated β-pinene while ACM had the opposite behavior, with higher O:C during the limonene experiment. For the mixture experiment the O:C of the ACM was between the O:C values obtained from the individual precursor experiments while CHARON did not follow the same trend with the O:C of the mixture showing the highest values from the three experiments (Figure A 3. 1). For the tree emissions experiment the BVOC system resulted in SOA that showed increased O:C values for all instruments introducing compounds with higher oxygen content in the particulate-phase. During this experiment CHARON was operated at different E/N operating conditions thus providing further insights of the influence of E/N on O:C values (Figure A 4. 1). Results showed that O:C increased by approximately 10% when changing the CHARON E/N from 100 Td to 65 Td, thus providing softer ionization conditions.

Although nearly all $C_xH_yO_z$ ions can be identified and quantified within the AMS mass spectra, AMS O:C calculation based on Canagaratna et al. (2015) has several sources of uncertainties due to correction factors applied. As stated by Canagaratna et al. (2015), the overall errors observed in elemental ratios calculations would introduce an upper uncertainty of 28%. In contrast to AMS data O:C ratios for the PTR based techniques were calculated with no additional correction factors thus explaining their lower values when compared to AMS.

PTR-ToF-MS is considered a soft ionization technique which suffers less from fragmentation and therefore should provide O:C ratios closer to the true values compared to uncorrected AMS data. Nevertheless, water clustering and carbon-oxygen bond breakage could occur, either increasing or decreasing O:C ratios. When proton transfer reactions induce fragmentation a neutral fragment is lost. For oxygenated organics it has been shown that the loss of water as neutral fragment is a common fragmentation pathway (de Gouw and Warneke, 2007). This could explain the lower O:C values seen from CHARON, ACM and TD compared to the AMS. Inter-comparison of the PTR based techniques further showed that $CHARON_{100}$ was more sensitive to oxygenated compounds compared to ACM and TD. Higher O:C ratios were observed when comparing $CHARON_{65}$ to $CHARON_{100}$ indicating that low E/N values can decrease the loss of neutral fragments such as water or carbon containing compounds with O:C ratios >1 (e.g. CO_2, HCOOH). This factor does affect the ACM and TD O:C ratios even more, since they were operated at even higher E/N (120 Td and 160 Td, respectively) than CHARON. It should be noted that lower E/N values could also increase the tendency to detect water clusters, i.e. $AH^+(H_2O)_n$, where A is the ionized

organic compound, bearing the risk to bias the O:C ratio high which is explored further in the next section.

As previously discussed, AMS H_2O, CO and CO_2 (detected as ionized H_2O^+, CO^+ and CO_2^+ signals) are generated due to thermal dissociation at temperatures exceeding 200 °C, under vacuum conditions. These fragment signals cannot be detected from ACM and TD, that undergo higher thermal dissociation compared to CHARON, thus an additional underestimation of their O:C values could not be excluded. To assess the extent of thermal dissociation, further re-calculation of the AMS O:C, excluding the H_2O^+, CO^+ and CO_2^+ peaks was performed and compared to the PTR-based techniques for the tree emissions as seen in Figure A 5. 1 (a). By excluding the H_2O^+ signal for the O:C analysis of the AMS, the initial O:C ratio of 0.6 ± 0.02 was reduced by approximately 30% while when excluding H_2O^+, CO^+ and CO_2^+ signals the reduction increased to 60%. These AMS O:C values were lower by 40% than that of ACM and TD for the tree emissions. When only excluding the H_2O^+ signal, AMS O:C ratios were higher by 30% compared to ACM and TD. These results suggest that CO and CO_2 loss by thermal dissociation in the ACM and TD play a less significant role compared to AMS due to their lower operating evaporation temperatures and higher pressure but still have an effect.

When comparing experiments incorporating β-pinene or limonene, the different behavior of the O:C ratios found for the $CHARON_{100}$ ($O{:}C_{\text{ CHARON, limonene}} < O{:}C_{\text{ CHARON, β-pinene}}$) and ACM ($O{:}C_{\text{ ACM, limonene}} > O{:}C_{\text{ ACM, β-pinene}}$) could be due to different fragmentation patterns of the particulate-phase functional groups or due to their volatility differences. Since limonene SOA are less volatile than β-pinene SOA (Lee et al., 2011) a fraction of the OA oxygenated mass that would evaporate at higher temperatures could be lost for CHARON that was operated at lower temperatures, thus leading to lower O:C values compared to the β-pinene experiments. Although one could expect a higher loss in CHARON due to the lower operating temperature compared to ACM, its reduced pressure compensates for the temperature difference thus increasing the volatility range down to low volatility OA (Eichler et al., 2017). Furthermore, ACM showed only minor differences in the thermograms obtained from the β-pinene compared to the limonene experiments, as seen in Figure A 6. 1. These results suggest that differences in the O:C trends of ACM and CHARON could not be fully explained by changes of the SOA volatility. The ionic and thermal dissociation patterns of the different particulate-phase functional groups could play a role in these findings and has to be examined in future studies.

4.2 Classification of SOA composition

Further comparison of the aerosol chemical characterization techniques was performed with a focus on the different chemical characteristics (oxygen atom number, carbon atom number, molecular weight) of the SOA composition. A desorption period from the tree emissions

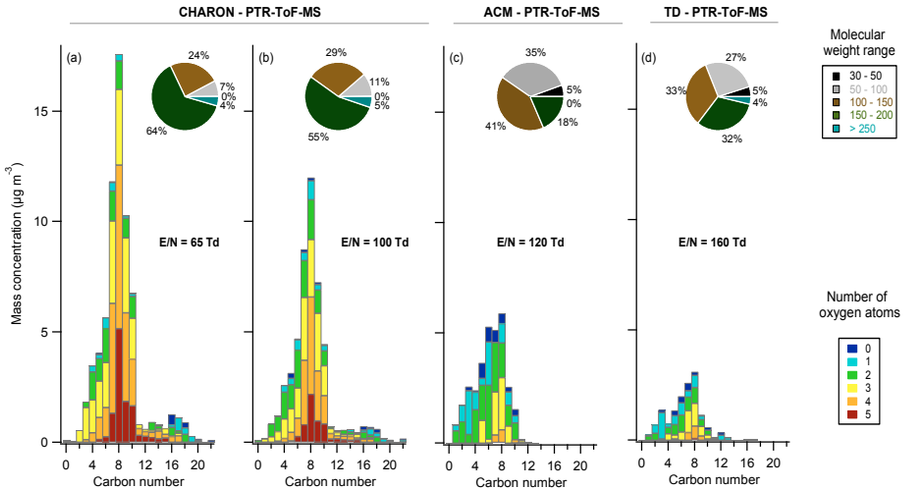

Figure 17: OA mass concentration (y-axis) distributed based on the number of carbon atoms (x-axis). Bar colours correspond to the contribution of oxygen atoms starting from 0 (blue) to 5 (red) for each carbon group when (a) CHARON was operated at E/N = 65 Td, (b) CHARON operated at 100 Td, (c) ACM operated at 120 Td and (d) TD operated at 160 Td. Pie charts correspond to the molecular weight contribution to the overall mass starting from *m/z* 30 – 50 (black) up to *m/z* > 250 (ciel). Results shown in this graph are from the tree emissions experiment at a high OA mass concentration, 25 h after the ozone injection (Figure 16 (d)). This graph is adopted from Gkatzelis et al. (2017).

experiment, 25 hours after the ozone injection (Figure 16 (d)), was chosen in order to highlight the instrument performance differences, shown in Figure 17. This example introduced the highest differences due to the complexity of the precursor mixture thus providing clear insights for the comparison of the PTR-based techniques. The mass concentration of all compounds containing the same carbon number was calculated. These carbon fractions were then further separated depending on the number of oxygen atoms the compounds contained. The molecular weights (MW) of the SOA constituents was separated in five different *m/z* range groups, from *m/z* 30 - 50, *m/z* 50 - 100, *m/z* 100 - 150, *m/z* 150 - 250, *m/z* >250. For ACM detection ranged from C1 to C13 and O0 to O4 atom numbers. The

carbon distribution showed the highest mass concentration for C8 species. Increased contribution of lower oxygen atom number species was observed at lower carbon atom numbers (< C7). Species with lower MW were observed to have a high contribution for ACM with 40% and 80% of the overall mass concentration coming from compounds below 100 and 150 u, respectively, while 20% of the mass was observed at higher MW (> 150 u). When comparing ACM to CHARON and TD, all instruments showed similar carbon content distributions, with the highest concentration introduced from C8 compounds. CHARON was able to measure compounds in the C10 - C20 range while ACM and TD only detected up to C13 compounds. The overall OA mass concentration decreased when moving from lower ($CHARON_{65}$ and $CHARON_{100}$) to higher E/N values (ACM at 120 Td and TD at 160 Td). The same trend was seen for the oxygen content of compounds; with a characteristic example being the compounds containing 5 oxygen atoms that decreased by a factor of 2 with the same instrument but different operational parameters for the PTR-ToF-MS ($CHARON_{65}$ vs. $CHARON_{100}$). In ACM and TD compounds containing 5 oxygens were negligible. A similar trend was observed for *m/z* range distributions, with a higher fraction of low *m/z* compounds observed at increasing E/N values. ACM and TD results indicated that the main fraction of compounds was detected for MW < 100 amu (70 and 75% of the overall mass concentration, respectively).

These results clearly show that the overall mass concentration detection as well as the carbon, oxygen and MW content determination are strongly affected by the PTR-ToF-MS E/N operating conditions. As the E/N values increased, oxygen-carbon bond breakage increased leading to undetected neutral fragments. This loss of information directly affects the overall mass concentration and MW detection range. Comparing the ACM to the TD MW pie charts showed that, although ACM was operated at lower E/N conditions (120 Td) than the TD (160 Td) the contribution in the lower MW range was higher for the ACM. The reason for this dissimilarity could be due to the higher limit of detection of the PTR-ToF-MS used for the ACM (see Table 2) leading to lower detection of the higher molecular weight compounds. Since water loss is the major fragmentation occurring in the PTR-ToF-MS, the oxygen content is affected the strongest from the increasing E/N. This could explain why compounds with 5 oxygens were nearly undetectable for ACM and TD compared to CHARON.

To further assess the differences in chemical classification by each instrument the relative OA mass concentration of molecular weight, carbon and oxygen number (box-and-whiskers including all data points throughout the campaign) were used, as seen in Figure 18. ACM and TD showed similar distributions for all contributions throughout the campaign with only

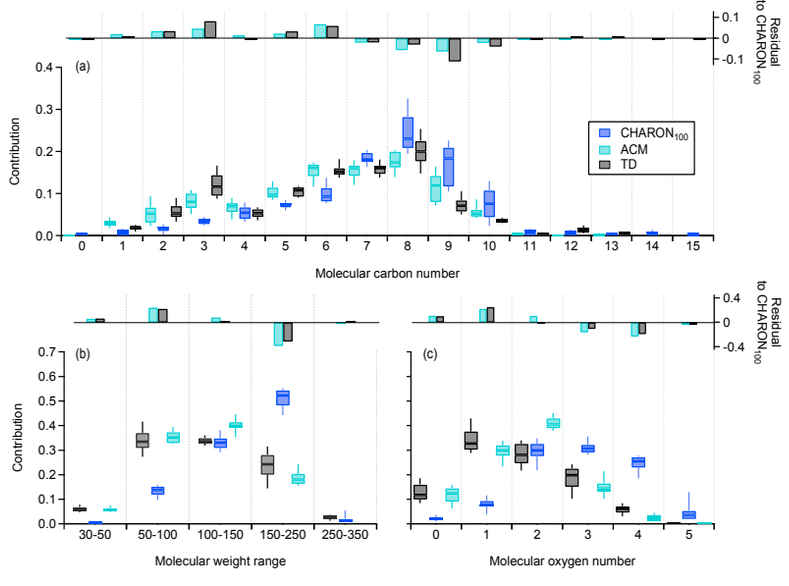

Figure 18: Box-and-whisker plots showing the relative OA mass concentration distribution dependent on (a) molecular carbon number, (b) molecular weight and (c) molecular oxygen number for the different instruments, indicated with different colours ($CHARON_{100}$ blue, ACM ciel and TD black). Each box-and-whisker corresponds to the median, 25th and 75th percentile levels of all data throughout the campaign. Upper graphs indicate the difference between the ACM and TD to the $CHARON_{100}$ median values defined as residual to $CHARON_{100}$. This graph is adopted from Gkatzelis et al. (2017).

minor differences (< 3%). On the contrary, their comparison to $CHARON_{100}$ showed a clear difference. Compounds in the lower MW range (< *m/z* 150), containing lower molecular carbon (< 9 carbon atoms) and oxygen (< 2 oxygen atoms) showed higher contributions for the ACM and TD compared to $CHARON_{100}$. A detailed comparison of CHARON's different E/N conditions during the tree emissions experiment (Figure A 7. 1) was also performed. Results indicated that for lower E/N, an absolute difference of 2%, 5% and 10% for the molecular carbon, weight and oxygen contributions were observed, respectively, suggesting that in this E/N range (from 65 to 100 Td) fragmentation is dominated by loss of oxygen due to fragmentation of functional groups.

The above results strongly suggest that the E/N settings play a key role in determining the fragmentation patterns. By increasing the drift tube voltage, the velocity of the ions increased, leading to higher kinetic energy in ion molecule and therefore stronger buffer gas collision. This energy increase was translated to an increase in carbon-oxygen bond breakage. On the

contrary, the lower the E/N was set, the higher the sensitivity due to enhanced reaction times but also the stronger the cluster ion distribution change, supporting more $H_3O^+(H_2O)_n$ (n=1,2,3) cluster ion generation (de Gouw and Warneke, 2007). In order to quantify whether the PTR-ToF-MS E/N conditions were a major factor for the differences seen during this campaign, a case study of pinonic acid was performed in the lab by Dr. Markus Müller.

Monodisperse pinonic acid particles were generated (900 – 1100 particles/cm^3) and directed to a CHARON-PTR-ToF-MS, changing E/N values from 60 to 170 Td (Figure A 8. 1). Results showed that the relative intensity of the parent ion decreased rapidly when increasing the E/N values. At the same time, the relative intensity of the lightweight fragments was increasing. The effect of the parent ion clustering with water was negligible suggesting no overestimation of the CHARON oxygen content at low E/N (65 Td). By assuming a uniform sensitivity and calculating the total signal (parent ion and fragments, assuming all *m/z* represent parent molecules) the mass fraction of pinonic acid particles was calculated (Figure A 8. 2). The higher the E/N values were set, the less the PTR-ToF-MS measured compared to the SMPS. These results confirmed our previous findings that fragmentation losses lead to an underestimation of the overall mass concentration. Therefore the different E/N conditions of the detection systems (PTR-ToF-MS) could explain to a large degree the differences between the CHARON, ACM and TD oxygen and carbon content (results seen in Figure 16 and Figure 18) as well as their differences in the overall detectable mass (results seen in Figure 15 and Figure 17). A clear influence of the aerosol sampling technique on the differences of these parameters cannot be determined nor excluded (Salvador et al., 2016).

4.3 Volatility comparison based on the temperature profiles

During the campaign, CHARON was operated at a constant temperature (140 °C) while ACM and TD ramped through different temperatures during desorption of the collected aerosol samples (see section 3.3). The ramping of ACM and TD provided the possibility of a detailed comparison of the compound dependent volatility trends. The ratio of the mass evaporating at each temperature step to the total mass concentration measured from ACM and TD, respectively, was calculated. An overview of the ACM results is provided in Figure 19. Similar evaporation trends were observed for all experiments. Around 10 to 30% of the ACM OA evaporated at the collector temperature of 100 °C, 20% at 150 °C, while the highest mass contribution was observed at 250 °C (50 to 60%). High contributions of the

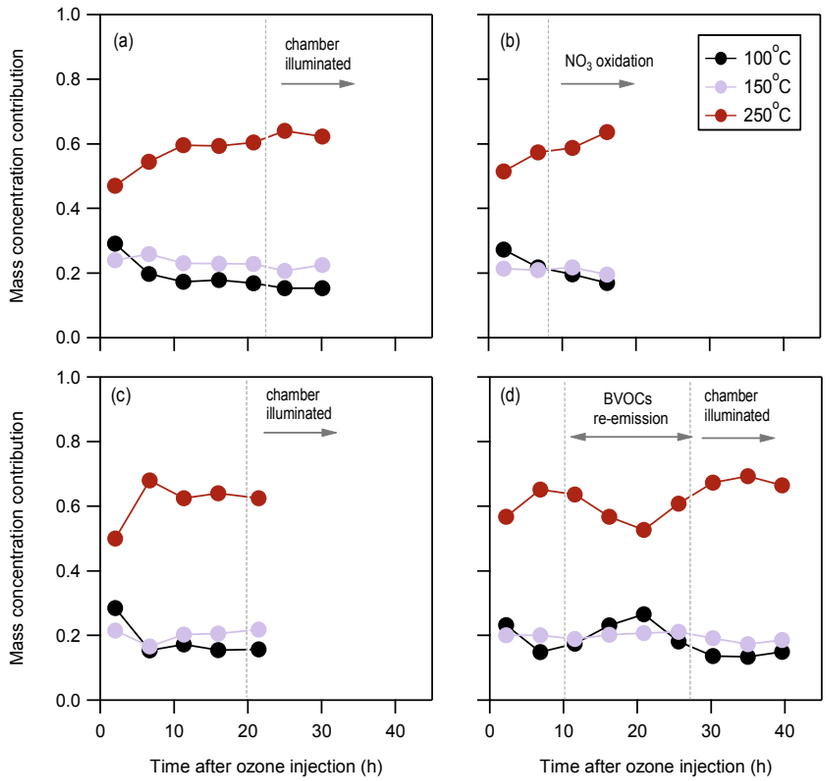

Figure 19: Overview of the ACM mass concentration contribution at each temperature of the thermogram for the (a) β-pinene, (b) limonene, (c) mixture and (d) tree emissions oxidations experiments. Different colours correspond to the different temperature of the heated collector.

aerosol mass concentration evaporated at lower temperatures when fresh SOA were generated (initial hours of the experiments and tree emissions re-emission stage) hence higher SOA volatility values were observed. As oxidation continued the relative contributions of aerosol mass evaporating at low temperatures and therefore the overall volatility decreased. When illuminating the chamber, SOA volatility decreased suggesting that photochemical aging of the SOA took place leading to a change of the chemical composition and volatility distribution.

Further comparison of ACM to TD was performed (Figure 20) with the limonene ozonolysis and NO_3 oxidation excluded from this comparison, due to TD operational problems. Both

instruments showed similar trends as previously discussed for ACM. For experiments having β-pinene as a precursor, TD showed a continuous decrease in volatility as the experiment evolved while ACM reached a plateau after 5 to 10 hours of aging. The volatility changes for both instruments, during the initial hours of the experiments and during the re-introduction of BVOCs for the trees experiment, could be attributed to the high concentration of semi-volatile organic compounds (SVOCs) in the gas-phase that had the maximum available surface to condense on (SMPS at its maximum surface are and mass concentration). Under

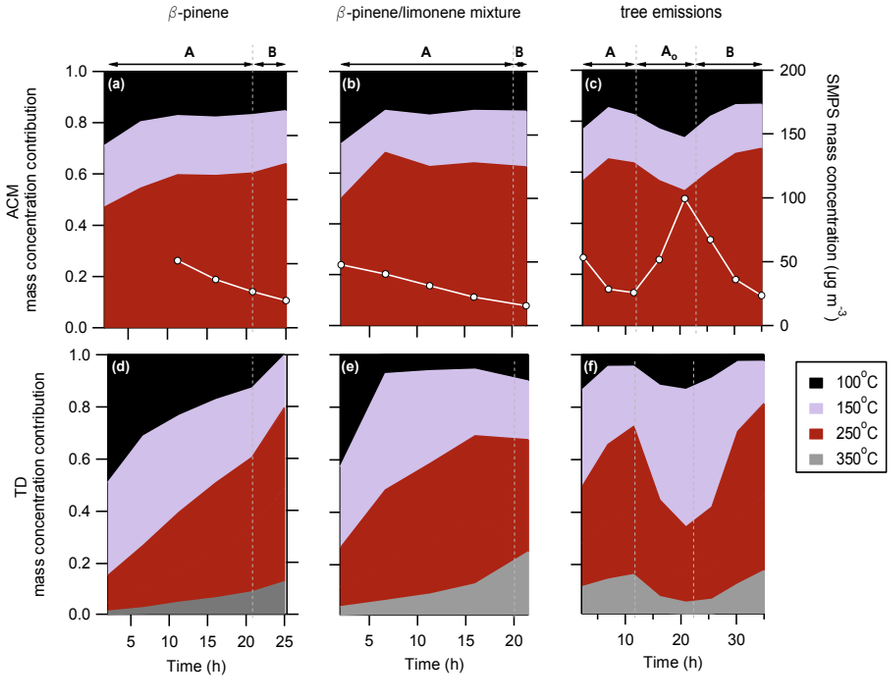

Figure 20: Temperature dependent mass concentration contribution (left y-axis) of ACM (upper plots: a, b, c) and TD (lower plots: d, e, f) for β-pinene (a, d), β-pinene and limonene mixture (b, e) and real tree emissions (c, f) versus the time since ozone injection (x-axis). White lines and circle markers (right y-axis) represent the SMPS mass concentration during each experiment. Dash vertical lines indicate the different experimental periods with A: the ozonolysis and SOA formation period, B: the chamber illumination and photo-oxidation period and A_0: the tree emissions BVOCs re-injection to the SAPHIR chamber. This graph is adopted from Gkatzelis et al. (2017).

these conditions, these compounds would partition more to the particulate-phase thus increasing their contribution during the highest concentration periods. These SVOCs that more easily evaporate back to the gas-phase could change the volatility patterns with higher mass contribution at lower collector temperatures, as observed from both techniques by a change of the thermograms during the maximum concentration periods.

Discrepancies between the ACM and TD, with the latter having a steadily changing desorption temperature with time, could be explained by several operating differences. During evaporation ACM was ramped by 100 °C min^{-1} to a maximum of 250 °C, with 3-minute isothermal sections at 100 °C, 150 °C and 250 °C, respectively, while TD was ramped continuously at a rate of ~15 °C min^{-1} for ~21 minutes until 350 °C. The higher volatility resolution of TD compared to ACM could introduce an increased sensitivity to volatility changes thus increase the TD variability compared to ACM. Differences could also be partly attributed to the different design of the instruments. ACM ensured complete separation of the particulate from the gas-phase (> 99.9999 gas-phase removal) while TD was corrected for gas-phase contamination by performing background measurements (Section 3.3.4). During collection of the particulate-phase compounds in the TD, the collector was exposed to high concentration of SVOCs from the gas-phase, thus increasing the risk for gas-phase oversampling. As the gas-phase concentrations decreased the TD volatility decreased. This could thus indicate a possible background correction artifact mostly affecting compounds in the higher volatility range, evaporating in the first temperature steps (100 ºC).

To further assess the volatility differences of ACM and TD, focus was given on the molecular oxygen number based on the assumption that oxygen number correlates to volatility (Jimenez et al., 2009). Box-and-whiskers, including all campaign desorption periods, were generated for each molecular oxygen number at each temperature, as seen in Figure 21. The data were normalized to the sum of the measured mass concentration from each molecular oxygen number in all temperatures following the above equation:

$$n_{\text{oxygen atoms i,100°C}} + n_{\text{oxygen atoms i,150°C}} + n_{\text{oxygen atoms i,250°C}} = 1\,, \qquad (9)$$

where $n_{\text{oxygen atoms i}}$ corresponds to the mass concentration contribution of all species containing i number of oxygen atoms at the different evaporation temperatures. Results showed that TD had a broader range in fractional contribution for all oxygen bins when compared to the ACM. A characteristic temperature showing this difference is 150 °C, where

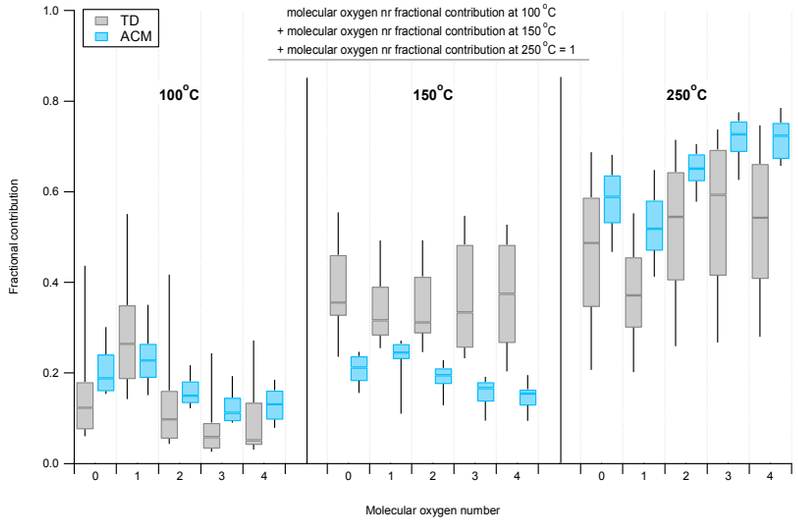

Figure 21: Box-and-whisker plots showing the distribution of the molecular oxygen number (x-axis), for the different temperature steps (100 °C, 150 ºC, 250 °C) of ACM (ciel) and TD (black). Each box-and-whisker corresponds to the median, 25th and 75th percentile levels of all desorption points throughout the campaign. Upper equation indicates how the contribution of each molecular oxygen number, at each temperature, corresponds to unity. This graph is adopted from Gkatzelis et al. (2017).

TD showed results in the range of 0.2 to 0.55 while ACM was in the range from 0.15 to 0.25. Despite the differences in relative contribution, both instruments showed similar trends. As the temperature of the collector increased, oxygenated compounds (2, 3 and 4 oxygens) contributed more than lower oxygenates. On the contrary, at lower temperatures compounds containing 0 and 1 oxygen were the dominant factor. Overall, for ACM around 20% of the SOA evaporated at 100 °C, 20% at 150 °C and 60% at 250 °C. TD showed similar volatility trends with 15 to 20% of the SOA evaporating at 100 °C, 35% at 150 °C and 50 to 55% at 250 °C.

According to observations and theory (Jimenez et al., 2009) oxygenated compounds are expected to have lower volatility thus evaporating at higher temperatures. TD and ACM described the expected volatility trends during the performed experiments based on compound specific information in accordance to theory. The variability of TD compared to ACM reflected the differences in the design and operation of the individual systems described previously. The higher volatility resolution but also the higher E/N conditions of TD could explain most of the observed discrepancies. Fragmentation due to ionic dissociation

after the evaporation could influence the volatility molecular oxygen content distribution by loss of neutral oxygen containing fragments. This could further affect the volatility distribution when the oxidation product concentrations change with time, reflected by the increase of the O:C ratios (see Figure 16). Furthermore, the ability of ACM to achieve complete gas to particle separation resulted in a lower thermogram uncertainty in the higher volatility range thus smaller variations. These results show the applicability of both techniques to study BSOA volatility trends in a compound specific level.

4.4 Compound detection comparison and tracers attribution

The molecular formula ($C_xH_yO_zN_a$) was attributed to each detected signal derived from the exact molecular mass (see section 3.3) determined by the TOF-MS for all 3 techniques throughout the campaign. In order to assess whether major contributing molecules with the same chemical formula were determined by all instruments, a comparison of the dominant signals was performed i.e. the molecular formulas that (i) were measured by all techniques during each experiment and (ii) were within the 80 highest signal concentrations. Figure 22 shows the respective results from the BSOA detected in the C7 to C10 range with varying oxygen content (from 0 to 4 oxygens). Although these techniques could provide the molecular formula of the compounds, the molecular structures are unknown. In order to derive further information, comparison to previous publications was performed for the major oxidation products from (a) the β-pinene ozonolysis (Hohaus et al., 2015, Yu et al., 1999, Chen and Griffin, 2005, Jenkin, 2004), (b) limonene ozonolysis and NO_3 oxidation (Jaoui et al., 2006, Kundu et al., 2012, Leungsakul et al., 2005b, Leungsakul et al., 2005a, Chen and Griffin, 2005) and (c) tree emissions ozonolysis with α-pinene and Δ^3-carene being the major reactants (Praplan et al., 2014, Yu et al., 1999, Chen and Griffin, 2005). Results showed that all techniques were able to detect most of the expected molecules. Details on the molecular formula and suggested structure are provided in more detail in Table A 2. Due to fragmentation most of the compounds were not detected at the parent ion molecular weight but underwent water loss in accordance to the findings that O:C ratios are observed to be reduced by ACM, TD and CHARON compared to the AMS (see section 4.1). These compounds corresponded to a large fraction of the BSOA mass measured from each technique (bars in Figure 22). On average, 70%, 60%, and 40% of the measured mass was contributed from these compounds, for ACM, CHARON and TD, respectively. When

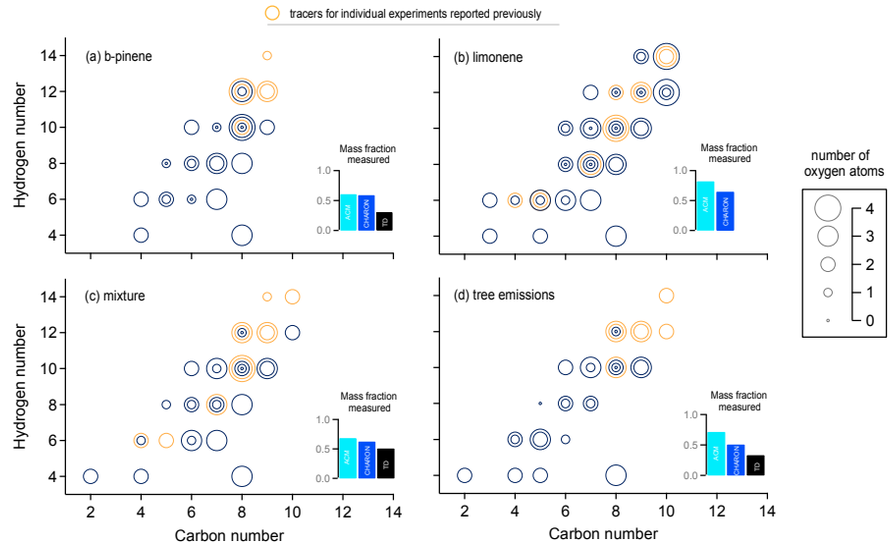

Figure 22: Chemical formula attribution based on the molecular carbon number (x-axis), hydrogen number (y-axis) and oxygen number (markers size) for the different experiments. Markers correspond to compounds measured from all techniques (ACM, CHARON and TD) at high concentrations (within the 80 compounds observing highest concentration). Each marker corresponds to one compound. For a given carbon and hydrogen atom number there can be different oxygen atom contained in the species, defined by the size of the marker e.g., multiple circles for C_8H_{10} species express the existence of $C_8H_{10}O_1$, $C_9H_8O_2$ etc. Orange markers indicate tracer compounds supported from previous publications (for details refer to Table A 2). Bars indicate the fraction of mass explained when accounting only the presented compounds, for each instrument (ACM ciel, $CHARON_{100}$ blue and TD black) based on their total aerosol mass measured. This graph is adopted from Gkatzelis et al. (2017).

comparing the above compounds concentration to the SMPS total mass, around 30%, 50% and 10% of the SMPS mass for ACM, CHARON and TD respectively was explained. The overlapping of detected compounds to compounds observed from previous publications (theoretical and experimental work) and their high contribution (up to 50%) to the overall BSOA mass concentration strongly promotes the use of PTR-ToF-MS aerosol measurement techniques to gain valuable insight on the chemical characteristics of BSOA.

4.5 Partitioning compound selection method: Assessment of ionic and thermal decomposition

Whether a detected ion was an original SOA compound or a fragment detected on this mass could be affected by two major processes, (i) thermal dissociation during desorption, and (ii) ionic dissociation in the ionization region of the PTR-ToF-MS.

Thermal dissociation has been found to introduce a high degree of fragmentation for compounds that contain multiple functional groups, including peroxide groups which are thermally labile (Lopez-Hilfiker et al., 2015). For organic alcohols and acids thermal desorption has been shown to lead to loss of carboxyl (-CO_2), carbonyl (-CO) and water (-H_2O) (Canagaratna et al., 2015). Accretion reactions and gas-phase autoxidation have been found to play a key role in ELVOC (section 1.4.2) formation (Tobias and Ziemann, 2001, Tobias and Ziemann, 1999, Ehn et al., 2014). Upon heating, such products will thermally decompose (Barsanti et al., 2017) and be detected in the lower molecular weight range thus directly affecting the partitioning estimation (Stark et al., 2017, Jang and Kamens, 2001) based on equation 4. All instruments deployed in this study were subjected to possible thermal dissociation with decarboxylation and dehydration reactions strongly dependent on the temperature, pressure and the heat exposure time of the molecules during desorption. CHARON was operated at the lowest temperature of 140 °C, under a few mbars of pressure and with the lowest heat exposure time therefore minimizing the latter reactions. On the contrary, ACM and TD were operated at 1 bar and up to 250 °C and 350 °C respectively with longer heat exposure times.

Functional group loss has been found to additionally occur in the ionization region of the PTR-ToF-MS instruments. E/N conditions in the PTR-ToF-MS instruments played a key role in decomposition, not only due to water loss but also carbon-oxygen bond breakage of the detected molecules (section 4.2). Even though PTRMS is considered a soft ionization technique compared to e.g. AMS, these decomposition pathways could still lead to misidentification of the original chemical composition of the SOA species. For the ACM the ionic fragmentation for the gas- and particle-phase species was identical since both measurements were conducted using the same PTR-ToF-MS as a detector. This would mean that in equation 4, G_i and P_i would be affected in the same way by ionic dissociation thus not affecting the saturation mass concentration (C*) calculation. CHARON and TD C* was determined by using the gas-phase (G_i) mass concentration measurements derived from a separately deployed PTR-ToF-MS operated at different E/N conditions (see Section 3.3).

Ionic dissociation was thus different for the gas- compared to the particle-phase measurements increasing the uncertainty of the volatility estimation for CHARON and TD when compared to ACM. Hereon the average C* for each ion detected both in the gas- and particle-phase was calculated for each experiment and instrument together with the error of the average. These values are further used to derive conclusions on the ability of the PTR-based instruments to provide reliable saturation concentration values.

A method to identify the ionic and thermal dissociation processes and their effect to the different techniques is presented in the following. This method was applied to the calculated average $\log_{10}(C^*)$ of each ion, found both in the gas- and particle-phase, for each experiment for the individual instruments as presented in the following equation:

$$\log_{10}(C_i^*)_{\text{experiment average}} = \frac{\sum_{z=0}^{n} \log_{10}(OA_z \times G_{i,z}/P_{i,z})}{n}, \quad (10)$$

where i is an indicator of the ion used, n is the number of points for each experiment based on the time resolution of ACM, OA_z stands for the total OA mass concentration at each point z of the experiment measured from the SMPS in μg m^{-3} (assuming a particle density of 1.4 g mol^{-1}), and Gi,z and Pi,z stand for the gas- and particle-phase mass concentration of the individual ions at each point z of the experiment in μg m^{-3}, respectively. A characteristic example of the β-pinene ozonolysis experiment (as shown in Figure 23) for the ACM is used here to explain this method. Information of the carbon (x-axis) and oxygen (size of the markers) atom number contained in the chemical formulas were used to differentiate between the different ions (Figure 23a). Each marker indicates one ion, therefore for the β-pinene experiment and for ACM 72 ions were detected both in the gas- and particle-phase. Their average saturation concentration $\log_{10}(C^*)$ and therefore their volatility ranged from 1 to 4, an indication of semi-volatile and intermediate-volatility species in the SOA mass. From these ions 55 were identified as fragmentation products accounting for 70 % of the partitioning ions and only 25 % of these ions were used for further analysis. Two major criteria were applied to differentiate between a possible parent ion (green markers) and a fragment: (i) if the carbon and oxygen atom number were lower than a certain threshold the ions were excluded from further analysis (grey markers). Based on Donahue et al. (2006) organic aerosols are expected in the range from ELVOC to SVOC and IVOC with saturation concentrations ranging from -5 to 4. This volatility regime consists of species with carbon and oxygen atom numbers higher than 5 and 1 respectively (Donahue et al., 2012, Donahue et al., 2011). Ions found in the particle-phase with lower carbon and oxygen numbers were thus

considered fragmentation products (grey markers) and were not considered further in the analysis. (ii) If the volatility of an identified ion $[M+H]^+$

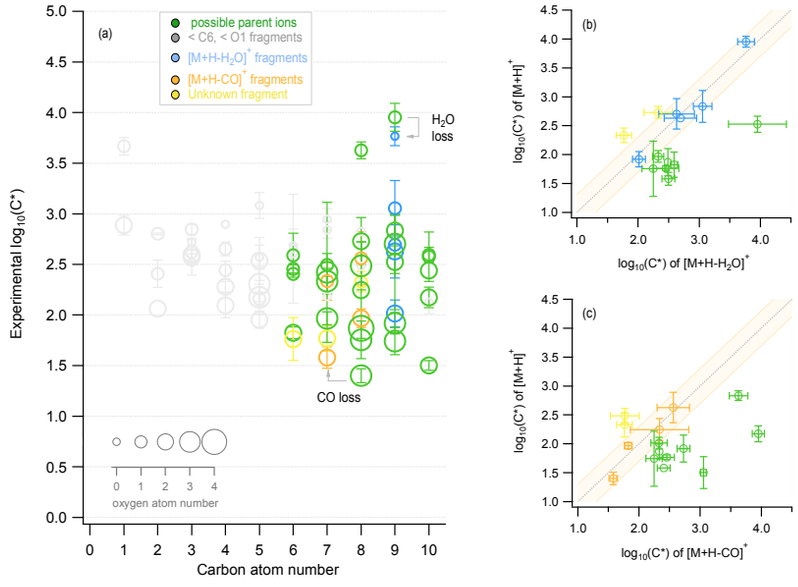

Figure 23: Characteristic example of fragment identification method from the β-pinene ozonolysis experiment for the ACM where (a) is the experimental saturation concentration (y-axis) for all identified compounds with different carbon (x-axis) and oxygen atom number (size of markers). Different colors indicate whether the compound represents a possible parent ion (green), a fragment with carbon and oxygen atom number lower than 6 and 1 respectively (grey), or a fragment originating from the loss of water (blue) or CO (orange). Figure (b) and (c) show the correlation of the saturation concentration of identified $[M+H]^+$ ions to compounds with the same chemical formula subtracting water $[M+H-H_2O]^+$ or CO $[M+H-CO]^+$. If the correlation is close to the 1:1 line then the $[M+H-H_2O]^+$ or $[M+H-CO]^+$compound is identified as a fragment and is given the respective color (blue or orange). The orange background indicates the ± 0.25 change of $\log_{10}(C^*)$. Error bars correspond to the error of the average (± 1σ).

was identical to (within $\log_{10}(C^*)$ of ± 0.25) or higher than the volatility of ions with the same chemical formula subtracting a functional group $[M+H-FG]^+$, the latter were considered highly affected by either ionic or thermal dissociation and were excluded from further analysis.

Characteristic examples showing this comparison are shown in Figure 23b and c. The y-axis corresponded to identified ions $[M+H]^+$ while the x-axis to ions with the same chemical formula subtracting water ($-H_2O$)(Figure 23b) or a carbonyl group (-CO)(Figure 23c). Since

volatility is dependent on the oxygen and carbon atom number (Pankow and Barsanti, 2009) decreasing O or C number in a molecule would directly affect their saturation concentration. When ions $[M+H]^+$ and $[M+H-FG]^+$ were found to have identical saturation concentrations, $[M+H-FG]^+$ ions were excluded (blue and orange markers in Figure 23b and c). $[M+H-FG]^+$ ions that showed lower volatility when compared to $[M+H]^+$ ions where considered fragments of unknown decomposition pathways (i.e. unknown parent ion composition) and were excluded as well (yellow markers). Only when ions $[M+H-FG]^+$ showed higher volatility values they were considered possible parent ions not strongly affected by thermal or ionic dissociation (green markers) and were further analyzed. The same comparison was not only performed for ($-H_2O$) and (-CO) functional group loss but was extended to ($-CO_2$), ($-H_2O_2$), ($-H_2O$) plus (-CO), and ($-H_2O$) plus ($-CO_2$).

An overview of the fragmentation identification results of this method for each instrument and experiment is provided in Figure A 9. 1. Percentages are derived based on the total number of fragment ions and how they distribute (%) to the different fragmentation pathways. For all PTR based techniques 40 to 60% of the partitioning ions were detected below the carbon and oxygen atom number threshold of C5 and O1, respectively. From the remaining species, ions affected by water ($-H_2O$) loss were around 5-10%, while carboxyl group ($-CO_2$) fragmentation was identified for less than 10% of the partitioning ions. Loss of (-CO), ($-H_2O_2$), ($-H_2O$) plus (-CO) and ($-H_2O$) plus ($-CO_2$) functional groups affected less than 5% of the ions for all experiments and instruments studied. Ions of unknown decomposition pathways represented $\leq$ 10% with TD showing the highest values. ACM showed increased contributions of lower molecular weight ions, compared to TD and CHARON, for limonene and mixture experiments (max 65%). In total, the fraction of ions identified as parent compounds partitioning in the gas- and particle-phase that were chosen for further analysis in the next sections ranged between 20-40% of the overall partitioning ions for each experiment and instrument studied.

The high contribution of lower MW partitioning ions for all PTR based techniques further promoted that ionic and thermal decomposition played a key role in carbon-oxygen bond breakage. The higher E/N values of ACM and TD compared to CHARON resulted in higher fragmentation thus higher contribution of the lower MW partitioning ions (section 4.2). Although ACM was operated al lower E/N conditions compared to TD, the contribution of lower MW ions was higher. The reason for this discrepancy was due to the higher limit of detection of the ACM (see Table 2) compared to TD and CHARON. Ions of low concentration in the higher MW range that could be detected from CHARON and TD were

below the detection limits of the ACM and were therefore not identified. For the remaining higher MW species, the water ($-H_2O$) loss was the dominant fragmentation pathway for all techniques. Although the PTR-based techniques were operated at different temperature, desorption residence times and pressure conditions they showed similar percent of ions affected by water loss. This is an indication that for all techniques dehydration occurred mostly due to ionic fragmentation in the ionization region of the PTRMS and not due to thermally initiated reactions for the partitioning ions studied. TD showed higher contribution of fragments of unknown decomposition pathways when compared to ACM and CHARON due to the highest difference of E/N operating conditions in the particle-phase (160 Td) compared to the gas-phase (130 Td), with the latter measured by a separately deployed PTR-ToF-MS. The higher ionic dissociation in the particle-phase increased the concentration of lower MW ions and decreased that of higher MW species. This had a direct effect on the calculation of the volatility based on equation 4. When this effect was strong enough fragment ions $[M+H-FG]^+$ showed higher concentrations in the particle phase thus lower volatility when compared to possible parent ions $[M+H]^+$. These ions were, based on this method, excluded as fragments of unknown fragmentation pathways and showed an expected higher contribution for systems like the TD. Fragment loss of ($-CO_2$), ($-CO$), ($-H_2O_2$), ($-H_2O$) plus ($-CO$) and ($-H_2O$) plus ($-CO_2$) accounted for 10% or less suggesting that these pathways were not dominating the partitioning ions studied. It should be noted that the decomposition of accretion reaction products or oligomers could be considered as a parent ion when using the above mentioned method, consequently leading to an overestimation of their particulate phase concentrations. This effect is not constrained by this parent ion selection method and is further addressed in Section 4.8.

4.6 Volatility distribution coverage: Instrument capabilities

The mass concentration of only the species accounted as parent ions for ACM, CHARON and TD was distributed to different volatility bins ranging from -1 to 5 with a 0.5 volatility resolution. The normalized volatility distribution (NVD) for each experiment accounting for all PTR-based techniques is shown in Figure 24. Normalization was performed by dividing each volatility bin by the sum of the PTR-based techniques mass concentration measured at each experiment. The detected biogenic SOA partitioning species showed $\log_{10}(C^*)$ values from 0 to 4, an indication of SVOCs and IVOCs. The limonene NO_3 oxidation experiment

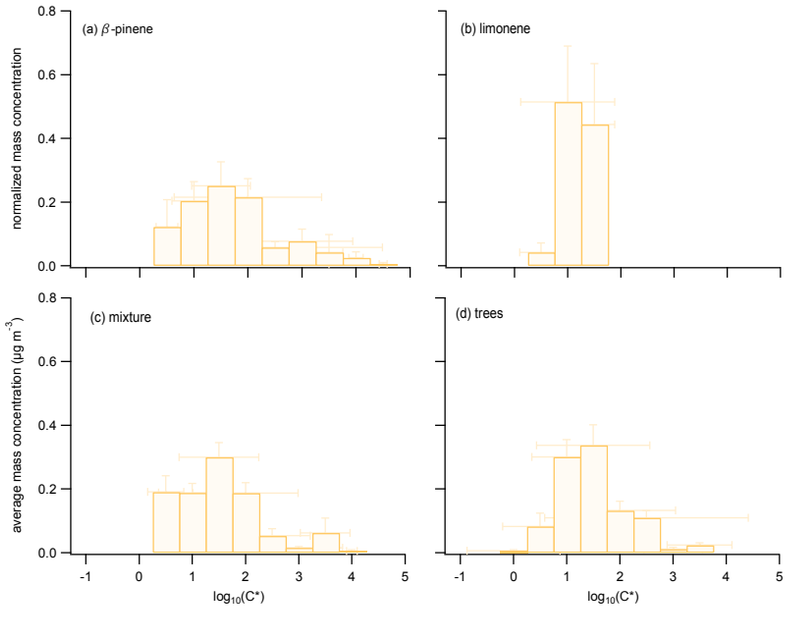

Figure 24: The normalized average mass concentration from ACM, CHARON and TD, distributed to the different volatility bins with a volatility resolution of 0.5. Error bars correspond to the ± 1σ of the average throughout each experiment. Each figure corresponds to an individual experiment.

had the lowest NVD starting from a $\log_{10}$(C*) of 0.5, with a narrow spread up to 2. For the β-pinene and β-pinene/limonene mixture experiments the NVD moved towards more volatile species ranging from 0.5 to 4. When comparing the single compound experiment of β-pinene to the mixture, the latter showed a NVD shifted to lower saturation concentrations, in accordance with the lower $\log_{10}$(C*) observed for pure limonene SOA. Partitioning species detected from all the PTR-based techniques were further compared as seen in Figure 25. ACM and CHARON showed same volatility values for all experiments with only the trees experiment resulting in higher deviations from the one to one line. TD presented higher $\log_{10}$(C*) when compared to CHARON and ACM, suggesting the examined species were underestimated in the particle-phase. A total of 5, 2, 6 and 4 ions were observed to partition with all three techniques for the β-pinene, limonene, β-pinene/limonene mixture and tree emissions experiment, respectively.

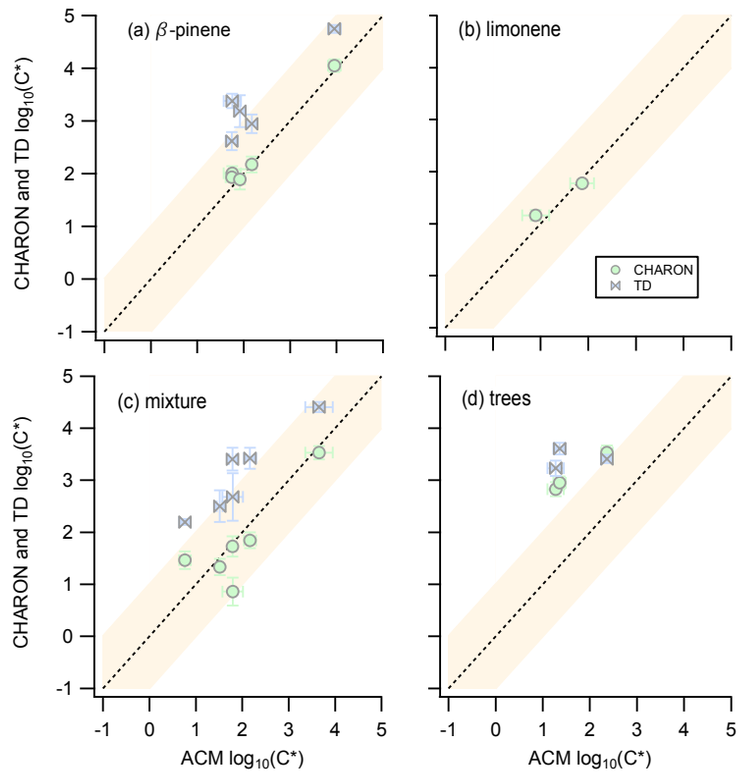

Figure 25: The average volatility of overlapping compounds seen from CHARON and ACM (circles) or TD and ACM (double triangles) in the different experiments. The dash line represents the 1:1 line. The orange background color indicates the ± 1 deviation from the 1:1. Error bars correspond to the ± 1σ of the average throughout each experiment.

Calculation of the $\log_{10}$(C*) in this study relied on the ratio between the gas- and particle-phase signal of an ion (equation 4). Detection limits of both of these limited the measurable range of this ratio. This explains the narrow volatility distributions available with all PTR-based techniques, as has been previously reported by Stark et al. (2017). Combining the capabilities of these instruments and the above approach to calculate the volatility provided insights in a defined range of SVOCs and IVOCs. Within this volatility range the differences observed when using different precursors agrees with bulk volatility measurement findings that limonene SOA are less volatile than β-pinene SOA (Lee et al., 2011). Differences on the

species measured for ACM and CHARON to TD could be explained by the higher E/N conditions of TD that were previously discussed (section 4.2). Since TD was more prone to particle-phase fragmentation compared to the gas-phase these higher MW compounds showed lower concentrations thus indicated higher volatility. This effect was negligible for ACM that was using the same PTRMS for gas- and particle-phase measurements and lower for CHARON operated at lower E/N conditions. The agreement of ACM and CHARON for all experiments except the trees experiment further promoted that both techniques measured the same species in good agreement and within the uncertainties of these calculations. As the complexity of the system increased, this agreement deviated from the one to one line. For the single precursor and mixture experiments ions were detected with C6 to C12 carbon atoms from all techniques. However, during the tree emissions experiment CHARON was the only instrument to detect ions in the C13 to C20 range (Section 4.2). These ions were not detected from ACM or TD that were operated at higher E/N conditions and were more likely to thermally decompose. Dissociation of these higher carbon atom ions could affect the volatility calculation of lower MW species still detected by ACM and TD and thus explain the deviations seen for the tree emissions experiment.

The total number of species seen from all techniques was low due to the partitioning compound selection method applied in the section 4.5. An overview of the overlapping compounds is provided in Figure A 9. 2. When all detected ions were taken into account more than 50 ions were seen from all techniques at each experiment. After narrowing our focus on the partitioning ions and excluding the lower MW fragments the overlapping compounds dropped to ~ 15 ions. Each technique was affected differently by ionic and thermal dissociation. By applying the above method to each technique different ions were excluded for each instrument thus leading to only a few species seen from all three techniques and accounted as parent ions.

4.7 Experimentally derived saturation concentration implemented to the 2D-VBS

Species identified as parent ions for all techniques were combined and further analysed with a focus on their average saturation concentration as seen in Figure 26. The 2D-VBS (Murphy et al., 2012, Donahue et al., 2011) was used to implement the results for each experiment with background colours corresponding to the different volatility classes, ranging from IVOCs

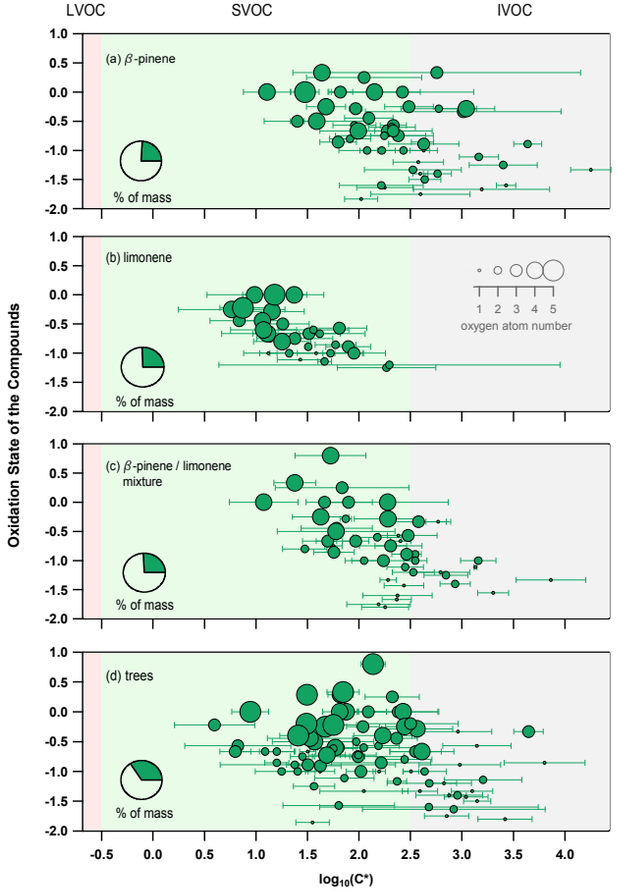

Figure 26: The average experimental saturation concentration for detected ions (from ACM, CHARON or TD) that act as parent ions identified using the described selection criteria during the (a) β-pinene, (b) limonene, (c) mixture of β-pinene and limonene and (d) the real tree emissions experiments. Error bars indicate the ± 1σ of the average. Size of the markers is an indicator of the oxygen atom number for each species. Pie charts show the percent of mass (green) measured when adding all presented ions compared to the total organic mass obtained from the AMS.

(grey) to SVOCs (green) and LVOCs (red). It should be noted here that the oxidation state (OS_C) was not corresponding to the bulk oxidation state ($\overline{OS}_C$) measured e.g. by AMS, but the OS_C of the individual species based on their carbon, hydrogen and oxygen atom number. In total 48, 31, 46 and 79 ions were identified as parent ions for the β-pinene, limonene, β-pinene and limonene mixture and tree emissions oxidation experiment, respectively.

Saturation concentration showed a decrease for species with higher OS_C and oxygen atom number. For the limonene experiment lower saturation concentration values for compounds defined by the same oxidation state was found when compared to the β-pinene, mixture or tree emissions experiment. Overall, parent ions corresponded to 20-30 % of the overall organic mass measured from an SMPS for all systems studied.

The observed volatility decrease with increasing OS and oxygen atom number is in good agreement with previous findings (Kroll, 2011, Jimenez et al., 2009). Limonene lower volatility values for species with the same OS when compared to the β-pinene, mixture or tree emissions experiment suggested that species originating from different precursors and oxidation pathways could introduce differences in their functionality and molecular structure thus affect their gas-to-particle partitioning. It should be noted that the lower volatility of limonene could be partly explained by the absence of TD data in this experiment and thus the absence of TD C* values when averaging the results from all PTR-based techniques. Since TD was affected the strongest by ionic dissociation, the C* values were biased to higher volatilities when compared to ACM and CHARON with particle-phase measurements (P_i in equation 4) fragmenting more compared to the gas-phase (G_i from dedicated gas-phase PTR operated at lower E/N). Results for all experiments excluding the TD data are shown in Figure A 10. 1. The limonene experiment would still show lower volatilities compared to the β-pinene and mixture experiments. However, a shift towards lower volatilities without accounting TD data in the average calculations is observed. Nevertheless, differences when accounting or excluding TD from this analysis does not change the trends and conclusions drawn from Figure 26. The increased number of species detected during the tree emissions experiment occurred due to the higher complexity of this system with more than one precursor oxidized to form SOA. In total, the PTR-based techniques showed that 20-30 % of the overall BSOA mass consisted of compounds with volatilities within the SVOC to IVOC range further promoting the importance of understanding the gas-to-particle partitioning and thermodynamic properties of compounds formed in such systems.

4.8 Experimentally derived saturation concentration compared to explicit methods

In order to derive further information from the experimentally determined parent ions, comparison to previous publications was performed for the major oxidation products from (a) the β-pinene ozonolysis (Hohaus et al., 2015, Yu et al., 1999, Chen and Griffin, 2005, Jenkin,

2004, Kahnt, 2012, Steitz, 2010), (b) limonene ozonolysis and NO_3 oxidation (Jaoui et al., 2006, Kundu et al., 2012, Leungsakul et al., 2005b, Leungsakul et al., 2005a, Chen and Griffin, 2005) and (c) tree emissions ozonolysis with α-pinene and Δ^3-carene being the major reactants (Praplan et al., 2014, Yu et al., 1999, Chen and Griffin, 2005). Species detected as parent ions that overlapped with compounds observed from previous publications were further examined based on their structural information. An overview of the overlapping compounds and their suggested structures are given in Table A 2.

A detailed analysis of the β-pinene ozonolysis experiment was performed with a focus on a 1st generation oxidation product, nopinone. Nopinone has been previously experimentally

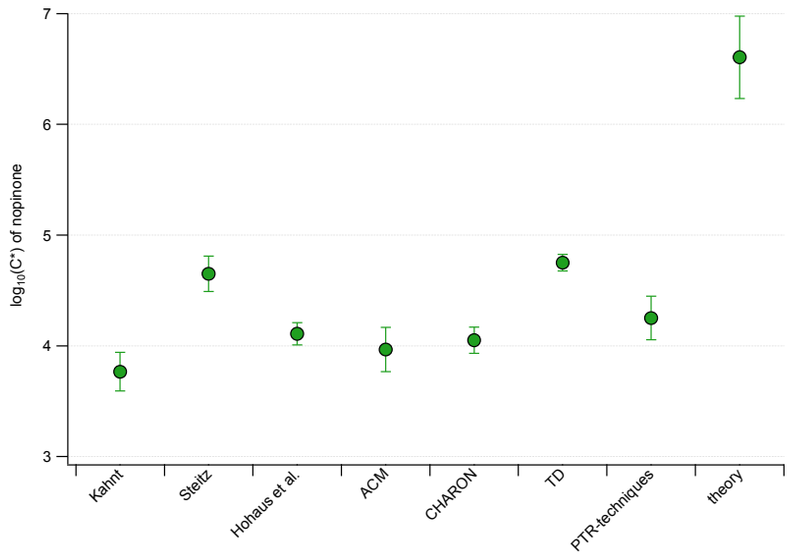

Figure 27: Comparison of the experimentally determined values of the saturation concentration for nopinone based on Hohaus et al. (2015), Kahnt (2012) and (Steitz, 2010) together with the results of the experimental (ACM, CHARON and TD), their average indicated as PTR-techniques and the theoretical approaches from this study. Theoretical calculations were performed by assuming the chemical structure of nopinone. Error bars on the experimental approaches indicate the ± 1σ error of the average while the error bars for the theoretical calculation act as indicators of the minimum and maximum range of 7 different theoretical approaches with the position of the marker indicating the average of these minimum and maximum values. More details on the theoretical calculations are provided in section 3.4.

studied with a focus on the gas-to-particle partitioning (Hohaus et al., 2015, Kahnt, 2012, Steitz, 2010). Comparison of this work to previous studies and to theory was performed as seen in Figure 27. Experimental calculation of the saturation concentration was performed based on the average C* values throughout the experiment for each technique (ACM, CHARON, TD) with the error bars indicating the ± 1σ of this averaging together with the average from all techniques indicated as PTR-techniques. For the theoretical calculations two methods were chosen, that showed the maximum and minimum values respectively when compared to other theoretical approaches (Figure A 11. 1). These limits are expressed by the error bars on the y-axis with the marker points corresponding to their average. For more details on the theoretical calculation the reader is referred to section 3.4. Results showed agreement within $\log_{10}(C^*)$ values of $\pm 10^{0.5}$ for the experimental approaches while the theoretical calculations were higher by 3 orders of magnitude on the C* estimation. The PTR-based calculated C* was in good agreement with previous studies using a GC-MS to detect particle-phase nopinone (Hohaus et al., 2015, Kahnt, 2012). Since GC-MS techniques are capable of providing the exact molecular structure of nopinone this further supported the identification of $(C_9H_{14}O_1)H^+$ as protonated nopinone in this study.

This comparison was extended to more oxidation products as seen in Figure 28. This time the experimental C* was calculated only based on the average of all PTR-based techniques with the error bars indicating the ± 1σ of this averaging. In total 10 compounds were identified from previous publications to overlap with experimentally detected parent ions for the β-pinene ozonolysis experiment. For most of these compounds theoretical and experimental values agreed well, when taking into account their errors. Better agreement was found for compounds in the SVOC volatility range while the saturation mass concentration of compounds in the IVOC were underestimated (nopinone and oxonopinone) from the experimental approaches when compared to theory. Comparison to the findings of Hohaus et al. (2015) further supported that not only nopinone but also oxonopinone, was found to be in excellent agreement when compared to the experimental approaches used in this work (3.16 ± 0.13 and 3.16 ± 0.12 respectively).

To better understand the differences of the experimental to the theoretical approaches, focus was given on the uncertainties of both calculations. For the theoretical approach as the molecules added more functional groups and more complexity, the uncertainty increased for both the saturation vapor pressure and the volatility. This is depicted by the higher error bars

when moving towards SVOCs. First generation products like nopinone are not characterized by high complexity, thus theory provided more reliable thermodynamic values also proven by

Figure 28: The experimental average saturation concentration obtained from all PTR-based techniques (y-axis) compared to the theoretical calculation of the saturation concentration (x-axis). Theoretical calculations were performed by assuming a chemical structure for the experimentally observed ions. The chemical structure was attributed based on known oxidation products of the β-pinene ozonolysis experiment and are shown on the right side of the figure. Error bars on the y-axis indicate the ± 1σ error of the average based on the experimental results from ACM, TD and CHARON. The error bars for the x-axis act as indicators of the minimum and maximum range of 7 different theoretical approaches with the position of the marker indicating the average of these minimum and maximum values. More details on the theoretical calculations are provided in section 3.4.

the good agreement between all theoretical approaches (Figure A 11. 1). The experimental calculation of the volatility performed by the PTR-based techniques could still be affected by the (i) existence of isomers within a studied *m/z* with different structural information and thus thermodynamic properties, (ii) thermal and ionic fragmentation of higher molecular weight compounds, produced by accretion and oligomerization reactions, in the *m/z* range detected by the PTRMS, (iii) phase-state of the bulk OA affecting the partitioning equilibrium time-scales (τ_{eq}) of the individual compounds.

Mass spectrometric measurement approaches provide by definition molecular formulas; however a given formula does not correspond to an individual compound. Isaacman-VanWertz et al. (2017) showed that during the α-pinene OH oxidation molecules with larger carbon atom numbers (C8 to C10) corresponded to an increased number of unique isomers for each molecular formula. Differences in the functionality of these isomers may be critical for studies of their thermodynamic properties. To reduce biases in this work, the different isomers seen from previous publications were included in the theoretical calculations. For the β-pinene experiment isomers showed C* values within the estimated uncertainty thus not strongly affecting the average C* calculation and therefore biasing low this comparison.

Treatment of this dataset to exclude ions affected by thermal and ionic dissociation was performed and analyzed in section 4.5. However, higher MW species e.g. accretion reaction products or oligomers, of low volatility, not in the detection range of the PTR-ToF-MS instruments could decompose to lower MW species during thermal breakdown (Barsanti et al., 2017). These species could be identified as a parent ion when using the parent ion identification method and consequently lead to an overestimation of their particulate-phase concentrations. This effect is not constrained to this method and could potentially and selectively decrease the volatility of certain species. To explain the experimental to theoretical differences found for nopinone, the ratio $\frac{G_i}{P_i}$ from equation 4 should change by a factor of ~ 300. This would suggest a particulate-phase mass concentration 300 times lower in order to reach an agreement with the theoretical calculations. This fragmentation pathway should not only strongly affect the PTR-based techniques but also the previously mentioned GC-MS systems thus narrowing the decomposition pathway to thermal dissociation during desorption, the only common pathway from all techniques. Finally, this thermal decomposition pathway would result in products with the exact chemical structure of nopinone.

When describing SOA formation, it is generally assumed that oxidation products rapidly adopt gas-to-particle equilibrium with the assumption of a homogeneously mixed condensed phase (Pankow, 1994, Odum et al., 1996). The non-ideal behavior of a complex organic mixture could introduce matrix effects, changing the activity coefficients of the individual organic molecules and thus their gas-to-particle equilibrium. Isotopic labeling experiments have confirmed that SOA derived from different precursors will interact in a relatively ideal fashion thus introducing low activity coefficient deviations from unity (Hildebrandt et al., 2011, Dommen et al., 2009). Furthermore, Hohaus et al. (2015) showed that for the β-pinene

ozonolysis oxidation products the theoretically estimated activity coefficient values based on the thermodynamic group-contribution model AIOFAC (Zuend et al., 2011) were far from explaining the theoretical to experimental differences. These findings further promoted that in this work gas-to-particle partitioning was not strongly affected by activity coefficient deviations and thus could not explain the observed differences.

On the contrary, the phase-state of the bulk OA strongly affects the partitioning equilibrium time-scales (τ_{eq}) ranging from seconds in case of liquid particles to hours or days for semi-solid or glassy particles (Shiraiwa and Seinfeld, 2012). Biogenic SOA particles have been found to adopt an amorphous solid-, most probably glassy-state (Virtanen et al., 2010). This amorphous solid-state may influence the partitioning of semi-volatile compounds. Biogenic OA produced in this study would be directly affected not only by high partitioning equilibrium time-scales but also increased particulate-phase concentrations of more volatile compounds "trapped" within this glassy-state of the OA. This would imply a direct reduction of their volatility thus explaining the observed lower C* values of the 1st generation products.

A comparison of observed and calculated C* was performed for all experiments during this campaign as seen in Figure 29. Compounds measured experimentally and seen from previous publications were 11, 12 and 9 for the limonene, mixture and trees oxidation experiments, respectively. These compounds were detected in 5, 8 and 4 different *m/z* suggesting an increased number of isomers found within these overlaps. Results showed similar trends as for the β-pinene experiment with theory in relatively good agreement with experiments for most of the compounds in the SVOC range while compounds expected in the IVOC range were experimentally underestimated, i.e. a larger particle-phase concentration was observed than explained by equilibrium partitioning theory. When moving from single to multiple precursor experiments and as the complexity of the studied systems increased, from e.g. the ozonolysis of β-pinene to the ozonolysis and NO_3 oxidation of limonene and the tree emissions, the number of isomers increased rapidly. Certain isomers showed high variations in their theoretical volatility values with changes within 2 orders of magnitude. These findings further promoted that for complex systems the limitations of mass spectrometric techniques to define the molecular structure of the compounds could introduce biases. For the tree emissions experiment compounds in the SVOC range had lower volatility when compared to theory, an indication that for biogenic complex systems the phase-state of the OA could play a key role, changing the equilibration timescales and thus the gas-to-particle partitioning. Despite these uncertainties, most of the theoretical to experimental volatility

values were still found to be in good agreement, suggesting that these deviations would be within the already existing high uncertainties of these calculations.

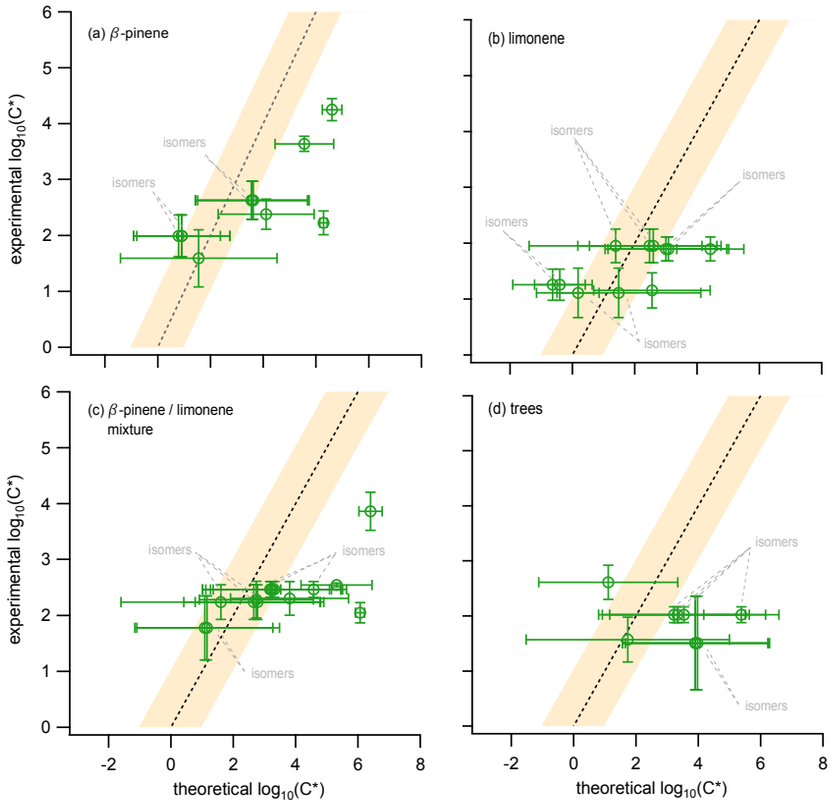

Figure 29: The experimental average saturation concentration obtained from all PTR-based techniques (y-axis) compared to the theoretical calculation of the saturation concentration (x-axis) for the (i) β-pinene, (ii) limonene, (iii) mixture of β-pinene and limonene and (iv) the real tree emissions experiments. Error bars on the y-axis indicate the ± 1σ error of the average based on the experimental results from ACM, TD and CHARON. The error bars for the x-axis act as indicators of the minimum and maximum range of 7 different theoretical approaches with the position of the marker indicating the average of these minimum and maximum values.

There are two major effects that could be summarized by presenting two case scenarios. In the first scenario the equilibrium partitioning theory would correctly represent the studied systems. The experimental underestimation of the IVOCs (and certain SVOCs) volatility would thus only be explained by experimental limitations due to either fragmentation of

higher MW compounds and oligomers to the detection range of the PTR-based techniques or the existence of isomers with high volatility differences. In the second scenario the assumption of equilibrium partitioning would be questioned due to the findings that BSOA form a glassy phase-state and thus gas-to-particle equilibrium is not reached. This would imply that the assumption of an equilibrium partitioning is not valid in all cases and depends on the precursor and the extent the SOA was aged. This result suggests that non-equilibrium aspects should be included in future theoretical calculations to further improve their predictions and close the gap between measurements and theoretical estimations. This work provides clear evidence pointing towards these two effects but cannot distinguish how large the contributions of each effect are. Future studies to measure the phase-state of the SOA in parallel to the information provided by the PTR-based techniques is essential. In order to bridge the gap between experimental and theoretical volatility calculations further development of instrumentation providing structural information in a molecular level is required. Techniques like the TAG (Zhang et al., 2014, Isaacman et al., 2014, Williams et al., 2006) coupled in parallel to the PTR-based techniques could provide further insight to different isomeric structures.

Chapter 5 Summary and Outlook

Secondary organic aerosol (SOA), formed by chemical reactions in the atmosphere, constitute a major fraction of the organic aerosol (OA) and thus play a key role in climate change and air quality. Defining the fundamental parameters that distribute organic molecules between the gas and particle phases is essential, as atmospheric lifetime and impacts change drastically when changing from the gas to the particle phases. In this work, a comparison of three state-of-the-art aerosol chemical characterization techniques has been performed as part of a chamber study on the biogenic SOA formation and aging. The aerosol collection module (ACM), the chemical analysis of aerosol on-line (CHARON) and the collection thermal desorption unit (TD) are different aerosol sampling inlets utilizing a Proton Transfer Time of Flight Mass Spectrometer (PTR-ToF-MS). These techniques were deployed at the atmosphere simulation chamber SAPHIR to perform oxidation experiments using different biogenic precursors, ranging from singe precursor experiments (β-pinene, limonene), their mixture and real plant emissions (*Pinus sylvestris L.*). Focus was given on the gas-to-particle partitioning of major biogenic oxidation products, expressed throughout this work as the saturation mass concentration C*. Determination of the C* of the individual ions was performed based on the parallel measurement of the signal in the gas- and particle-phase.

The total aerosol concentration recovery of the PTR based techniques, compared to an SMPS, was 80 ± 10%, 51 ± 5% and 27 ± 3% for CHARON, ACM and TD, respectively. In contrast, an AMS concurrently operated and with no collection efficiency correction applied, showed a recovery of 67%. The three PTR based techniques were capable of measuring the same major contributing signals for the different monoterpene oxidation products studied. These attributed compounds corresponded to a high fraction of the overall SOA mass concentration with 30%, 50% and 10% of the overall mass being explained for ACM, CHARON and TD, respectively. Additional comparison to previous publications showed that these compounds corresponded to known products of the monoterpenes studied. Both the ACM and TD collection and thermal desorption design provided additional information on their volatility and showed similar trends. Compounds containing higher molecular oxygen number ($n_O \geq 2$) contributed more to the aerosol fraction desorbed at high temperatures (250°C) than lower oxygenated compounds ($n_O < 2$) which were more efficiently desorbed at low temperatures (100°C).

Oxygen to carbon ratios (O:C) increased while SOA production and ageing proceeded. All instruments had comparable O:C trends during the course of an experiment. Good agreement was found for the ACM and TD O:C values (< 3% difference) while CHARON showed 20 to 35% higher O:C ratios.

Despite significant difference in the aerosol collection and desorption techniques, the major reason for the discrepancies was the different operating conditions of the PTR-ToF-MS. Laboratory case studies supported that E/N conditions played a crucial role in carbon-oxygen bond breakage leading to lower O:C ratios at high E/N. Since ACM and TD were operated at higher E/N compared to CHARON this resulted to higher fragmentation, thus affecting their oxygen and carbon content and mass recovery. Compared to AMS, PTRMS is a soft ionization technique even at high E/N and therefore less prone to fragmentation. AMS requires correction factors (Canagaratna et al., 2015), to determine O:C ratios whereas for PTRMS corrections were omitted. Determination of O:C ratios for the PTR based techniques was thus underestimated, explaining their difference to the HR-ToF-AMS (30 to 50% higher). Differences in the sampling and evaporation technique might introduce also deviations between the chemical characterizations i.e. due to thermal decomposition. This has to be studied in detail in future comparisons by operating the PTR-ToF-MS instruments under the same E/N conditions.

Decomposition pathways could directly affect the gas-to-particle partitioning of the different ions and thus the C* calculations. To reassure negligible biases due to instrumental fragmentation a method to identify and exclude ions affected by these decomposition pathways was developed and tested for each technique. Narrow volatility distributions were observed ranging from $\log_{10}$(C*) values from $0-4$, with species in the semi-volatile (SVOCs) to intermediate volatility (IVOCs) regime. The limonene oxidation experiment showed a lower volatility distribution when compared to the β-pinene oxidation experiment further supporting that limonene SOA are less volatile than β-pinene SOA (Lee et al., 2011). When comparing C* values obtained for species observed from all techniques, instruments showed good agreement, within 1 decade, with deviations explained by the different operating conditions of the PTRMS.

Determined species were mapped onto the 2D-VBS and results showed a decrease of the C* with increasing oxidation state and increasing oxygen atom number in accordance to previous findings (Kroll, 2011, Jimenez et al., 2009). These species accounted for 20-30 % of the total organic mass measured from an AMS. For species that overlapped with compounds detected

in previous publications a comparison to theoretical calculations was performed based on their molecular structure. Results showed good agreement for SVOCs, within the uncertainties of the measurements, while IVOCs introduced higher deviations. Detailed comparison of the partitioning values of a 1st generation product from the ozonolysis of β-pinene, nopinone, was performed to previous publications. Results showed agreement for the $\log_{10}(C^*)$ within ± 0.5 for all experimental approaches while theory showed differences of 3 orders of magnitude on the C* estimation. These major differences are discussed in terms of possible uncertainties biasing the experimental values from (1) existence of isomers within a studied *m/z*, (2) thermal and ionic fragmentation of higher molecular weight compounds, produced by accretion and oligomerization reactions, to the *m/z* range detected by the PTRMS, (3) non-idealities of the organic mixtures and (4) the phase-state of the bulk OA affecting the partitioning equilibrium time-scales (τ_{eq}) of the individual compounds. Results point towards possible interferences by thermal and ionic fragmentation as well as kinetic influences in the distribution between gas- and particle-phase with gas-phase condensation in the particle-phase and irreversible uptake. These findings further promote future work and parallel measurement of the phase-state of the OA combined with compound specific volatility determination from the PTR-based techniques.

Overall, all PTR based techniques were able to reproduce the overall general chemical composition of the OA (same major contributing compounds) and measure compounds supported from previous publications. These techniques can provide valuable insight on the chemical characteristics of freshly formed and aged BSOA, and on thermodynamic properties such as gas-to-particle partitioning values and volatility patterns on a compound specific level.

For the ACM, future work includes the improvement and minimization of the required collection times by attaching an aerosol enrichment system at the ACM inlet. By pre-concentrating the particles, the mass loading introduced in the vacuum system of the ACM could increase by up to a factor of 10 or more, thus decreasing the collection times down to a few minutes. The PTR-ToF-MS used in this work was a model with a relatively low mass resolution (m/Δm). Newly developed instruments like the VOCUS-PTR-ToF-MS, recently purchased by our institute, have a resolving power higher than 10000, thus increasing by a factor of 5 the capabilities of the ACM-PTR-ToF-MS. By coupling ACM to the VOCUS-PTR identification of isobaric compounds in complex mixtures could be achieved improving the reliability of higher molecular weight compounds identification.

Furthermore, laboratory investigation of single compounds to better understand the thermal dissociation pathways in the ACM would be of interest. By deriving the saturation mass concentration of e.g. nopinone in a single component system and performing parallel calibrations based on the thermograms obtained from the ACM desorption steps further insights on possible matrix artifacts when working in complex systems can be derived. Moving from well-defined single component systems to complex chemical systems using the simulation chamber SAPHIR would provide further insight in the quantification of the different effects e.g. ionic and thermal dissociation. Finally, parallel measurements using the PTR-based together with GC-based techniques like the TAG would provide further insights on the isomer identification while the usage of aerosol impactors to define the phase-state of the OA would provide further insight on the compound specific volatility estimations.

List of abbreviations and parameters

Abbreviation	Meaning
ACM	Aerosol Collection Module
AMS	Aerosol Mass Spectrometer
BSOA	Biogenic Secondary Organic Aerosol
BVOC	Biogenic Volatile Organic Compounds
CE	Collection Efficiency
CHARON	Chemical Analysis of Aerosol On-line
$CHARON_{65}$	Chemical Analysis of Aerosol On-line operated at 65 Td
$CHARON_{100}$	Chemical Analysis of Aerosol On-line operated at 100 Td
CPC	Condensation Particle Counter
CTD	Collection Thermal Desorption
EDB	Electrodynamic Balance
ELVOC	Extremely-Low-Volatility Organic Compounds
FIGAERO	Filter Inlet for Gases and Aerosols
GC	Gas-Chromatography
GUI	Graphical User Interface
IVOC	Intermediate-Volatility Organic Compounds
KEMS	Knudsen Effusion Mass Spectrometer
LED	Light-Emitting Diode
LOD	Limit of Detection
LVOC	Low-Volatility Organic Compounds
MVK	Methyl Vinyl Ketone
MW	Molecular Weight
NVD	Normalized Volatility Distribution
OA	Organic Aerosol
PID	Proportional-Integral-Derivative
PLUS	Plant Chamber Unit for Simulation
PM 1	Particulate matter, smaller than 1.0 µm
PM 2.5	Particulate matter, smaller than 2.5 µm
PTR	Proton-Transfer-Reaction
PTRMS	Proton-Transfer-Reaction Mass Spectrometer
PTR-ToF-MS	Proton-Transfer-Reaction Time-of-Flight Mass Spectrometer

RTC	Retention Time Correlation
SAPHIR	Simulation of Atmospheric Photochemistry in a Large Reaction Chamber
SMPS	Scanning Mobility Particle Sizer
SOA	Secondary Organic Aerosol
SV	Semi-Volatile
SVOC	Semi-Volatile Organic Compounds
TDMS	Thermal Desorption Mass Spectrometry
VBS	Volatility-Basis-Set
VOC	Volatile Organic Compounds
TD	Collection Thermal Desorption unit and ThermoDenuder
TAG	Thermal Desorption Aerosol Gas Chromatograph
VAPS	Volatility and Polarity Separator
2D-GC	2-dimensional Gas Chromatography
2D-VBS	2-Dimensional Volatility-Basis-Set

Parameter	**Meaning**
$\Delta H_{trs,i}$	Molar enthalpy change upon phase transition
$\Delta \nu_{m,i}$	Molar volume upon phase transition
$\zeta_{x,i}$	Mole-fraction-based activity coefficient
$C_{aer,i}$	Aerosol mass concentration of compound i
C*	Saturation mass concentration
C_p	Heat capacity
E/N	Electric field strength to buffer gas density
F_{N_2}	Flow of the nitrogen carrier gas
F_{col}	Collection flow rate
Gi	Gas-phase mass concentration of compound i
MW_i	Molecular weight of compound i
MW_{OA}	Mean molecular weight of the condensed organic phase
$n_{mean,i}$	Arithmetic mean of the mixing ratio during the aerosol analysis in the nitrogen flow
$n_{oxygen\ atoms\ i,\ at\ x\ temperature}$	Mass concentration contribution of all species containing i number of oxygen atoms at x evaporation temperature

OA	Organic aerosol mass concentration
O:C	Oxygen to carbon ratio
OS_c	Oxidation State of a compound i
$\overline{OS}_c$	Bulk Oxidation State of organic aerosol
P	Ambient pressure
P_i	Particle-phase mass concentration of compound i
p_{eq}^{i}	Equilibrium vapor pressure
p_i^o	Pure component saturation vapor pressure
$p_{i,L}$	Sub-cooled liquid saturation vapor pressure
R	Universal gas law
S_i	Sensitivity of compound i
T	Temperature
t_{meas}	Aerosol desorption duration
t_{col}	Aerosol collection duration

List of Figures

List of Tables

References

Aiken, A. C., Decarlo, P. F., Kroll, J. H., Worsnop, D. R., Huffman, J. A., Docherty, K. S., Ulbrich, I. M., Mohr, C., Kimmel, J. R., Sueper, D., Sun, Y., Zhang, Q., Trimborn, A., Northway, M., Ziemann, P. J., Canagaratna, M. R., Onasch, T. B., Alfarra, M. R., Prevot, A. S. H., Dommen, J., Duplissy, J., Metzger, A., Baltensperger, U. & Jimenez, J. L. 2008. O/C and OM/OC Ratios of Primary, Secondary, and Ambient Organic Aerosols with High-Resolution Time-of-Flight Aerosol Mass Spectrometry. *Environmental Science & Technology,* 42**,** 4478-4485.

An, W. J., Pathak, R. K., Lee, B.-H. & Pandis, S. N. 2007. Aerosol volatility measurement using an improved thermodenuder: Application to secondary organic aerosol. *Journal of Aerosol Science,* 38**,** 305-314.

Aumont, B., Szopa, S. & Madronich, S. 2005. Modelling the evolution of organic carbon during its gas-phase tropospheric oxidation: development of an explicit model based on a self generating approach. *Atmos. Chem. Phys.,* 5**,** 2497-2517.

Barsanti, K. C., Kroll, J. H. & Thornton, J. A. 2017. Formation of Low-Volatility Organic Compounds in the Atmosphere: Recent Advancements and Insights. *J Phys Chem Lett,* 8**,** 1503-1511.

Bilde, M., Barsanti, K., Booth, M., Cappa, C. D., Donahue, N. M., Emanuelsson, E. U., Mcfiggans, G., Krieger, U. K., Marcolli, C., Topping, D., Ziemann, P., Barley, M., Clegg, S., Dennis-Smither, B., Hallquist, M., Hallquist, A. M., Khlystov, A., Kulmala, M., Mogensen, D., Percival, C. J., Pope, F., Reid, J. P., Ribeiro Da Silva, M. A., Rosenoern, T., Salo, K., Soonsin, V. P., Yli-Juuti, T., Prisle, N. L., Pagels, J., Rarey, J., Zardini, A. A. & Riipinen, I. 2015. Saturation vapor pressures and transition enthalpies of low-volatility organic molecules of atmospheric relevance: from dicarboxylic acids to complex mixtures. *Chem Rev,* 115**,** 4115-56.

Booth, A. M., Markus, T., Mcfiggans, G., Percival, C. J., Mcgillen, M. R. & Topping, D. O. 2009. Design and construction of a simple Knudsen Effusion Mass Spectrometer (KEMS) system for vapour pressure measurements of low volatility organics. *Atmos. Meas. Tech.,* 2**,** 355-361.

Bosque, R. & Sales, J. 2002. Polarizabilities of Solvents from the Chemical Composition. *Journal of Chemical Information and Computer Sciences,* 42**,** 1154-1163.

Camredon, M., Hamilton, J. F., Alam, M. S., Wyche, K. P., Carr, T., White, I. R., Monks, P. S., Rickard, A. R. & Bloss, W. J. 2010. Distribution of gaseous and particulate organic composition during dark α-pinene ozonolysis. *Atmos. Chem. Phys.,* 10**,** 2893-2917.

Canagaratna, M. R., Jayne, J. T., Jimenez, J. L., Allan, J. D., Alfarra, M. R., Zhang, Q., Onasch, T. B., Drewnick, F., Coe, H., Middlebrook, A., Delia, A., Williams, L. R., Trimborn, A. M., Northway, M. J., Decarlo, P. F., Kolb, C. E., Davidovits, P. & Worsnop, D. R. 2007. Chemical and microphysical characterization of ambient aerosols with the aerodyne aerosol mass spectrometer. *Mass Spectrom Rev,* 26**,** 185-222.

Canagaratna, M. R., Jimenez, J. L., Kroll, J. H., Chen, Q., Kessler, S. H., Massoli, P., Hildebrandt Ruiz, L., Fortner, E., Williams, L. R., Wilson, K. R., Surratt, J. D., Donahue, N. M., Jayne, J. T. & Worsnop, D. R. 2015. Elemental ratio measurements of organic compounds using aerosol mass spectrometry: characterization, improved calibration, and implications. *Atmospheric Chemistry and Physics,* 15**,** 253-272.

Cappa, C. D. & Jimenez, J. L. 2010. Quantitative estimates of the volatility of ambient organic aerosol. *Atmospheric Chemistry and Physics,* 10**,** 5409-5424.

Cappellin, L., Karl, T., Probst, M., Ismailova, O., Winkler, P. M., Soukoulis, C., Aprea, E., Märk, T. D., Gasperi, F. & Biasioli, F. 2012. On Quantitative Determination of Volatile Organic Compound Concentrations Using Proton Transfer Reaction Time-of-Flight Mass Spectrometry. *Environmental Science & Technology,* 46**,** 2283-2290.

Chen, J. & Griffin, R. 2005. Modeling secondary organic aerosol formation from oxidation of -pinene, -pinene, and -limonene. *Atmospheric Environment,* 39**,** 7731-7744.

Clegg, S. L., Seinfeld, J. H. & Brimblecombe, P. 2001. Thermodynamic modelling of aqueous aerosols containing electrolytes and dissolved organic compounds. *Journal of Aerosol Science,* 32**,** 713-738.

Compernolle, S., Ceulemans, K. & Muller, J. F. 2010. Vapor pressure estimation methods applied to secondary organic aerosol constituents from α-pinene oxidation: an intercomparison study. *Atmos. Chem. Phys.,* 10**,** 6271-6282.

Cordes, W. & Rarey, J. 2002. A new method for the estimation of the normal boiling point of non-electrolyte organic compounds. *Fluid Phase Equilib.,* 201**,** 409-433.

Cross, E. S., Slowik, J. G., Davidovits, P., Allan, J. D., Worsnop, D. R., Jayne, J. T., Lewis, D. K., Canagaratna, M. & Onasch, T. B. 2007. Laboratory and Ambient Particle Density Determinations using Light Scattering in Conjunction with Aerosol Mass Spectrometry. *Aerosol Science and Technology,* 41**,** 343-359.

De Gouw, J. & Warneke, C. 2007. Measurements of volatile organic compounds in the earth's atmosphere using proton-transfer-reaction mass spectrometry. *Mass Spectrom Rev,* 26**,** 223-57.

Decarlo, P. F., Kimmel, J. R., Trimborn, A., Northway, M. J., Jayne, J. T., Aiken, A. C., Gonin, M., Fuhrer, K., Horvath, T., Docherty, K. S., Worsnop, D. R. & Jimenez, J. L. 2006. Field-Deployable, High-Resolution, Time-of-Flight Aerosol Mass Spectrometer. *Analytical Chemistry,* 78**,** 8281-8289.

Dommen, J., Hellén, H., Saurer, M., Jaeggi, M., Siegwolf, R., Metzger, A., Duplissy, J., Fierz, M. & Baltensperger, U. 2009. Determination of the Aerosol Yield of Isoprene in the Presence of an Organic Seed with Carbon Isotope Analysis. *Environmental Science & Technology,* 43**,** 6697-6702.

Donahue, N. M., Chuang, W., Epstein, S. A., Kroll, J. H., Worsnop, D. R., Robinson, A. L., Adams, P. J. & Pandis, S. N. 2013. Why do organic aerosols exist? Understanding aerosol lifetimes using the two-dimensional volatility basis set. *Environmental Chemistry,* 10**,** 151.

Donahue, N. M., Epstein, S. A., Pandis, S. N. & Robinson, A. L. 2011. A two-dimensional volatility basis set: 1. organic-aerosol mixing thermodynamics. *Atmospheric Chemistry and Physics,* 11**,** 3303-3318.

Donahue, N. M., Kroll, J. H., Pandis, S. N. & Robinson, A. L. 2012. A two-dimensional volatility basis set – Part 2: Diagnostics of organic-aerosol evolution. *Atmospheric Chemistry and Physics,* 12**,** 615-634.

Donahue, N. M., Robinson, A. L., Stanier, C. O. & Pandis, S. N. 2006. Coupled Partitioning, Dilution, and Chemical Aging of Semivolatile Organics. *Environmental Science & Technology,* 40**,** 2635-2643.

Donahue, N. M., Robinson, A. L., Trump, E. R., Riipinen, I. & Kroll, J. H. 2014. Volatility and aging of atmospheric organic aerosol. *Top Curr Chem,* 339**,** 97-143.

Ehn, M., Thornton, J. A., Kleist, E., Sipila, M., Junninen, H., Pullinen, I., Springer, M., Rubach, F., Tillmann, R., Lee, B., Lopez-Hilfiker, F., Andres, S., Acir, I. H., Rissanen, M., Jokinen, T., Schobesberger, S., Kangasluoma, J., Kontkanen, J., Nieminen, T., Kurten, T., Nielsen, L. B., Jorgensen, S., Kjaergaard, H. G., Canagaratna, M., Maso, M. D., Berndt, T., Petaja, T., Wahner, A., Kerminen, V. M., Kulmala, M., Worsnop, D. R., Wildt, J. & Mentel, T. F. 2014. A large source of low-volatility secondary organic aerosol. *Nature,* 506**,** 476-9.

Eichler, P., Müller, M., D'anna, B. & Wisthaler, A. 2015. A novel inlet system for online chemical analysis of semi-volatile submicron particulate matter. *Atmospheric Measurement Techniques,* 8**,** 1353-1360.

Eichler, P., Müller, M., Rohmann, C., Stengel, B., Orasche, J., Zimmermann, R. & Wisthaler, A. 2017. Lubricating Oil as a Major Constituent of Ship Exhaust Particles. *Environmental Science & Technology Letters,* 4**,** 54-58.

Epstein, S. A., Riipinen, I. & Donahue, N. M. 2010. A Semiempirical Correlation between Enthalpy of Vaporization and Saturation Concentration for Organic Aerosol. *Environmental Science & Technology,* 44**,** 743-748.

Faulhaber, A. E., Thomas, B. M., Jimenez, J. L., Jayne, J. T., Worsnop, D. R. & Ziemann, P. J. 2009. Characterization of a thermodenuder-particle beam mass spectrometer system for the study of organic aerosol volatility and composition. *Atmos. Meas. Tech.,* 2**,** 15-31.

Fredenslund, A., Jones, R. L. & Prausnitz, J. M. 1975. Group-contribution estimation of activity coefficients in nonideal liquid mixtures. *AIChE Journal,* 21**,** 1086-1099.

Gkatzelis, G. I., Papanastasiou, D. K., Florou, K., Kaltsonoudis, C., Louvaris, E. & Pandis, S. N. 2016. Measurement of nonvolatile particle number size distribution. *Atmospheric Measurement Techniques,* 9**,** 103-114.

Gkatzelis, G. I., Tillmann, R., Hohaus, T., Müller, M., Eichler, P., Xu, K.-M., Schlag, P., Schmitt, S. H., Wegener, R., Kaminski, M., Holzinger, R., Wisthaler, A. & Kiendler-Scharr, A. 2017. Comparison of three aerosol chemical characterization techniques utilizing PTR-ToF-MS: A study on freshly formed and aged biogenic SOA. *Atmospheric Measurement Techniques Discussions***,** 1-31.

Goldstein, A. H. & Galbally, I. E. 2007. Known and Unexplored Organic Constituents in the Earth's Atmosphere. *Environmental Science & Technology,* 41**,** 1514-1521.

Graus, M., Muller, M. & Hansel, A. 2010. High resolution PTR-TOF: quantification and formula confirmation of VOC in real time. *J Am Soc Mass Spectrom,* 21**,** 1037-44.

Guenther, A. B., Jiang, X., Heald, C. L., Sakulyanontvittaya, T., Duhl, T., Emmons, L. K. & Wang, X. 2012. The Model of Emissions of Gases and Aerosols from Nature version 2.1 (MEGAN2.1): an extended and updated framework for modeling biogenic emissions. *Geoscientific Model Development,* 5**,** 1471-1492.

Hallquist, M., Wenger, J. C., Baltensperger, U., Rudich, Y., Simpson, D., Claeys, M., Dommen, J., Donahue, N. M., George, C., Goldstein, A. H., Hamilton, J. F., Herrmann, H., Hoffmann, T., Iinuma, Y., Jang, M., Jenkin, M. E., Jimenez, J. L., Kiendler-Scharr, A., Maenhaut, W., Mcfiggans, G., Mentel, T. F., Monod, A., Prévôt, A. S. H., Seinfeld, J. H., Surratt, J. D., Szmigielski, R. & Wildt, J. 2009. The

formation, properties and impact of secondary organic aerosol: current and emerging issues. *Atmos. Chem. Phys.,* 9**,** 5155-5236.

Heald, C. L. & Spracklen, D. V. 2015. Land use change impacts on air quality and climate. *Chem Rev,* 115**,** 4476-96.

Hildebrandt, L., Henry, K. M., Kroll, J. H., Worsnop, D. R., Pandis, S. N. & Donahue, N. M. 2011. Evaluating the Mixing of Organic Aerosol Components Using High-Resolution Aerosol Mass Spectrometry. *Environmental Science & Technology,* 45**,** 6329-6335.

Hohaus, T., Gensch, I., Kimmel, J. R., Worsnop, D. R. & Kiendler-Scharr, A. 2015. Experimental determination of the partitioning coefficient of β-pinene oxidation products in SOAs. *Physical Chemistry Chemical Physics,* 17**,** 14796-14804.

Hohaus, T., Kuhn, U., Andres, S., Kaminski, M., Rohrer, F., Tillmann, R., Wahner, A., Wegener, R., Yu, Z. & Kiendler-Scharr, A. 2016. A new plant chamber facility, PLUS, coupled to the atmosphere simulation chamber SAPHIR. *Atmospheric Measurement Techniques,* 9**,** 1247-1259.

Hohaus, T., Trimborn, D., Kiendler-Scharr, A., Gensch, I., Laumer, W., Kammer, B., Andres, S., Boudries, H., Smith, K. A., Worsnop, D. R. & Jayne, J. T. 2010. A new aerosol collector for quasi on-line analysis of particulate organic matter: the Aerosol Collection Module (ACM) and first applications with a GC/MS-FID. *Atmospheric Measurement Techniques,* 3**,** 1423-1436.

Holzinger, R. 2015. PTRwid: A new widget tool for processing PTR-TOF-MS data. *Atmospheric Measurement Techniques,* 8**,** 3903-3922.

Holzinger, R., Goldstein, A. H., Hayes, P. L., Jimenez, J. L. & Timkovsky, J. 2013. Chemical evolution of organic aerosol in Los Angeles during the CalNex 2010 study. *Atmospheric Chemistry and Physics,* 13**,** 10125-10141.

Holzinger, R., Kasper-Giebl, A., Staudinger, M., Schauer, G. & Röckmann, T. 2010a. Analysis of the chemical composition of organic aerosol at the Mt. Sonnblick observatory using a novel high mass resolution thermal-desorption proton-transfer-reaction mass-spectrometer (hr-TD-PTR-MS). *Atmospheric Chemistry and Physics,* 10**,** 10111-10128.

Holzinger, R., Williams, J., Herrmann, F., Lelieveld, J., Donahue, N. M. & Röckmann, T. 2010b. Aerosol analysis using a Thermal-Desorption Proton-Transfer-Reaction Mass Spectrometer (TD-PTR-MS): a new approach to study processing of organic aerosols. *Atmos. Chem. Phys.,* 10**,** 2257-2267.

Huffman, J. A., Ziemann, P. J., Jayne, J. T., Worsnop, D. R. & Jimenez, J. L. 2008. Development and Characterization of a Fast-Stepping/Scanning Thermodenuder for Chemically-Resolved Aerosol Volatility Measurements. *Aerosol Science and Technology,* 42**,** 395-407.

Isaacman-Vanwertz, G., Massoli, P., O'brien, R. E., Nowak, J. B., Canagaratna, M. R., Jayne, J. T., Worsnop, D. R., Su, L., Knopf, D. A., Misztal, P. K., Arata, C., Goldstein, A. H. & Kroll, J. H. 2017. Using advanced mass spectrometry techniques to fully characterize atmospheric organic carbon: current capabilities and remaining gaps. *Faraday Discussions*.

Isaacman-Vanwertz, G., Yee, L. D., Kreisberg, N. M., Wernis, R., Moss, J. A., Hering, S. V., De Sa, S. S., Martin, S. T., Alexander, M. L., Palm, B. B., Hu, W., Campuzano-Jost, P., Day, D. A., Jimenez, J. L., Riva, M., Surratt, J. D., Viegas, J., Manzi, A.,

Edgerton, E., Baumann, K., Souza, R., Artaxo, P. & Goldstein, A. H. 2016. Ambient Gas-Particle Partitioning of Tracers for Biogenic Oxidation. *Environ Sci Technol*.

Isaacman, G., Kreisberg, N. M., Yee, L. D., Worton, D. R., Chan, A. W. H., Moss, J. A., Hering, S. V. & Goldstein, A. H. 2014. Online derivatization for hourly measurements of gas- and particle-phase semi-volatile oxygenated organic compounds by thermal desorption aerosol gas chromatography (SV-TAG). *Atmospheric Measurement Techniques,* 7**,** 4417-4429.

Isaacman, G., Worton, D. R., Kreisberg, N. M., Hennigan, C. J., Teng, A. P., Hering, S. V., Robinson, A. L., Donahue, N. M. & Goldstein, A. H. 2011. Understanding evolution of product composition and volatility distribution through in-situ GC × GC analysis: a case study of longifolene ozonolysis. *Atmospheric Chemistry and Physics,* 11**,** 5335-5346.

Jang, M. & Kamens, R. M. 2001. Atmospheric Secondary Aerosol Formation by Heterogeneous Reactions of Aldehydes in the Presence of a Sulfuric Acid Aerosol Catalyst. *Environmental Science & Technology,* 35**,** 4758-4766.

Jaoui, M., Corse, E., Kleindienst, T. E., Offenberg, J. H., Lewandowski, M. & Edney, E. O. 2006. Analysis of Secondary Organic Aerosol Compounds from the Photooxidation of d-Limonene in the Presence of NOX and their Detection in Ambient PM2.5. *Environmental Science & Technology,* 40**,** 3819-3828.

Jenkin, M. E. 2004. Modelling the formation and composition of secondary organic aerosol from α- and β-pinene ozonolysis using MCM v3 *Atmos. Chem. Phys.,* 4**,** 1741-1757.

Jimenez, J. L., Canagaratna, M. R., Donahue, N. M., Prevot, A. S. H., Zhang, Q., Kroll, J. H., Decarlo, P. F., Allan, J. D., Coe, H., Ng, N. L., Aiken, A. C., Docherty, K. S., Ulbrich, I. M., Grieshop, A. P., Robinson, A. L., Duplissy, J., Smith, J. D., Wilson, K. R., Lanz, V. A., Hueglin, C., Sun, Y. L., Tian, J., Laaksonen, A., Raatikainen, T., Rautiainen, J., Vaattovaara, P., Ehn, M., Kulmala, M., Tomlinson, J. M., Collins, D. R., Cubison, M. J., Dunlea, J., Huffman, J. A., Onasch, T. B., Alfarra, M. R., Williams, P. I., Bower, K., Kondo, Y., Schneider, J., Drewnick, F., Borrmann, S., Weimer, S., Demerjian, K., Salcedo, D., Cottrell, L., Griffin, R., Takami, A., Miyoshi, T., Hatakeyama, S., Shimono, A., Sun, J. Y., Zhang, Y. M., Dzepina, K., Kimmel, J. R., Sueper, D., Jayne, J. T., Herndon, S. C., Trimborn, A. M., Williams, L. R., Wood, E. C., Middlebrook, A. M., Kolb, C. E., Baltensperger, U. & Worsnop, D. R. 2009. Evolution of Organic Aerosols in the Atmosphere. *Science,* 326.

Joback, K. G. & Reid, R. C. 1987. Estimation of pure-component properties from group contributions. *Chem. Eng. Commun.,* 57**,** 233-43.

Jordan, A., Haidacher, S., Hanel, G., Hartungen, E., Märk, L., Seehauser, H., Schottkowsky, R., Sulzer, P. & Märk, T. D. 2009. A high resolution and high sensitivity proton-transfer-reaction time-of-flight mass spectrometer (PTR-TOF-MS). *International Journal of Mass Spectrometry,* 286**,** 122-128.

Kahnt, A. 2012. *Semivolatile compounds from atmospheric monoterpene oxidation* PhD, Universität Leipzig.

Kanakidou, M., Seinfeld, J., Pandis, S., Barnes, I., Dentener, F., Facchini, M., Dingenen, R. V., Ervens, B., Nenes, A. & Nielsen, C. 2005. Organic aerosol and global climate modelling: a review. *Atmospheric Chemistry and Physics,* 5**,** 1053-1123.

Karnezi, E., Riipinen, I. & Pandis, S. N. 2014. Measuring the atmospheric organic aerosol volatility distribution: a theoretical analysis. *Atmospheric Measurement Techniques,* 7**,** 2953-2965.

Kiehl, J. T. 2007. Twentieth century climate model response and climate sensitivity. *Geophysical Research Letters,* 34.

Kiendler-Scharr, A., Zhang, Q., Hohaus, T., Kleist, E., Mensah, A., Mentel, T. F., Spindler, C., Uerlings, R., Tillmann, R. & Wildt, J. 2009. Aerosol Mass Spectrometric Features of Biogenic SOA: Observations from a Plant Chamber and in Rural Atmospheric Environments. *Environmental Science & Technology,* 43**,** 8166-8172.

Kreisberg, N. M., Hering, S. V., Williams, B. J., Worton, D. R. & Goldstein, A. H. 2009. Quantification of Hourly Speciated Organic Compounds in Atmospheric Aerosols, Measured by an In-Situ Thermal Desorption Aerosol Gas Chromatograph (TAG). *Aerosol Science and Technology,* 43**,** 38-52.

Kroll, J. H. 2011. Carbon oxidation state as a metric for describing the chemistry of atmospheric organic aerosol. *Nature Chemistry,* 3.

Kundu, S., Fisseha, R., Putman, A. L., Rahn, T. A. & Mazzoleni, L. R. 2012. High molecular weight SOA formation during limonene ozonolysis: insights from ultrahigh-resolution FT-ICR mass spectrometry characterization. *Atmospheric Chemistry and Physics,* 12**,** 5523-5536.

Künzli, N., Jerrett, M., Mack, W. J., Beckerman, B., Labree, L., Gilliland, F., Thomas, D., Peters, J. & Hodis, H. N. 2004. Ambient Air Pollution and Atherosclerosis in Los Angeles. *Environmental Health Perspectives,* 113**,** 201-206.

Lee, B.-H., Pierce, J. R., Engelhart, G. J. & Pandis, S. N. 2011. Volatility of secondary organic aerosol from the ozonolysis of monoterpenes. *Atmospheric Environment,* 45**,** 2443-2452.

Lelieveld, J., Evans, J. S., Fnais, M., Giannadaki, D. & Pozzer, A. 2015. The contribution of outdoor air pollution sources to premature mortality on a global scale. *Nature,* 525**,** 367-71.

Leungsakul, S., Jaoui, M. & Kamens, R. M. 2005a. Kinetic Mechanism for Predicting Secondary Organic Aerosol Formation from the Reaction of d-Limonene with Ozone. *Environmental Science & Technology,* 39**,** 9583-9594.

Leungsakul, S., Jeffries, H. E. & Kamens, R. M. 2005b. A kinetic mechanism for predicting secondary aerosol formation from the reactions of d-limonene in the presence of oxides of nitrogen and natural sunlight. *Atmospheric Environment,* 39**,** 7063-7082.

Liu, P., Ziemann, P. J., Kittelson, D. B. & Mcmurry, P. H. 1995a. Generating Particle Beams of Controlled Dimensions and Divergence: I. Theory of Particle Motion in Aerodynamic Lenses and Nozzle Expansions. *Aerosol Science and Technology,* 22**,** 293-313.

Liu, P., Ziemann, P. J., Kittelson, D. B. & Mcmurry, P. H. 1995b. Generating Particle Beams of Controlled Dimensions and Divergence: II. Experimental Evaluation of Particle Motion in Aerodynamic Lenses and Nozzle Expansions. *Aerosol Science and Technology,* 22**,** 314-324.

Lopez-Hilfiker, F. D., Mohr, C., D'ambro, E. L., Lutz, A., Riedel, T. P., Gaston, C. J., Iyer, S., Zhang, Z., Gold, A., Surratt, J. D., Lee, B. H., Kurten, T., Hu, W. W., Jimenez, J., Hallquist, M. & Thornton, J. A. 2016. Molecular Composition and Volatility of

Organic Aerosol in the Southeastern U.S.: Implications for IEPOX Derived SOA. *Environ Sci Technol,* 50**,** 2200-9.

Lopez-Hilfiker, F. D., Mohr, C., Ehn, M., Rubach, F., Kleist, E., Wildt, J., Mentel, T. F., Carrasquillo, A. J., Daumit, K. E., Hunter, J. F., Kroll, J. H., Worsnop, D. R. & Thornton, J. A. 2015. Phase partitioning and volatility of secondary organic aerosol components formed from α-pinene ozonolysis and OH oxidation: the importance of accretion products and other low volatility compounds. *Atmospheric Chemistry and Physics,* 15**,** 7765-7776.

Lopez-Hilfiker, F. D., Mohr, C., Ehn, M., Rubach, F., Kleist, E., Wildt, J., Mentel, T. F., Lutz, A., Hallquist, M., Worsnop, D. & Thornton, J. A. 2014. A novel method for online analysis of gas and particle composition: description and evaluation of a Filter Inlet for Gases and AEROsols (FIGAERO). *Atmospheric Measurement Techniques,* 7**,** 983-1001.

Louvaris, E. E., Florou, K., Karnezi, E., Papanastasiou, D. K., Gkatzelis, G. I. & Pandis, S. N. 2017. Volatility of source apportioned wintertime organic aerosol in the city of Athens. *Atmospheric Environment,* 158**,** 138-147.

Mackay, D., Bobra, A., Chan, D. W. & Shiu, W. Y. 1982. Vapor-pressure correlations for low-volatility environmental chemicals. *Environ. Sci. Technol.,* 16**,** 645-9.

Martinez, R. E., Williams, B. J., Zhang, Y., Hagan, D., Walker, M., Kreisberg, N. M., Hering, S. V., Hohaus, T., Jayne, J. T. & Worsnop, D. R. 2016. Development of a volatility and polarity separator (VAPS) for volatility- and polarity-resolved organic aerosol measurement. *Aerosol Science and Technology,* 50**,** 255-271.

Mcfiggans, G., Topping, D. O. & Barley, M. H. 2010. The sensitivity of secondary organic aerosol component partitioning to the predictions of component properties – Part 1: A systematic evaluation of some available estimation techniques. *Atmospheric Chemistry and Physics,* 10**,** 10255-10272.

Mensah, A. A., Holzinger, R., Otjes, R., Trimborn, A., Mentel, T. F., Ten Brink, H., Henzing, B. & Kiendler-Scharr, A. 2012. Aerosol chemical composition at Cabauw, The Netherlands as observed in two intensive periods in May 2008 and March 2009. *Atmospheric Chemistry and Physics,* 12**,** 4723-4742.

Mitchem, L. & Reid, J. P. 2008. Optical manipulation and characterisation of aerosol particles using a single-beam gradient force optical trap. *Chem Soc Rev,* 37**,** 756-69.

Müller, M., Mikoviny, T., Jud, W., D'anna, B. & Wisthaler, A. 2013. A new software tool for the analysis of high resolution PTR-TOF mass spectra. *Chemometrics and Intelligent Laboratory Systems,* 127**,** 158-165.

Murphy, B. N., Donahue, N. M., Fountoukis, C., Dall'osto, M., O'dowd, C., Kiendler-Scharr, A. & Pandis, S. N. 2012. Functionalization and fragmentation during ambient organic aerosol aging: application of the 2-D volatility basis set to field studies. *Atmospheric Chemistry and Physics,* 12**,** 10797-10816.

Myrdal, P. B. & Yalkowsky, S. H. 1997. Estimating Pure Component Vapor Pressures of Complex Organic Molecules. *Ind. Eng. Chem. Res.,* 36**,** 2494-2499.

Nannoolal, Y., Rarey, J. & Ramjugernath, D. 2008. Estimation of pure component properties. Part 3. Estimation of the vapor pressure of non-electrolyte organic compounds via group contributions and group interaction. *Fluid Phase Equilib.,* 269**,** 117-133.

Nannoolal, Y., Rarey, J., Ramjugernath, D. & Cordes, W. 2004. Estimation of pure component properties. *Fluid Phase Equilib.,* 226**,** 45-63.

Odum, J. R., Hoffmann, T., Bowman, F., Collins, D., Flagan, R. C. & Seinfeld, J. H. 1996. Gas/Particle Partitioning and Secondary Organic Aerosol Yields. *Environmental Science & Technology,* 30**,** 2580-2585.

Pankow, J. F. 1994. An absorption model of gas/particle partitioning of organic compounds in the atmosphere. *Atmospheric Environment,* 28**,** 185-188.

Pankow, J. F. & Asher, W. E. 2008. SIMPOL.1: a simple group contribution method for predicting vapor pressures and enthalpies of vaporization of multifunctional organic compounds. *Atmos. Chem. Phys.,* 8**,** 2773-2796.

Pankow, J. F. & Barsanti, K. C. 2009. The carbon number-polarity grid: A means to manage the complexity of the mix of organic compounds when modeling atmospheric organic particulate matter. *Atmospheric Environment,* 43**,** 2829-2835.

Pope, F. D., Dennis-Smither, B. J., Griffiths, P. T., Clegg, S. L. & Cox, R. A. 2010. Studies of Single Aerosol Particles Containing Malonic Acid, Glutaric Acid, and Their Mixtures with Sodium Chloride. I. Hygroscopic Growth. *Journal of Physical Chemistry,* 114**,** 5335-5341.

Pöschl, U. & Shiraiwa, M. 2015. Multiphase chemistry at the atmosphere-biosphere interface influencing climate and public health in the anthropocene. *Chem Rev,* 115**,** 4440-75.

Praplan, A. P., Schobesberger, S., Bianchi, F., Rissanen, M. P., Ehn, M., Jokinen, T., Junninen, H., Adamov, A., Amorim, A., Dommen, J., Duplissy, J., Hakala, J., Hansel, A., Heinritzi, M., Kangasluoma, J., Kirkby, J., Krapf, M., Kürten, A., Lehtipalo, K., Riccobono, F., Rondo, L., Sarnela, N., Simon, M., Tomé, A., Tröstl, J., Winkler, P. M., Williamson, C., Ye, P., Curtius, J., Baltensperger, U., Donahue, N. M., Kulmala, M. & Worsnop, D. R. 2014. Elemental composition and clustering of α-pinene oxidation products for different oxidation conditions. *Atmospheric Chemistry and Physics Discussions,* 14**,** 30799-30833.

Prisle, N. L., Engelhart, G. J., Bilde, M. & Donahue, N. M. 2010. Humidity influence on gas-particle phase partitioning ofα-pinene + O3secondary organic aerosol. *Geophysical Research Letters,* 37**,** n/a-n/a.

Riipinen, I., Pierce, J. R., Donahue, N. M. & Pandis, S. N. 2010. Equilibration time scales of organic aerosol inside thermodenuders: Evaporation kinetics versus thermodynamics. *Atmospheric Environment,* 44**,** 597-607.

Rohrer, F., Bohn, B., Brauers, T., Brüning, D., Johnen, F. J., Wahner, A. & Kleffmann, J. 2005. Characterisation of the photolytic HONO-source in the atmosphere simulation chamber SAPHIR. *Atmos. Chem. Phys.,* 5**,** 2189-2201.

Salvador, C. M., Ho, T. T., Chou, C. C. K., Chen, M. J., Huang, W. R. & Huang, S. H. 2016. Characterization of the organic matter in submicron urban aerosols using a Thermo-Desorption Proton-Transfer-Reaction Time-of-Flight Mass Spectrometer (TD-PTR-TOF-MS). *Atmospheric Environment,* 140**,** 565-575.

Schmitt, S. H. 2017. *Formation of secondary organic aerosol from photo-oxidation of benzene: A chamber stydy.* Doctor of Philosophy, Universität Bayreuth.

Seinfeld, J. & Pandis, S. 2006. ATMOSPHERIC CHEMISTRY AND PHYSICS: From Air Pollution to Climate Change, second edition. *WILEY-INTERSCIENCE PUBLICATION.*

Shiraiwa, M. & Seinfeld, J. H. 2012. Equilibration timescale of atmospheric secondary organic aerosol partitioning. *Geophysical Research Letters,* 39**,** n/a-n/a.

Stark, H., Yatavelli, R. L. N., Thompson, S. L., Kang, H., Krechmer, J. E., Kimmel, J. R., Palm, B. B., Hu, W., Hayes, P. L., Day, D. A., Campuzano-Jost, P., Canagaratna, M. R., Jayne, J. T., Worsnop, D. R. & Jimenez, J. L. 2017. Impact of Thermal Decomposition on Thermal Desorption Instruments: Advantage of Thermogram Analysis for Quantifying Volatility Distributions of Organic Species. *Environ Sci Technol*.

Stein, S. E. & Brown, R. L. 1994. Estimation of normal boiling points from group contributions. *J. Chem. Inf. Comput. Sci.,* 34**,** 581-7.

Steitz, B. 2010. *Experimental determination of the partitioning coefficient of nopinone as a marker substance in organic aerosol*. PhD, Wuppertal University.

Stocker, T. F., Qin, D., Plattner, G. K., Tignor, M., Allen, S. K., Boschung, J., Nauels, A., Xia, Y., Bex, V. & Midgley, P. M. 2013. IPCC, 2013: Summary for Policymakers. In: Climate Change 2013: The Physical Science Basis. Contribution of Working Group I to the Fifth Assessment Report of the Intergovernmental Panel on Climate Change.

Su, T. & Chesnavich, W. J. 1982. Parametrization of the ion–polar molecule collision rate constant by trajectory calculations. *The Journal of Chemical Physics,* 76**,** 5183-5185.

Thompson, S. L., Yatavelli, R. L. N., Stark, H., Kimmel, J. R., Krechmer, J. E., Day, D. A., Hu, W., Isaacman-Vanwertz, G., Yee, L., Goldstein, A. H., Khan, M. a. H., Holzinger, R., Kreisberg, N., Lopez-Hilfiker, F. D., Mohr, C., Thornton, J. A., Jayne, J. T., Canagaratna, M., Worsnop, D. R. & Jimenez, J. L. 2017. Field intercomparison of the gas/particle partitioning of oxygenated organics during the Southern Oxidant and Aerosol Study (SOAS) in 2013. *Aerosol Science and Technology,* 51**,** 30-56.

Tobias, H. J. & Ziemann, P. J. 1999. Compound Identification in Organic Aerosols Using Temperature-Programmed Thermal Desorption Particle Beam Mass Spectrometry. *Analytical Chemistry,* 71**,** 3428-3435.

Tobias, H. J. & Ziemann, P. J. 2001. Kinetics of the Gas-Phase Reactions of Alcohols, Aldehydes, Carboxylic Acids, and Water with the C13 Stabilized Criegee Intermediate Formed from Ozonolysis of 1-Tetradecene. *The Journal of Physical Chemistry A,* 105**,** 6129-6135.

Virtanen, A., Joutsensaari, J., Koop, T., Kannosto, J., Yli-Pirila, P., Leskinen, J., Makela, J. M., Holopainen, J. K., Poschl, U., Kulmala, M., Worsnop, D. R. & Laaksonen, A. 2010. An amorphous solid state of biogenic secondary organic aerosol particles. *Nature,* 467**,** 824-7.

Wiedensohler, A., Birmili, W., Nowak, A., Sonntag, A., Weinhold, K., Merkel, M., Wehner, B., Tuch, T., Pfeifer, S., Fiebig, M., Fjäraa, A. M., Asmi, E., Sellegri, K., Depuy, R., Venzac, H., Villani, P., Laj, P., Aalto, P., Ogren, J. A., Swietlicki, E., Williams, P., Roldin, P., Quincey, P., Hüglin, C., Fierz-Schmidhauser, R., Gysel, M., Weingartner, E., Riccobono, F., Santos, S., Grüning, C., Faloon, K., Beddows, D., Harrison, R., Monahan, C., Jennings, S. G., O'dowd, C. D., Marinoni, A., Horn, H. G., Keck, L., Jiang, J., Scheckman, J., Mcmurry, P. H., Deng, Z., Zhao, C. S., Moerman, M., Henzing, B., De Leeuw, G., Löschau, G. & Bastian, S. 2012. Mobility particle size spectrometers: harmonization of technical standards and data structure to facilitate high quality long-term observations of atmospheric particle number size distributions. *Atmos. Meas. Tech.,* 5**,** 657-685.

Williams, B. J., Goldstein, A. H., Kreisberg, N. M. & Hering, S. V. 2006. An In-Situ Instrument for Speciated Organic Composition of Atmospheric Aerosols:Thermal DesorptionAerosolGC/MS-FID (TAG). *Aerosol Science and Technology,* 40**,** 627-638.

Williams, B. J., Jayne, J. T., Lambe, A. T., Hohaus, T., Kimmel, J. R., Sueper, D., Brooks, W., Williams, L. R., Trimborn, A. M., Martinez, R. E., Hayes, P. L., Jimenez, J. L., Kreisberg, N. M., Hering, S. V., Worton, D. R., Goldstein, A. H. & Worsnop, D. R. 2014. The First Combined Thermal Desorption Aerosol Gas Chromatograph—Aerosol Mass Spectrometer (TAG-AMS). *Aerosol Science and Technology,* 48**,** 358-370.

Yatavelli, R. L. N., Stark, H., Thompson, S. L., Kimmel, J. R., Cubison, M. J., Day, D. A., Campuzano-Jost, P., Palm, B. B., Hodzic, A., Thornton, J. A., Jayne, J. T., Worsnop, D. R. & Jimenez, J. L. 2014. Semicontinuous measurements of gas–particle partitioning of organic acids in a ponderosa pine forest using a MOVI-HRToF-CIMS. *Atmospheric Chemistry and Physics,* 14**,** 1527-1546.

Yu, J., Cocker, D. R., Griffin, R. J., Flagan, R. C. & Seinfeld, J. H. 1999. Gas-Phase Ozone Oxidation of Monoterpenes: Gaseous and Particulate Products. *Journal of Atmospheric Chemistry,* 34**,** 207-258.

Zhang, Y. P., Williams, B. J., Goldstein, A. H., Docherty, K., Ulbrich, I. M. & Jimenez, J. L. 2014. A Technique for Rapid Gas Chromatography Analysis Applied to Ambient Organic Aerosol Measurements from the Thermal Desorption Aerosol Gas Chromatograph (TAG). *Aerosol Science and Technology,* 48**,** 1166-1182.

Zhao, Y., Kreisberg, N. M., Worton, D. R., Isaacman, G., Weber, R. J., Liu, S., Day, D. A., Russell, L. M., Markovic, M. Z., Vandenboer, T. C., Murphy, J. G., Hering, S. V. & Goldstein, A. H. 2013a. Insights into secondary organic aerosol formation mechanisms from measured gas/particle partitioning of specific organic tracer compounds. *Environ Sci Technol,* 47**,** 3781-7.

Zhao, Y., Kreisberg, N. M., Worton, D. R., Teng, A. P., Hering, S. V. & Goldstein, A. H. 2013b. Development of an In SituThermal Desorption Gas Chromatography Instrument for Quantifying Atmospheric Semi-Volatile Organic Compounds. *Aerosol Science and Technology,* 47**,** 258-266.

Zuend, A., Marcolli, C., Booth, A. M., Lienhard, D. M., Soonsin, V., Krieger, U. K., Topping, D. O., Mcfiggans, G., Peter, T. & Seinfeld, J. H. 2011. New and extended parameterization of the thermodynamic model AIOMFAC: calculation of activity coefficients for organic-inorganic mixtures containing carboxyl, hydroxyl, carbonyl, ether, ester, alkenyl, alkyl, and aromatic functional groups. *Atmospheric Chemistry and Physics,* 11**,** 9155-9206.

Appendix A Supplementary Material to Support the Results and Discussion Chapter

In this Appendix additional information to further support the results of this work are provided. Figures and Tables are divided in subsections depending on their related topic.

A.1 Calibrated compounds for the ACM-PTR-ToF-MS

Table A 1: Compounds the ACM-PTR-ToF-MS was calibrated for and the sensitivity of the instrument towards each of the compounds. Sensitivity values were used to derive ppbV from ncps as given from equation 5.

Compound	Protonated compound		Sensitivity (ncps/ppb)
	Formula	molecular weight (g mol^{-1})	
Acetonitrile	$(C_2H_3N)H+$	42.03	23.22
Acetaldehyde	$(C_2H_4O)H+$	45.03	27.86
Butanol	$(C_4H_8)H+$	57.07	5.06
Acetone	$(C_3H_6O)H+$	59.05	24.26
Isoprene	$(C_5H_8)H+$	69.07	5.19
MVK	$(C_4H_6O)H+$	71.05	10.28
Butanone	$(C_4H_8O)H+$	73.06	15.47
Benzene	$(C_6H_6)H+$	79.05	15.31
Monoterpene [(1)]	$(C_6H_8)H+$	81.07	7.42
Pentanone	$(C_5H_{10}O)H+$	87.08	5.93
Toluene	$(C_7H_8)H+$	93.07	13.99
Xylene	$(C_8H_{10})H+$	107.09	15.83
Chlorobenzene	$(C_6H_5Cl)H+$	113.02	9.73
Chlorobenzene	$(C_6H_5{}^{37}Cl)H+$	115.01	3.13
Trimethylbenzene	$(C_9H_{12})H+$	121.10	19.36
Monoterpene	$(C_{10}H_{16})H+$	137.13	3.80
Nopinone	$(C_9H_{14}O)H+$	139.11	7.55

[(1)] Monoterpene fragment

A.2 Compounds seen in this work that overlap with compounds observed in previous publications

Table A 2: Oxidation experiments overview based on the different precursor used (β-pinene, limonene, α-pinene, Δ3-carene) and a list of the oxidation products observed in this work that overlap with compounds detected from previous publications. Information of the chemical formula, molecular weight (MW), chemical structure and SMILES code are provided. Compounds with the same chemical formula but different chemical structures are listed below.

Experiment type and oxidation products	Chemical formula	MW	Structure	SMILES code
β-pinene oxidation (Hohaus et al., 2015, Yu et al., 1999, Chen and Griffin, 2005, Jenkin, 2004)				
Nopinone	$C_9H_{14}O$	138.21		CC1(C2CC1C(=O)CC2)C
2,2-Dimethyl-cyclobutane-1,3-dicarboxaldehyde	$C_8H_{12}O_2$	140.18		O=CC1CC(C=O)C1(C)C
Oxonopinone	$C_9H_{12}O_2$	152.19	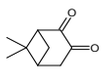	CC1(C2CC1C(=O)C(=O)C2)C
2,2-Dimethyl-3-formyl-cyclobutyl-methanoic acid	$C_8H_{12}O_3$	156.18	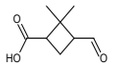	OC(=O)C1CC(C=O)C1(C)C
Norpinonic acid top/ Pinalic-3-acid middle/ Pinalic-4-acid bottom	$C_9H_{14}O_3$	170.21	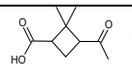 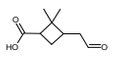 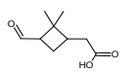	OC(=O)C1CC(CC=O)C1(C)C OC(=O)CC1CC(C=O)C1(C)C OC(=O)C1CC(C(C)=O)C1(C)C
Norpinic acid	$C_8H_{12}O_4$	172.18	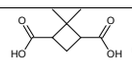	CC1(C(CC1C(=O)O)C(=O)O)C
Hydroxy norpinonic acids	$C_9H_{14}O_4$	186.21	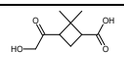	OC(=O)C1CC(C(=O)CO)C1(C)C OC(C=O)C1CC(C(=O)O)C1(C)C

			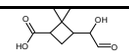	
Pinic acid	$C_9H_{14}O_4$	186.21	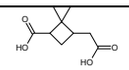	CC1(C(CC1C(=O)O)CC(=O)O)C
Limonene oxidation (Jaoui et al., 2006, Kundu et al., 2012, Leungsakul et al., 2005b, Leungsakul et al., 2005a, Chen and Griffin, 2005)				
3-Oxobutanal	$C_4H_6O_2$	86.09	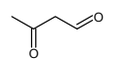	CC(=O)CC=O
Levulinic acid	$C_5H_8O_3$	116.12	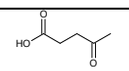	CC(=O)CCC(=O)O
Pentanedioic acid	$C_5H_8O_4$	132.11	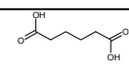	OC(=O)CCCCC(=O)O
3,6-Oxoheptanoic acid	$C_7H_{10}O_4$	158.15	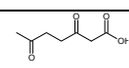	O=C(CCC(C)=O)CC(=O)O
Limonalic acid	$C_9H_{14}O_3$	170.21	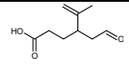	O=CCC(CCC(=O)O)C(=C)C
Norlimononic acid	$C_9H_{14}O_3$	170.21	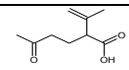	O=C(C)CCC(C(=C)C)C(=O)O
Ketolimononaldehyde	$C_9H_{14}O_3$	170.21	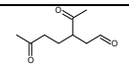	CC(=O)C(CC=O)CCC(=O)C
Norlimonic acid	$C_8H_{12}O_4$	172.18	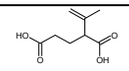	OC(=O)CCC(C(=C)C)C(=O)O
Limononic acid	$C_{10}H_{16}O_3$	184.23	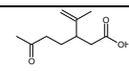	O=C(C)CCC(CC(=O)O)C(=C)C
4-Isopropenyl-1-methyl-1,5-hydroxy-2-oxocyclohexane	$C_{10}H_{16}O_3$	184.23	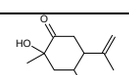	CC(=C)C1CC(=O)C(C)(O)CC1O
7-Hydroxylimononaldehyde	$C_{10}H_{16}O_3$	184.23	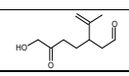	O=C(CCC(CC=O)C(=C)C)CO

Ketolimononic acid	$C_9H_{14}O_4$	186.21	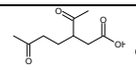	O=C(C)CCC(CC(=O)O)C(C)=O
Limonic acid	$C_9H_{14}O_4$	186.21	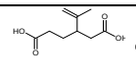	OC(=O)CCC(CC(=O)O)C(=C)C
Ketolimonic acid	$C_8H_{12}O_5$	188.18	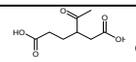	OC(=O)CCC(CC(=O)O)C(C)=O
5-Hydroxylimononic acid	$C_{10}H_{16}O_4$	200.23	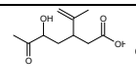	O=C(C)C(O)CC(CC(O)=O)C(=C)C
7-Hydroxylimononic acid	$C_{10}H_{16}O_4$	200.23	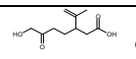	O=C(CCC(CC(=O)O)C(=C)C)CO

α-pinene and Δ^3-carene oxidation (tree emissions) (Praplan et al., 2014, Yu et al., 1999, Chen and Griffin, 2005)				
2,2-Dimethyl-cyclobutyl-1,3-dicarboxaldehyde	$C_8H_{12}O_2$	140.18	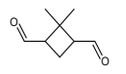	O=CC1CC(C=O)C1(C)C
2,2-Dimethyl-3-formyl-cyclobutyl-methanoic-acid	$C_8H_{12}O_3$	156.18	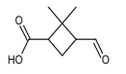	OC(=O)C1CC(C=O)C1(C)C
Norpinonic acid and isomers(upper three) / 3-Norcaronic acid and isomers (bottom three)	$C_9H_{14}O_3$	170.21	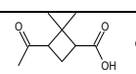	OC(=O)C1CC(C(C)=O)C1(C)C
			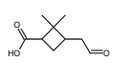	OC(=O)C1CC(CC=O)C1(C)C
			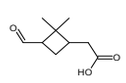	OC(=O)CC1CC(C=O)C1(C)C O=C(C)CC1C(C(=O)O)C1(C)C
			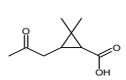	OC(=O)CC1C(CC=O)C1(C)C OC(=O)CC1C(CC=O)C1(C)C

			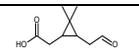 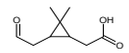	
Norpinic acid / Nor-3-caric acid	$C_8H_{12}O_4$	172.18	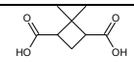	CC1(C(CC1C(=O)O)C(=O)O)C
(2,2-Dimethyl-3-acetyl)-cyclobutyl-formate	$C_{10}H_{16}O_3$	184.23	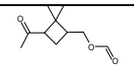	O=C(C)C1CC(COC=O)C1(C)C
Pinonic acid / 3-caronic acid	$C_{10}H_{16}O_3$	184.23	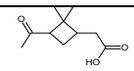	OC(=O)CC1CC(C(C)=O)C1(C)C
Hydroxy pinonaldehydes (upper two) / Hydroxy 3-caronic acid (bottom)	$C_{10}H_{16}O_3$	184.23	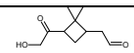 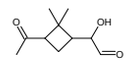	O=C(CO)C1CC(CC=O)C1(C)C OC(C=O)C1CC(C(C)=O)C1(C)C
Pinic acid / 3-Caric acid	$C_9H_{14}O_4$	186.21	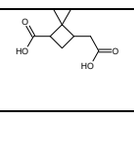	CC1(C(CC1C(=O)O)CC(=O)O)C

A.3 O:C values for the ACM and CHARON for all experiments

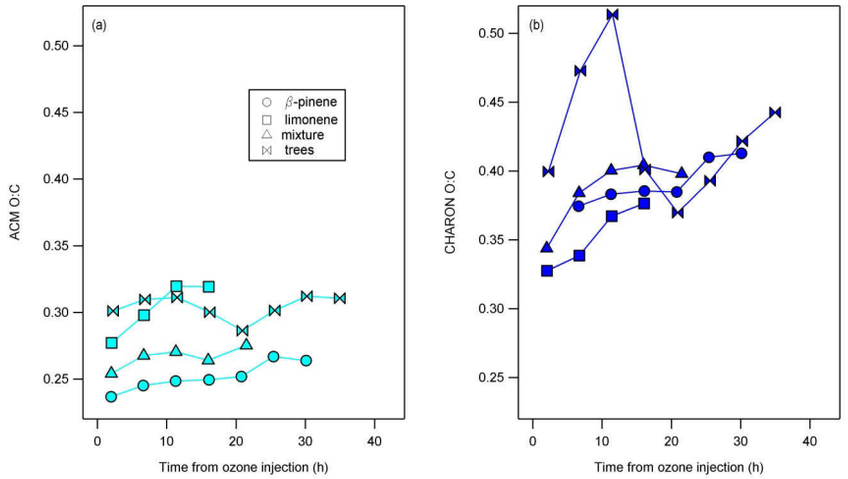

Figure A 3. 1: Average values of the oxygen to carbon (O:C) ratios obtained from each experiment for (a) ACM and (b) CHARON. Each marker is an indicator of the experiment performed with mixture indicating the experiment using β-pinene and limonene as precursors and trees representing the emissions obtained from the trees as discussed in section 3.2. Calculation of the O:C ratios are obtained based on section 4.1.

A.4 Oxygen to carbon ratio comparison based on the different E/N operating conditions of CHARON

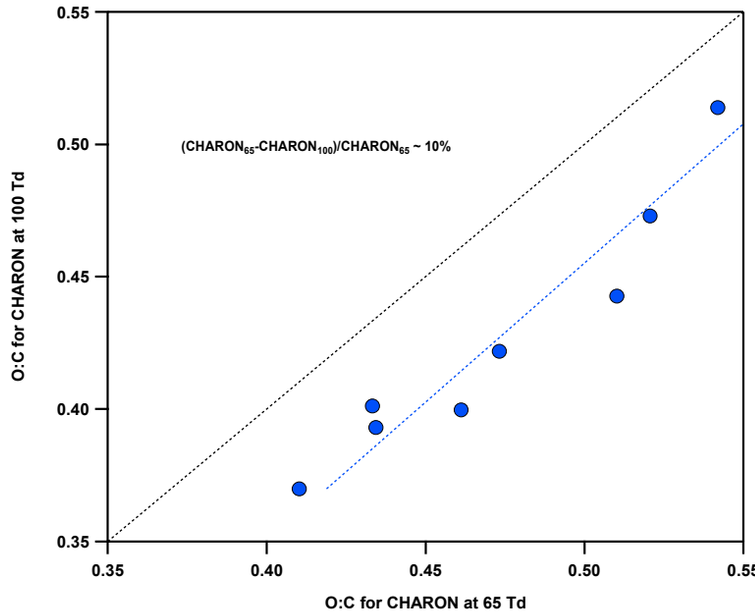

Figure A 4. 1: Comparison of the oxygen to carbon ratio during the tree emissions oxidation experiment for the different E/N conditions the CHARON was operated (x-axis for E/N 65 Td and y-axis for E/N 100 Td). The black dash line indicates the 1:1 line and the blue dash line is the linear fit applied to the data. The upper left equation provides the average % difference between the O:C at 65 Td and 100 Td. This graph is adopted from Gkatzelis et al. (2017).

A.5 Comparison of the PTR-based techniques to the AMS O:C ratio

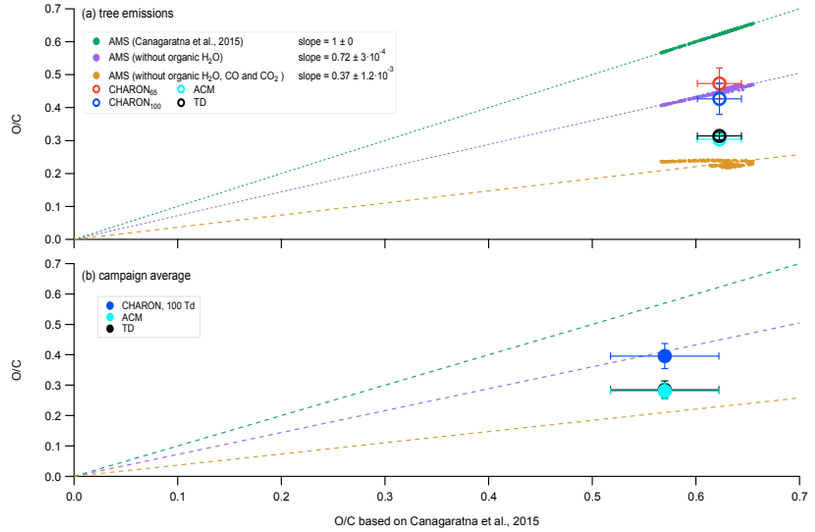

Figure A 5. 1: The average AMS O:C based on Canagaratna et al. (2015)(x-axis) (a) for the tree emissions ozonolysis experiment compared to the AMS O:C, when excluding surface fragmentation peaks (H_2O, CO and CO_2) and compared to the average O:C for the different PTR-based techniques during the tree emissions and (b) for the whole campaign, compared to the different aerosol chemical characterization techniques campaign average O:C. Error bars indicate the ± 1 standard deviation of the average both for the AMS and the different aerosol chemical characterization techniques. Dash lines correspond to the linear fit of the AMS case studies (green: AMS based on Canagaratna et al., 2015, purple: AMS without organic H_2O peak and brown: AMS without organic H_2O, CO and CO_2) derived from the tree emissions experiment. This graph is adopted from Gkatzelis et al. (2017).

A.6 Fractional mass loss of ACM at each temperature step for the β-pinene and limonene experiment

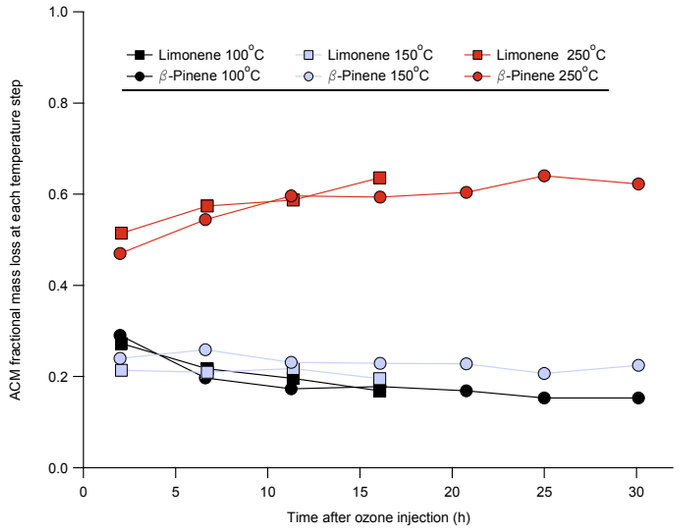

Figure A 6. 1: Fractional mass loss of the ACM at each temperature step during the β-pinene (circle markers) and limonene (square markers) experiment versus the time after ozone injection. Different colors correspond to different temperatures. This graph is adopted from Gkatzelis et al. (2017).

A.7 CHARON differences in the SOA classification due to the different E/N operating conditions during the tree emissions experiment

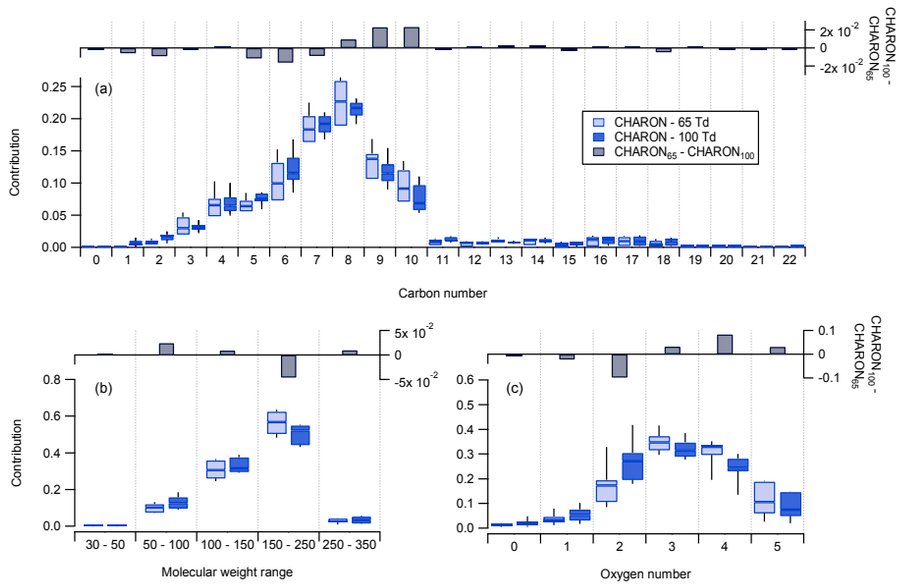

Figure A 7. 1: Box-and-whisker plots showing the relative OA mass concentration distribution dependent on (a) molecular carbon number, (b) molecular weight and (c) molecular oxygen number for the tree emissions experiment and CHARON operated at two different E/N conditions indicated with different colours ($CHARON_{100}$ dark blue, $CHARON_{65}$ ciel). Each box-and-whisker corresponds to the median, 25^{th} and 75^{th} percentile levels of all data for the tree emissions experiment. Upper graphs indicate the difference between the CHARON operated at 65 Td to the 100 Td. This graph is adopted from Gkatzelis et al. (2017).

A.8 Lab experiment using pinonic acid particles and operating the CHARON at different E/N conditions

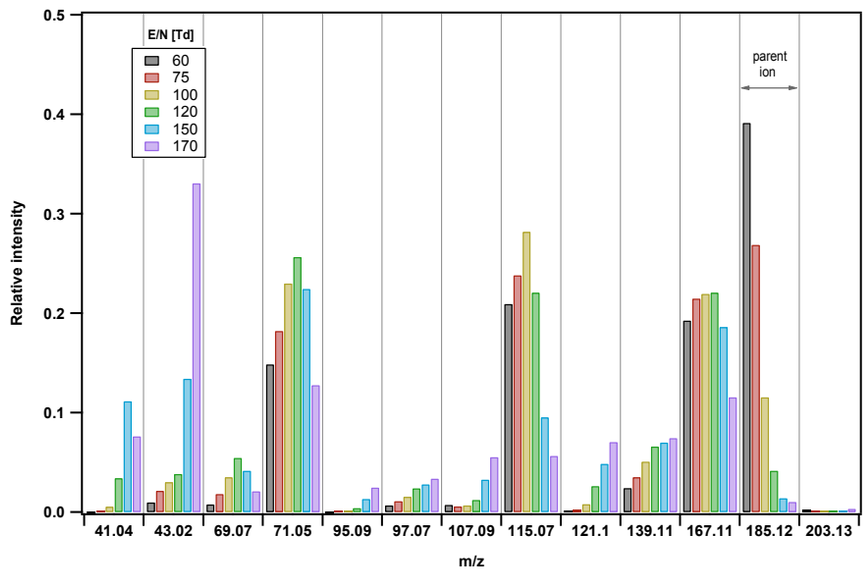

Figure A 8. 1: Lab experiments to measure pinonic acid at different E/N conditions. The relative intensity of each *m/z* (transmission corrected normalized counts per second fraction) for the different E/N conditions is indicated by the bar colour. The protonated parent pinonic acid is shown in *m/z* 185.12. This graph is adopted from Gkatzelis et al. (2017).

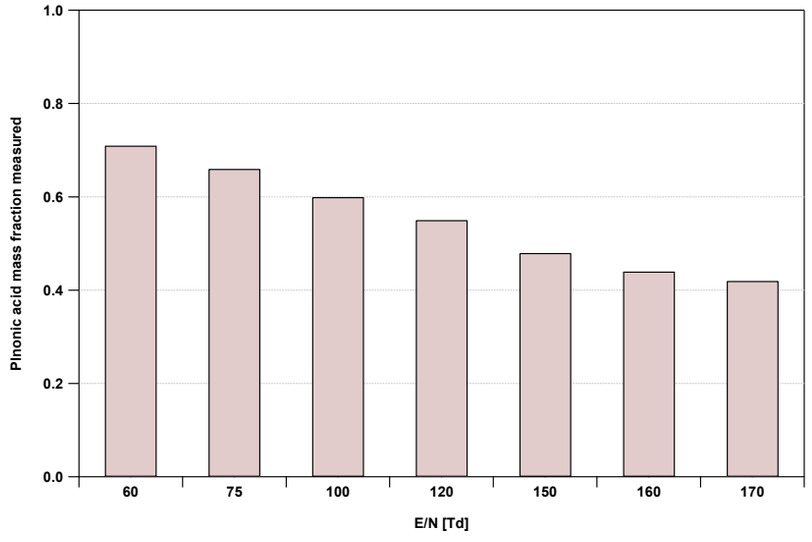

Figure A 8. 2: Mass fraction of the pinonic acid particles compared to an SMPS, for the different E/N conditions of the CHARON-PTR-ToF-MS, ranging from 60 up to 173 Td. Assumption of uniform sensitivity is made and mass concentration is generated by taking the sum of all fragments and assuming all *m/z*'s represent parent molecules. This graph is adopted from Gkatzelis et al. (2017).

A.9 Fragmentation pathways and ion overlaps

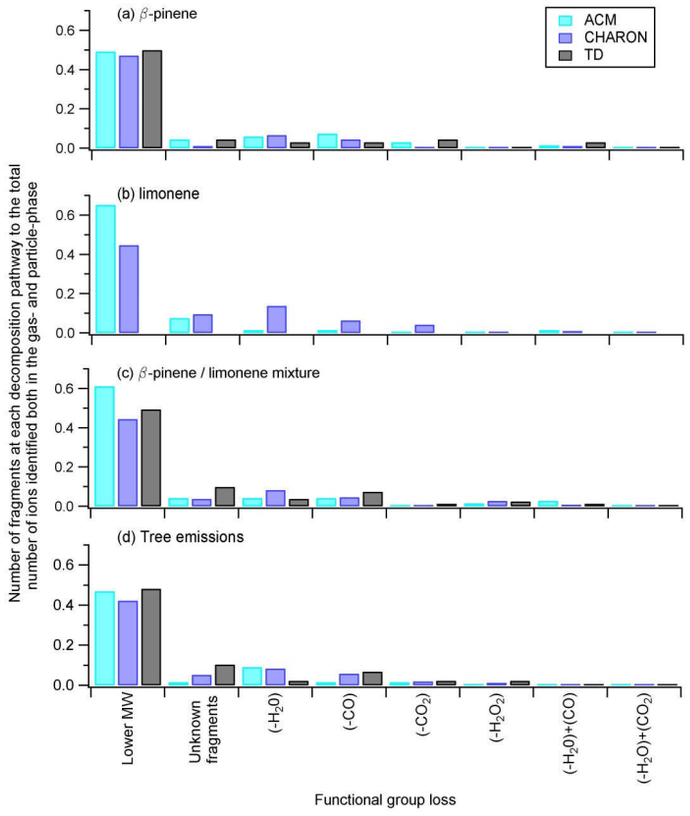

Figure A 9. 1: The ratio of the number of lower molecular weight and unknown fragments as well as fragments subject to functional group loss ((-H_2O), (-CO) (-CO_2), (-H_2O_2), (-H_2O) and (-CO), (-H_2O) and (-CO_2)) to the number of identified ions both in the gas- and particle-phase. Different colours indicate the different instruments for the different experiments.

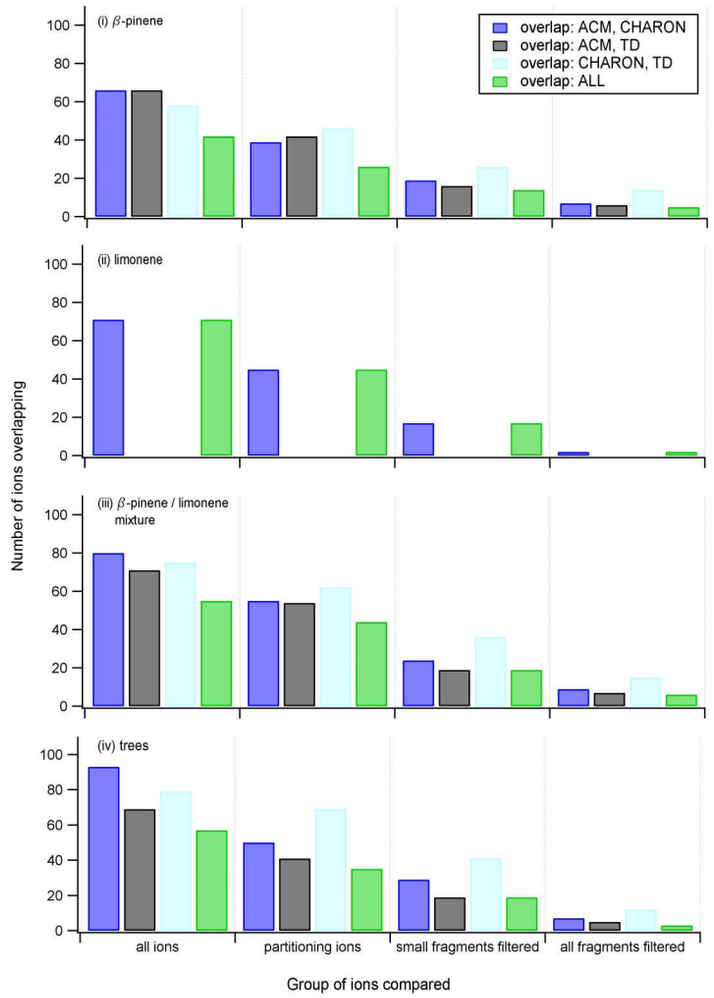

Figure A 9. 2: The number of ions measured from more than one technique with a focus on the ions measured both from ACM and CHARON (blue), ACM and TD (black), CHARON and TD (ciel) and ions measured from all techniques, accounting for ACM, TD and CHARON (green). Overlaps are checked for different groups of ions starting from the overlaps of all ions detected, to overlaps seen for only the ions that partition between the gas- and particle-phase, to the overlaps of the remaining partitioning ions after filtering out the small fragments and the remaining partitioning ions after filtering out all fragments for the different experiments performed.

A.10 Mapping ACM and CHARON to the 2D-VBS

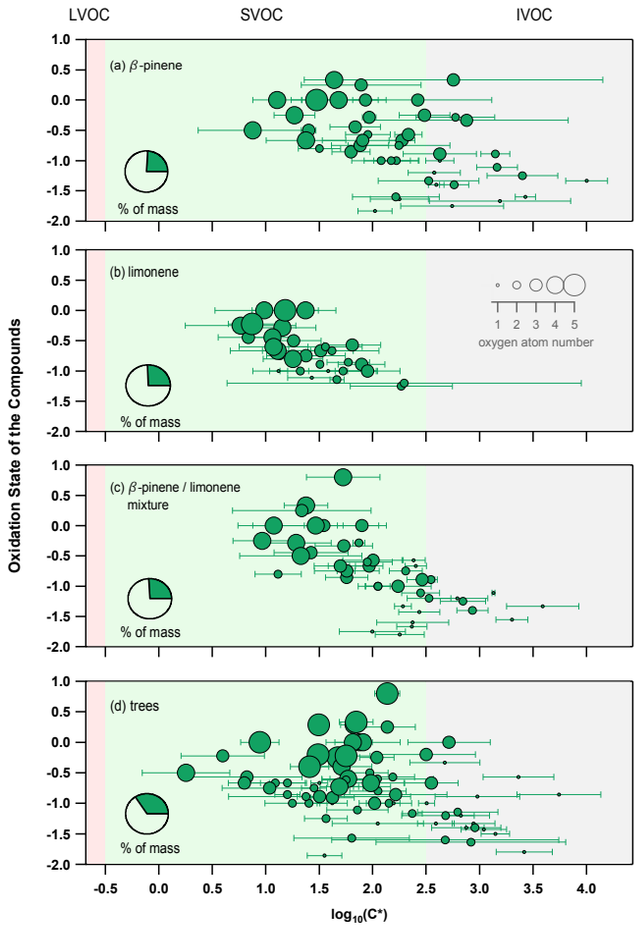

Figure A 10. 1: The average experimental saturation concentration for detected ions (from ACM and CHARON) that act as parent ions identified using the described selection criteria during the different experiments. Error bars indicate the ± 1σ of the average. Size of the markers is an indicator of the oxygen atom number for each species. Pie charts show the percent of mass (green) measured when adding all presented ions compared to the total organic mass obtained from the AMS.

A.11 Vapour pressure estimation using different theoretical approaches

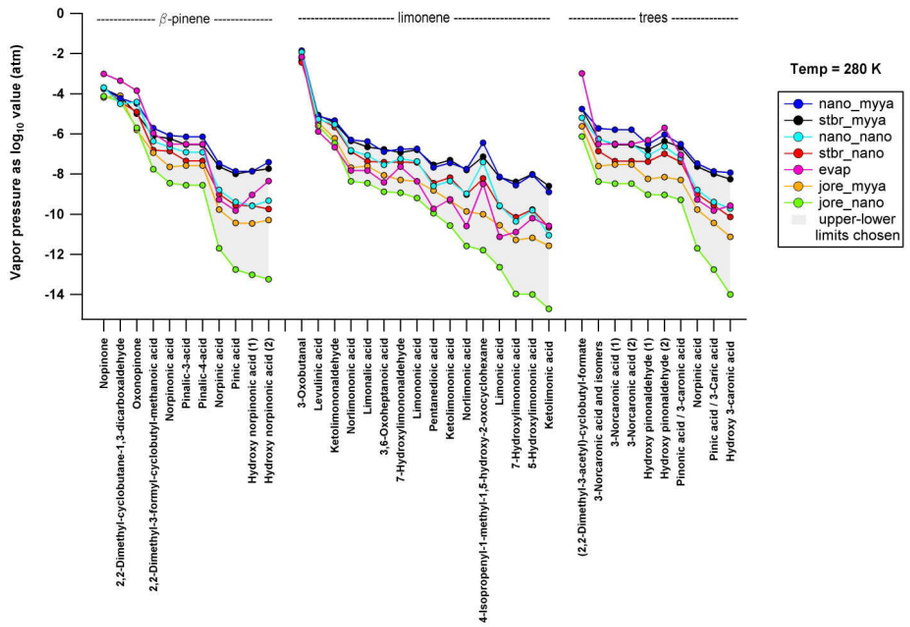

Figure A 11. 1: Theoretical calculation of the vapor pressure (y-axis) using the combination of 7 different approaches. The grey background color indicates the minimum and maximum range chosen for this study. The label indicates the different approaches used for the calculation of the boiling point (left of the underscore) and the saturation vapor pressure (right of the underscore). For the boiling point “nano” stands for Nannoolal et al. (2004), “strb” for Stein and Brown (1994), “evap” for the EVAPORATION method and “jore” for Joback and Reid (1987). For the saturation vapor pressure “myya” stands for Myrdal and Yalkowsky (1997) and “nano” for Nannoolal et al. (2008). Details on the different approaches are provided in section 3.4.

Appendix B Software and Hardware Updates

B.1 Hardware Updates

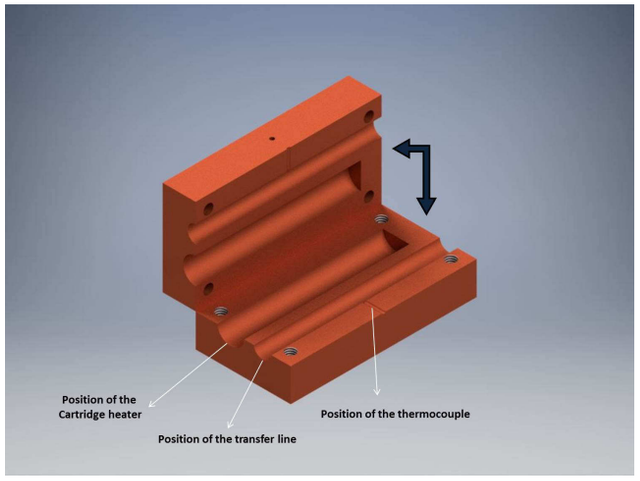

Figure B 1: Schematic representation of the copper plates designed using the software INVENTOR to assure uniform temperatures for the ACM transfer line from the collector to the valve-box. Minimum distance of the cartridge heater and the thermocouple from the transfer line was achieved.

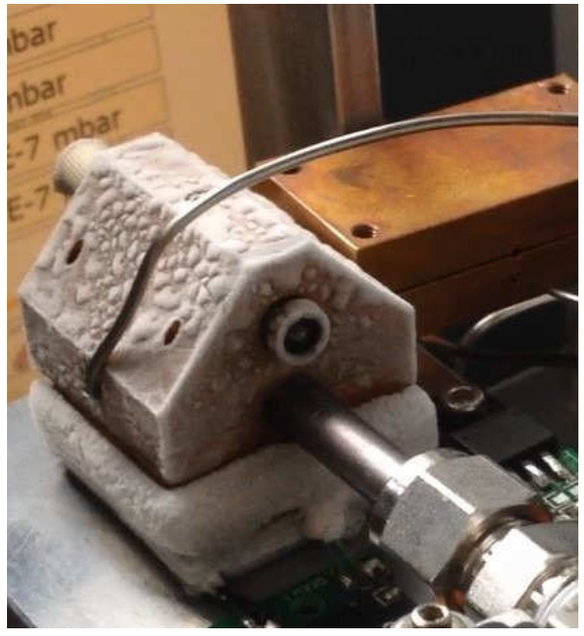

Figure B 2: Frost generated on the collector of the ACM during collection. Before changing to the desorption mode the collector was first heated up to 20 °C in order to disconnect the peltier element using the lifter.

Ich versichere, dass ich die von mir vorgelegte Dissertation selbständig angefertigt, die benutzten Quellen und Hilfsmittel vollständig angegeben und die Stellen der Arbeit − einschließlich Tabellen, Karten und Abbildungen −, die anderen Werken im Wortlaut oder dem Sinn nach entnommen sind, in jedem Einzelfall als Entlehnung kenntlich gemacht habe; dass diese Dissertation noch keiner anderen Fakultät oder Universität zur Prüfung vorgelegen hat; dass sie − abgesehen von unten angegebenen Teilpublikationen − noch nicht veröffentlicht worden ist, sowie, dass ich eine solche Veröffentlichung vor Abschluss des Promotionsverfahrens nicht vornehmen werde. Die Bestimmungen der Promotionsordnung sind mir bekannt. Die von mir vorgelegte Dissertation ist von (Prof. Andreas Hofzumahaus und Prof. Astrid Kiendler-Scharr) betreut worden.

Curriculum Vitae

Georgios Gkatzelis
Bendstrasse 54,
Aachen, 52066, Germany
ResearcherID: http://www.researcherid.com/rid/R-1057-2016

(+49) 15777336152
g.gkatzelis@fz-juelich.de

Education

- Institute of Energy and Climate Research, IEK-8: Troposphere, Forschungszentrum JülichGmbH, Jülich, Germany and the Chemistry Department, University of Cologne, Germany
  Ph.D. with a focus in Atmospheric Chemistry (October 2014- expected submission in October 2017)
  Supervisor: A. Kiendler-Scharr

- Chemical Engineering Department, University of Patras, Greece
  M.Sc. with a focus on Air Environmental Pollution (February 2012-July 2014)
  Supervisor: S.N. Pandis, Group: LAQS (http://laqs.iceht.forth.gr/)

- Chemical Engineering Department, University of Patras, Greece
  Diploma with grade 8.01/10 (September 2005-April 2011)
  Field: Science and Technology of Materials
- Kato Kastritsi High School, Patras, Greece
  Graduation with grade 19.3/20 (June 2005)

Research Experience

- **Simulation chamber studies to investigate SOA production** (June 2015-July 2015); Responsibilities: Installation & operation of PTR-ToF-MS, data evaluation; Host: G. McFiggans, Manchester University, UK

- **ME2 Workshop 2016, Zürich** (November 2016)

- **Winter field campaign in Beijing, China: A study on haze episodes** (January 2016-March 2016); Responsibilities: Installation & operation of ACM-PTR-ToF-MS, data evaluation; Host: Yuanhang Zhang, College of Environmental Sciences and Engineering, Peking University, China

- **Research visit at the Aix-Marseille University**, France (December 2015); Research focus: Training on the Thermal desorption Aerosol Gas Chromatography Aerosol Mass Spectrometry (TAG-AMS); Host: N. Marchand, University of Marseille, France

- **Simuation chamber campaign using SAPHIR and SAPHIR-PLUS to compare state of the art aerosol characterization instrumentation: Studies on biogenic SOA formation and aging** (June 2015-July 2015); Responsibilities: Installation & operation of ACM-PTR-ToF-MS, data evaluation for all instruments; Host: A. Kiendler-Scharr, Forschungszentrum JülichGmbH

- **Instrument development, automation and optimization** in Jülich, Germany (November 2014-June 2015); Host: A. Kiendler-Scharr, Forschungszentrum Jülich GmbH

- **Research visit at TU Delft, Netherlands** (February 2013-June 2013); Research focus : Aerosol instrumentation and aerosol based nanotechnology; Host: A. Schmidt-Ott and G. Biskos, TU Delft, Netherlands

- **Wintertime field campaign in Athens, Greece** (January 2013-February 2013); Responsibilities: Installation & operation of a thermodenuder coupled to a SMPS and an AMS, data evaluation; Host : S.N. Pandis, Patras, Greece

- **Simulation chamber studies to characterize a thermodenuder** at high operating temperatures (2012); Host : S.N. Pandis, Patras, Greece

Teaching and Work Experience

- September 2012-January 2013
  Teaching Assistant, University of Patras, Greece
  Field: Mathematics, Ordinary Differential Equations

- September 2011-December 2011
  Research Assistant, FORTH ICE-HT, Patras, Greece (http://www.iceht.forth.gr)
  Field: Environmental Pollution

- December 2010-August 2011
  Hellenic Army, caterers
  Role: Responsible for the logistics (food supply & payment of soldiers)

Journal publications in preparation

1. **Gkatzelis, G. I.**, T. Hohaus, R. Tillmann, I. Gensch, M. Müller, P. Eichler, Kang-Ming Xu, Z. Yu, P. Schlag, S. H. Schmitt, R. Wegener, M. Kaminski, R. Holzinger, A. Wisthaler, A. Kiendler-Scharr: Gas-to-particle partitioning of major biogenic oxidation products: A study on freshly formed and aged biogenic SOA

Journal publications

1. **Gkatzelis, G. I.**, R. Tillmann, T. Hohaus, M. Müller, P. Eichler, Kang-Ming Xu, P. Schlag, S. H. Schmitt, R. Wegener, M. Kaminski, R. Holzinger, A. Wisthaler, A. Kiendler-Scharr: Comparison of three aerosol chemical characterization techniques utilizing PTR-ToF-MS: A study on freshly formed and aged biogenic SOA, Atmospheric Measurement Techniques Discussions

2. Florou, K., D. K. Papanastasiou, M. Pikridas, C. Kaltsonoudis, E. Louvaris, **Gkatzelis, G. I.**, D. Patoulias,N. Mihalopoulos, and S. N. Pandis: The contribution of wood burning and other pollution sources to wintertime organic aerosol levels in two Greek cities, Atmospheric Chemistry and Physics, 17(4), 3145-3163, doi:10.5194/acp-17-3145-2017, 2017.3.

3. Louvaris, E. E., K. Florou, E. Karnezi, D. K. Papanastasiou, **Gkatzelis, G. I.**, and S. N. Pandis: Volatility of source apportioned wintertime organic aerosol in the city of Athens, Atmospheric Environment, 158,138-147, doi:10.1016/j.atmosenv.2017.03.042, 2017.

4. **Gkatzelis, G. I.**, D. K. Papanastasiou, K. Florou, C. Kaltsonoudis, E. Louvaris, and S. N. Pandis: Measurement of nonvolatile particle number size distribution, Atmospheric Measurement Techniques, 9(1),103-114, doi:10.5194/amt-9-103-2016, 2016.

Thesis

1. **Msc Thesis**, 2014: Measurement of nonvolatile particle number size distribution

Conferences

1. Lu K., Tan Z., Wang H., Li X., Wu Z., Chen Q., Wu Y., Ma X., Liu Y., Liu Y., Chen X., Qiu P., Shang D., Dong H., Zeng L., Shao M., Hu M., Fuchs H., Novelli A., Broch S., Hofzumahaus A., Holland F., Rohrer F., Birger B., **Gkatzelis G. I.**, Schmitt S. H., Kiendler-Scharr A., Wahner A., Zhang Y.: “Heavy haze in winter Beijing driven by fast gas phase oxidation,”
   Oral Presentation in the AGU, December 2017, New Orleans, USA
2. **Gkatzelis, G. I.**, R. Tillmann, T. Hohaus, M. Müller, P. Eichler, Kang-Ming Xu, P. Schlag, S. H. Schmitt, R. Wegener, M. Kaminski, R. Holzinger, A. Wisthaler, A. Kiendler-Scharr, “Comparison of aerosol chemical characterization techniques utilizing a PTR-ToF-MS:A study on biogenic SOA formation and gas-to-particle partitioning,”
   Poster Presentation in the AAAR, October 2017, Raleigh, North Carolina, USA
3. **Gkatzelis, G. I.**, P. Eichler, T. Hohaus, M. Müller, P. Schlag, S.H. Schmitt, R. Tillmann, Kang-Ming Xu, R. Holzinger, A. Wisthaler, A. Kiendler-Scharr, “Comparison of aerosol chemical characterization techniques utilizing a PTR-ToF-MS: A study of biogenic SOA formation and aging,”
   Oral Presentation in the EAC, August-September 2017, Z¨urich, Switzerland
4. S.H. Schmitt, P. Schlag, **Gkatzelis, G. I.**, T. Hohaus, Y. Wang, D. Shang, M. Hu, K. Lu, A. Wahner, A. Kiendler-Scharr, “Insights into PM1 during haze episodes in Beijing, China, using aerosol mass spectrometer in a two month winter field campaign 2016,”
   Oral Presentation in the EAC, August-September 2017, Z¨urich, Switzerland
5. Hendrik Fuchs , Zhaofeng Tan, Keding Lu, S. Broch, Steven S. Brown, Huabin Dong, **Gkatzelis, G. I.**, Sebastian Gomm, Rolf Hseler, Lingyuan He, Andreas Hofzumahaus, Frank Holland, Astrid Kiendler-Scharr, Xin Li, Ying Liu, Sihua Lu, Kyung-Eun Min, Anna Novelli, Franz Rohrer, Min Shao, Baolin Wang, Ming Wang, Yusheng Wu, Limin Zeng, Yingson Zhang, Andreas Wahner, Yuanhang Zhang, “Budget of the OH reactivity in the North China Plain in summer- and wintertime: Results from recent field campaigns,”
   Oral Presentation in the AGU Fall Meeting, December 2016, San Francisco, USA

6. **Gkatzelis, G. I.**, P. Eichler, T. Hohaus, M. Kaminski, M. Müller, P. Schlag, S.H. Schmitt, R. Tillmann, R. Wegener, Kang-Ming Xu, Z. Yu, R. Holzinger, A. Wisthaler, A. Kiendler-Scharr, "Experimental determination of the partitioning coefficient of important BVOC oxidation products at the atmospheric simulation chamber SAPHIR,"
   Poster Presentation in the EAC, September 2016, Tours, France
7. **Gkatzelis, G. I.**, T. Hohaus, R. Tillman, S. H. Schmitt, Z. Yu, R. Wegener, M. Kaminski, A. Kiendler-Scharr, "Experimental determination of the partitioning coefficient and volatility of important BVOC oxidation products using the Aerosol Collection Module (ACM) coupled to a PTR-ToF-MS,"
   Poster Presentation in the AGU Fall Meeting, December 2015, San Francisco, USA.
8. D.K. Papanastasiou, **Gkatzelis, G. I.**, K. Florou, C.Kaltsonoudis, S. N. Pandis, "Nighttime chemistry of biomass burning plumes,"
   Oral Presentation in the EAC, September 2015, Milan, Italy
9. E. E. Louvaris, K.K. Florou, **Gkatzelis, G. I.**, S. N. Pandis, "Volatility of source apportioned wintertime organic aerosol in the city of Athens,"
   Poster Presentation in the EAC, September 2015, Milan, Italy
10. E. Kostenidou, K. Florou, **Gkatzelis, G. I.**, C.Kaltsonoudis, E. Louvaris, D.K. Papanastasiou, M. Pikridas, M. Psichoudaki, A. Siampani, S.N. Pandis, "Temporal and spatial variability of fine PM in the Eastern Mediterranean,"
    Oral Presentation in the IAC, September 2014, Busan, Korea
11. **Gkatzelis, G. I.**, D.K. Papanastasiou, C.Kaltsonoudis,E. Louvaris, K. Florou, S.Bezentakos, G. Biskos, S.N. Pandis, "Measurement of Non-Volatile Particle Number Size Distribution,"
    Poster Presentation in the EGU General Assembly, April-May 2014, Vienna, Austria
12. Dimitrios K. Papanastasiou, Evangelia Kostenidou, **Gkatzelis, G. I.**, Magdalini Psichoudaki, Evangelos Louvaris, and Spyros Pandis, "Photochemical Formation and Aging of Ambient Organic Aerosol: A Laboratory Study,"
    Poster Presentation in the EGU General Assembly, April-May 2014, Vienna, Austria
13. Kalliopi Florou, Christos Kaltsonoudis, Dimitrios Papanastasiou, **Gkatzelis, G. I.**, Evangelos Louvaris, Michael Pikridas and Spyros Pandis, "Wintertime Air Pollution and the Greek Financial Crisis,"
    Oral Presentation in the 32nd Annual AAAR Conference, September-October 2013, Oregon, Portland
14. Evangelia Kostenidou, Kalliopi Florou, Christos Kaltsonoudis, Magda Psichoudaki, Evangelos Louvaris, Dimitrios Papanastasiou, **Gkatzelis, G. I.**, Anna Siampani, Maria Tsiflikiotou, Epameinondas Tsiligiannis and Spyros N. Pandis, "Wintertime Air Pollution and the Greek Financial Crisis,"
    Oral Presentation in the 10th Colloquium FORTH, July 2013, Heraklion, Crete, Greece

Memberships, Funding and Community service

• Reviewer for ACP, July 2017
• Member of Gesellschaft für Aeorosolforschung (GAeF)
• Member of Hellenic Association for Aerosol Research (HAAR)
• GAeF EAC2017 student travel support
• GAeF EAC2016 student travel support

Band / Volume 404
Thermomechanical Characterization of Advanced Ceramic Membrane Materials
Y. Zou (2018), xvi, 168 pp
ISBN: 978-3-95806-288-7

Band / Volume 405
Betrachtung der Kristallinitätsentwicklung in mikrokristallinem Dünnschicht-Silizium mit in-situ Raman-Spektroskopie
T. Fink (2018), XI, 166 pp
ISBN: 978-3-95806-289-4

Band / Volume 406
Institute of Energy and Climate Research
IEK-6: Nuclear Waste Management
Report 2015 / 2016
Material Science for Nuclear Waste Management
S. Neumeier, H. Tietze-Jaensch, D. Bosbach (Eds.)
(2018), 221 pp
ISBN: 978-3-95806-293-1

Band / Volume 407
Reduction properties of a model ceria catalyst at the microscopic scale
J. Hackl (2018), VIII, 98 pp
ISBN: 978-3-95806-294-8

Band / Volume 408
Comparative Analysis of Infrastructures: Hydrogen Fueling and Electric Charging of Vehicles
M. Robinius, J. Linßen, T. Grube, M. Reuß, P. Stenzel, K. Syranidis, P. Kuckertz and D. Stolten (2018), VII, 108 pp
ISBN: 978-3-95806-295-5

Band / Volume 409
Reactions between nitrite and soil organic matter and their role in nitrogen trace gas emissions and nitrogen retention in soil
J. Wei (2018), XXII, 160 pp
ISBN: 978-3-95806-299-3

Band / Volume 410
The impact of soil water distribution on root development and root water uptake of winter wheat
G. Cai (2018), xviii, 143 pp
ISBN: 978-3-95806-303-7

Schriften des Forschungszentrums Jülich
Reihe Energie & Umwelt / Energy & Environment

Band / Volume 411
Charakterisierung und Optimierung der Grenzfläche Elektrolyt/Kathode in metallgestützten Festelektrolyt-Brennstoffzellen
D. Udomsilp (2018), XI, 176 pp
ISBN: 978-3-95806-304-4

Band / Volume 412
Formation of Secondary Organic Aerosol from Photo-Oxidation of Benzene: a Chamber Study
S. H. Schmitt (2018), III, 250 pp
ISBN: 978-3-95806-305-1

Band / Volume 413
Mechanismen der chrombasierten Degradation von metallgestützten Festoxid-Brennstoffzellen
A. Beez (2018), VIII, 144 pp
ISBN: 978-3-95806-306-8

Band / Volume 414
Entwicklung eines Werkzeugs zur Modellierung der Nettoerosion im Hauptraum der Brennkammer eines Tokamaks und Studium der Plasma-Wand-Wechselwirkung an DEMO1
M. Beckers (2018), XIX, 150 pp
ISBN: 978-3-95806-307-5

Band / Volume 415
Fehlstellendotierung von Eisenoxid- und Bismutsulfid-Nanopartikeln
J. P. Mock (2018), v, 187 pp
ISBN: 978-3-95806-309-9

Band / Volume 416
Nanocrystalline Silicon Oxide in Silicon Heterojunction Solar Cells
A. Richter (2018), 166 pp
ISBN: 978-3-95806-310-5

Band / Volume 417
Gas-to-Particle Partitioning of Major Oxidation Products from Monoterpenes and Real Plant Emissions
G. Gkatzelis (2018), xii, 128 pp
ISBN: 978-3-95806-314-3

Weitere ***Schriften des Verlags im Forschungszentrum Jülich*** unter
http://wwwzb1.fz-juelich.de/verlagextern1/index.asp

Energie & Umwelt
Energy & Environment

Gas-to-Particle Partitioning

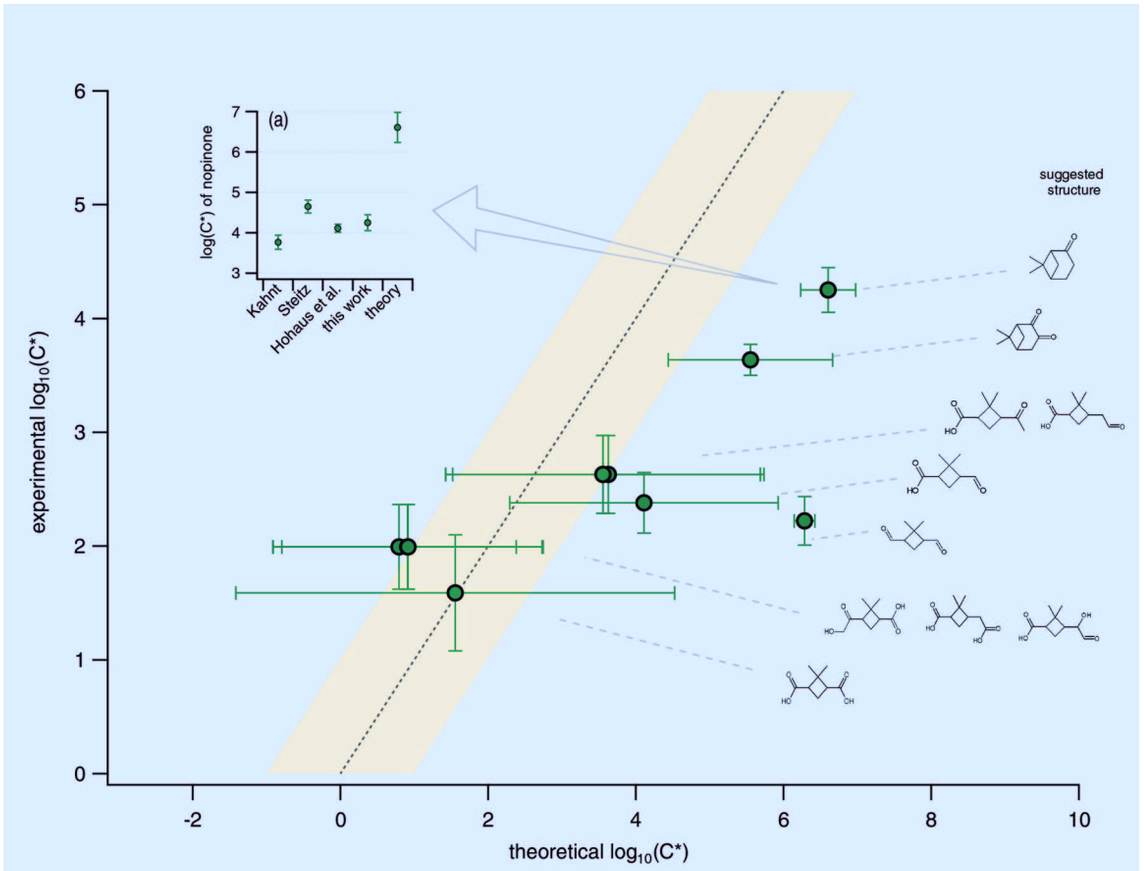

417

Georgios Gkatzelis

Gas-to-Particle Partitioning of Major Oxidation Products from Monoterpenes and Real Plant Emissions

Georgios Gkatzelis

Energie & Umwelt / Energy & Environment
Band / Volume 417
ISBN 978-3-95806-314-3

Energie & Umwelt / Energy & Environment
Band / Volume 417
ISBN 978-3-95806-314-3

Mitglied der Helmholtz-Gemeinschaft

JÜLICH Forschungszentrum

JÜLICH Forschungszentrum

Mitglied der Helmholtz-Gemeinschaft

JÜLICH Forschungszentrum